Durham E-Theses

High Count Rate X-ray Detection for Liquid Threat Identification Applications

SCOTT, PAUL,DAVID

How to cite:

Use policy

High Count Rate X-ray Detection for Liquid Threat Identification Applications

Paul David Scott

Ph.D. Thesis 2011

Abstract

This work presents the development of an x-ray detector system for the multispectral detection of x-rays used in a Bottle Scanner. This system is designed to identify liquid explosives concealed within bottles taken onto aircraft. The Bottle Scanner works by calculating the transmission spectrum for a given bottle and its contents. This is then used as a fingerprinting technique in order to identify the presence of liquid explosives.

The main focus of this work is the design of the detector signal chain and particularly the pulse height detection algorithms for the acquisition of 32 bin x-ray spectra. The pulse height detection algorithms are implemented on a field programmable gate array (FPGA). The performance of such algorithms at high count rate is a key requirement for this application. Four such algorithms are discussed in this work, each with varying complexity and different approaches to pile up handling.

The algorithms are simulated using a Monte Carlo approach where the random arrival rate of photons at the detector is modelled. Algorithms are then emulated using an Agilent DSO90254A oscilloscope before finally being programmed onto an FPGA and tested on a real system. The transmission curves produced in real Bottle Scanner systems show a deviation from those predicted by the underlying physics and exhibit a rollover at high energies. This is shown to be due to pulse pile up effects which are explored in detail.

Depth of interaction effects are also investigated experimentally and by simulation using the Geant4 software package. The results of this are used to design a biparametric type algorithm which is capable of simultaneous pile up rejection and depth of interaction correction.

High Count Rate X-ray Detection for Liquid Threat Identification Applications

by

Paul David Scott BSc (Hons)

A thesis presented in candidature for the degree of Doctor of Philosophy in the University of Durham

Department of Physics

May 2011

Contents

List of Figures

vi

viii

Acknowledgements

I would like to take this opportunity to thank the people who have helped me during my study. In particular I would like to thank my supervisors Professor Andy Brinkman and Professor Brian Tanner for their support throughout my Ph.D study and their encouragement during the write up period.

I would like to thank Arnab Basu, Ben Cantwell and John Mullins for giving me the opportunity of the Ph.D CASE studentship. It seems like a long time ago when I was first interviewed for a technicians post at Durham Scientific Crystals. I would also like to thank Kromek generally for their financial support and the resources they have provided me with throughout my thesis. I continue to find Kromek to be a challenging and fulfilling place to work.

I would like to thank Ian Radley and Mohamed Ayoub who I work closely with every day at Kromek and are a source of valuable discussion and ideas; Barry Sanderson for helping with the set up of experiments; Bijoy TV for his advice and help with programming and John Allison and Mike Taylor for their work on Geant4.

Most of all I wish to thank my wife Laurie for her ongoing support, encouragement and understanding. I am particularly grateful for her help during the final stages of correction and printing which were more troublesome than anticipated.

In loving memory of my son

Billy Scott

Chapter 1   Introduction

1.1   Introduction

The threat from liquid, aerosol and gel based explosives (LAGs) has been present since August 2006 when an attempt was made to smuggle the individual components of a liquid explosive onto an aircraft departing from Heathrow to be constructed into an explosive device while the aircraft was in flight [1].

This incident prompted the need for a step change in the capability of airport screening systems and has consequently opened up a gap in the security market for a new type of scanner. The Bottle Scanner manufactured by Kromek uses a multispectral 'colour x-ray' technique to identify the x-ray transmission signature of LAGs [2]. The x-ray transmission signature is analysed by Kromek's proprietary ADMIT[TM] algorithm which allows the identification of threat liquids and precursors by comparison to a user configurable database.

The Bottle Scanner received European Union (E.U.) Type B Category 2 ECAC certification in October 2010 [3] where Type B defines a system capable of scanning a single sealed bottle and Category 2 relates to the ability of the system to detect the full range of threat liquids during testing.

Other competing technologies include large scale computerised tomography (CT) scanners. These provide good materials identification by virtue of the fact that they are able to examine an object with a 360° view however they are large heavy machines, comparatively slow and have enormous overheads in terms of purchase and maintenance. Consequently such systems have not been issued to airports for hand carried luggage screening. Nuctech offers a standalone LS1516A Inspection System [4] based on dual energy CT technology capable of imaging any type of container, both clear and opaque. Like the Kromek Bottle Scanner this system has also received European Union ECAC certification.

CEIA[5] have produced a bottle and liquid scanner which uses a two stage test to identify potential liquid threats. The first stage uses a wide band radio frequency complex impedance measurement to classify liquids into a 'family' of liquids rather than identifying a specific liquid. The second stage uses shortwave infrared radiation to identify the specific threat and involves decanting a small amount of the suspected threat liquid into a disposable container of known volume and wall thickness to identify the specific threat. The obvious health and safety concerns associated with decanting a suspected threat liquid within a public area of an airport no doubt make this a major drawback of this particular product.

This is clearly a competitive new market and with over 40 major airports in the U.K. alone each requiring multiple scanners this presents an enormous potential revenue stream. At the time of writing Kromek was one of only two companies

to successfully pass ECAC testing making it well placed to capitalise on this emerging new market.

1.2   Historical Background

In 2003 Durham Scientific Crystals (now known as Kromek) was formed to commercialise a ground breaking crystal growth technology developed in the Physics Department of Durham University. The technology was targeted at the growth of large volumes of single crystal cadmium telluride (CdTe) and cadmium zinc telluride (CdZnTe) via a patented vapour phase method known as the Multi Tube Physical Vapour Transport (MTPVT) technique [6,7,8]. Other manufacturers produce crystals from the liquid phase which has resulted in materials of limited size and unpredictable quality[9].

The favourable properties of CdTe such as its wide band gap and high photon stopping power have long made it a material of choice for high energy x-ray detection. The limitations of availability and price have however resulted in the commercial viability of CdTe based technologies being marginal. The use of the MTPVT process is hoped to make possible the mainstream commercial use of CdTe for the first time.

The first commercial use for CdTe came as a gap in the security market became apparent following the aforementioned attempt to smuggle liquid explosives on board transatlantic flights. Until this time the assumed threat had been

predominantly from plastic based explosives. The last innovation in detector technology used in the security industry was the 'dual-energy' detector which was widely introduced following the Lockerbie disaster in 1988 [10].

The dual-energy detector is a sandwich structure of two pieces of scintillator material and a photo diode detector [11],[12]. As suggested by the name these detectors can only detect in two energy bands. The scintillators have different thickness and this allows the detector to separate low energy x-rays from high energy x-rays. The detector can then be used to classify the x-ray beam attenuation to be due to scattering or absorption. This in turn can be used to categorise the material as organic or inorganic. Threat items are expected to be organic although clearly there are many other organic materials which do not pose a threat, meaning that the technology is very limited.

Once the threat from liquid explosive became apparent the existing technology was clearly found wanting. With detection in just two energy bands there is simply no way of accurately identifying all threat items as many share the same x-ray characteristics in these energy regions [2]. The current insistence by airports that passengers remove liquids from hand luggage is indicative of the inability of the existing technology to accurately identify threat materials.

6"

1.3   Motivation for Present Work

Once the liquid threat became apparent there was a blanket ban on hand carried liquids. Anyone boarding a flight following the 2006 liquids ban will be only too aware of the problems and frustrations this has caused to passengers. In addition to this the adverse effect on duty free sales, an important revenue stream for airports across the world has been widely publicised [13]. The United States (U.S.) Transport Security Administration (TSA) and the European Civil Aviation Conference (ECAC) both issued urgent requests for new technology in this field.

The TSA requirement is for a Bottle Scanner which can identify the presence of a liquid threat inside a bottle without the need to open the bottle. In order to prevent the build up of queues a single bottle must be measured within 20 seconds. The precise TSA and E.U. screening requirements are classified however common liquid explosives likely to be of concern are discussed in the literature [14,15].

The first stage of the relaxing of the liquids ban will begin in April 2011 and will legally oblige all E.U. airports to have liquid screening capability. From 29th April 2011 transferring passengers from outside the EU will be allowed to carry liquids bought in duty-free shops on to connecting flights within the E.U., ending a restriction that has seen the impounding of duty free goods [16].

The size of the addressable airport security market alone is estimated to be around £485 million and Kromek could generate revenues of up to £72 million over three years, representing approximately 15% of the total market share [17]. In addition to this the applications of the core technology are almost limitless with the potential for screening multiple bottles, and applications not only in the airport security sector but also in customs and border control, and manufacturing quality control to name but a few.

1.4   Scope of Present Work

This thesis is devoted to the design of the x-ray detector system inside Kromek's Bottle Scanner with particular emphasis on pulse height analysis algorithms which are used to generate energy (or pulse height) spectra of the incident x-ray beam. The throughput requirement of bottles at an airport checkpoint requires that the detector must operate at a high count rate in order to achieve the necessary Poisson precision to enable threat identification. This leads to certain design challenges for both the detector and the read out electronics.

One of the major challenges of high count rate operation is dealing with a phenomenon known as pulse pile up. This occurs when two or more x-rays arrive at the detector in close enough succession that the signals overlap in the read out electronics. The convolution of multiple events results in loss of energy and count rate information and becomes more pronounced as the count rate is increased, leading to degradation of the measured energy spectrum.

8"

The other factor affecting the energy spectrum is the incomplete collection of charge from the detector. Chapter 2 deals with the physics relating to the charge transport in a detector and some of the key challenges are outlined. This includes the low drift velocity of the hole signal and the short pulse shaping times required by this application. Methods of overcoming this by modification of the device geometry and electronic correction are discussed along with techniques for dealing with pulse pile up in high count rate systems.

In Chapter 3 a brief overview of the theory behind Kromek's ADMIT^{TM} algorithm for the identification of threat liquids is given. This chapter discusses the choice of detector and electronics used in this work and results from initial tests are shown.

Three pulse height detection algorithms are discussed in Chapter 4 and the performance of each at various count rates is simulated by use of a Monte Carlo model of the random arrival of events at the detector.

Results are shown in Chapter 5 from the implementation of two of the pulse height detection algorithms firstly using emulation on an oscilloscope followed by tests on an field programmable gate array (FPGA). The results are then compared to the modelling work discussed in Chapter 4.

Shortfalls in the algorithms due to incomplete pile up removal and depth of interaction effects are discussed in Chapter 5. These are shown to lead to

7

artefacts in the transmission spectra which present potential problems to a materials identification application. Chapter 6 gives details of an addition to the modelling work in Chapter 4 using the Geant4 software. This allows x-ray interactions to be produced and enables transmission spectra to be simulated by knowledge of the x-ray interaction with a bottle. The results from these simulations are compared to the experimental work in Chapter 5 and validate the findings discussed.

Chapter 7 shows a further improvement to the pulse height detection algorithm which allows improved treatment of pulse pile up and depth of interaction effects by applying what is referred to here as a height-width filtering method which simultaneously removes pulse pile up and corrects depth of interaction effects. The performance of this algorithm is explored using a combination of experimental measurements and simulations.

The concluding chapter provides a summary of all of the key results presented in the preceding chapters and discusses some further work which could build on knowledge gained from this work.

: "

Chapter 2   Scientific Background

2.1   Introduction

This chapter is intended to provide a summary of the basic scientific principles which are applicable to this work and more generally to the field of semiconductor detector physics as a whole. The details of signal formation and propagation in a semiconductor detector are discussed in Section 2.2 followed by a discussion of the charge transport within a detector in Section 2.3.

The detector material of choice in this work is CdTe which suffers from poor hole transport properties. Signal dispersion brought about by this poor hole charge collection efficiency is discussed in Section 2.4 which is shown to result in a depth of interaction effect which can result in the loss of energy information.

The detector read out electronics are discussed in Section 2.5 and an overview of their operation is given along with relevant operational details such as shaping time selection. An understanding of the operational characteristics of the detector electronics is of key importance to the subsequent chapters where the output is used to define pulse height detection algorithms. These are in turn are used to produce pulse height spectra in the Bottle Scanner system.

In Section 2.6 the various methods of dealing with the poor hole collection problem are discussed including modified detector design and electronic correction techniques. As this work is primarily focused on high count rate applications a further problem relating to pulse pile up is discussed in Section 2.7 and existing approaches from the literature are outlined.

2.2   Signal Formation in Semiconductor Detectors

Semiconductor detectors all operate on the same basic principle, interaction with an energetic particle ionises electron hole pairs within the material. These charges are swept out of the material by the application of an electric field. The current or charge signal generated by the movement of the electron hole pairs is then read out by external electronics. A charge sensitive preamplifier is used throughout this work, therefore signals are generally considered in terms of induced charge where the magnitude of the charge generated is proportional to the energy of the incoming photon.

There are three major energy loss mechanisms for photon interactions with a detector [18]. These are:

(1) *The Photoelectric Effect* - all of the photon energy is transferred to an atomic electron. If the photon energy is sufficient to overcome the electrostatic barrier presented by the termination of the crystalline surface (i.e. the work function of the material) an electron is ejected.

(2) *The Compton Effect* - in contrast to the photoelectric effect the photon energy is reduced by the interaction with the detector material producing a 'hot electron' and a Compton shift in the wavelength of the scattered photon.

(3) *Pair Production* - production of an electron-hole pair by the interaction of a photon of energy $> 2m_0c^2$ with the Coulomb field of a nucleus. Where m_0 is the electron mass and c is the speed of light.

Out of the three possible interaction mechanisms, it is only the photoelectric effect which results in complete absorption of the incident energy since a Compton scattered photon or an electron-hole pair may escape the detector volume meaning that all of the energy is not deposited in the detector. In general, the photoelectric effect dominates for photon energies up to $200\,keV$, the Compton effect dominates for energies up to a few MeV and pair production for energies above 6 MeV [19].

Fig 2-1 shows the probability of energy loss by each mechanism as a function of photon energy for CdTe. As energy loss by Compton scattering and pair production is negligible up to 200 keV these effects are generally ignored.
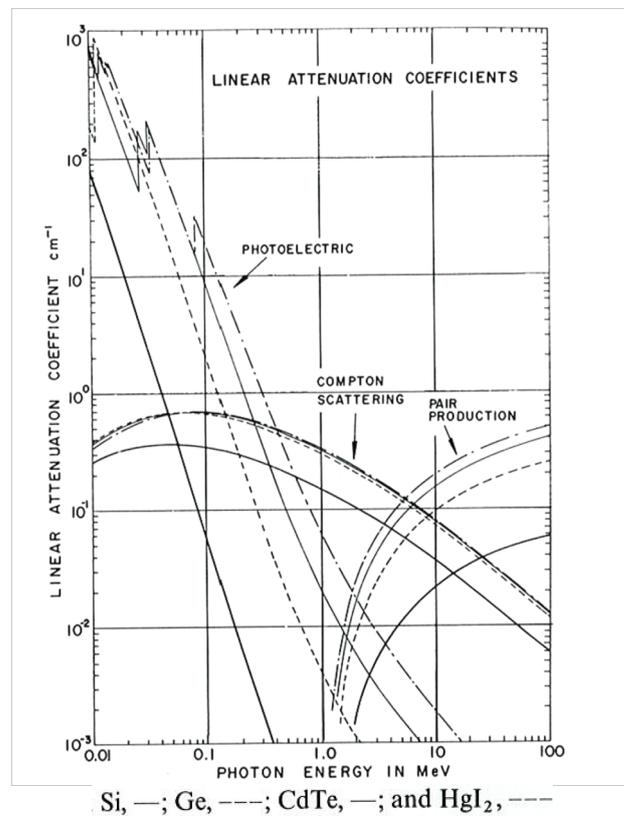
Fig 2-1 Linear attenuation coefficient as a function of energy for CdTe showing the energy regimes for the photoelectric effect, Compton scatter and pair production[20].

34"

No analytical expression exists for the probability of photoelectric absorption for all energies, E_γ and atomic number, Z however an approximation is given by Equation 2-1 [21]:

$$\tau \approx constant.\frac{Z^n}{E_\gamma^{3.5}} \qquad \text{2-1}$$

where the exponent, n, varies between 4 and 5 depending on the photon energy of interest. The higher Z value materials provide a larger photoelectric cross section, thus yielding higher photon detection efficiency.

The number of transmitted photons of a given energy along a path length through a material is described by the Beer-Lambert Law:

$$I = I_0 exp(-\alpha x) \qquad \text{2-2}$$

Here I is the intensity at position x within the material and I_0 is the initial number of photons. The parameter α is the linear attenuation coefficient and is given by the sum of the probabilities of each energy loss mechanism [18]. The linear attenuation coefficient is therefore both energy and material dependent. A higher attenuation coefficient implies a greater probability of interaction with the intervening material and therefore leads to a reduced transmission.

Ionising radiation excites electron-hole pairs in direct proportion to the energy deposited [19]. The number of electron hole pairs, n_0, is given by:

$$n_0 = E_\gamma / \omega \qquad\qquad\qquad\qquad 2\text{-}3$$

Where n_0 is the number of electron-hole pairs, E_γ is the energy deposited by the photon interaction and ω is the ionisation energy which is defined as the average energy required to produce an ionised electron-hole pair [22].

Ionisation requires that an electron must be excited into the conduction band and therefore the width of band gap sets the minimum ionisation energy. For high energy photon interactions where the photon energy is significantly greater than the band gap energy, E_g, the effect of momentum conservation becomes pronounced. This is because the photon momentum is proportional to the photon energy, given by:

$$p = E_\gamma / c \qquad\qquad\qquad\qquad 2\text{-}4$$

For high energy interactions a large proportion of the incident energy must be absorbed via phonon production through lattice vibrations. This results in an ionisation energy which exceeds the semiconductor band gap. The expression below describes the energy required to form an electron hole pair as a function of the band gap energy [23].

$$\omega \approx 2.8 E_g + 0.6 \ eV \qquad\qquad\qquad 2\text{-}5$$

The properties of various commonly used semiconductor materials are tabulated in Table 2-1. The suitability of a detector for a given application is governed by

36"

many factors including the stopping power which is given by the mean atomic

number, Z, of the constituent elements and the ionisation energy range which is a

function of the band gap.

Material	E_g (eV)	ω (eV)	ε	μ_e	μ_h	$\mu\tau_e$	$\mu\tau_h$	Z
CdTe	1.44	4.43	10.9	1100	100	3.10^{-3}	2.10^{-4}	50
Cd$_{0.9}$Zn$_{0.1}$Te	1.572	4.64	10	1000	120	4.10^{-3}	$1.2.10^{-4}$	49.1
GaAs	1.43	4.2	12.8	8000	400	8.10^{-5}	8.10^{-6}	31.5
Ge	0.67	2.96	16	3900	1900	> 1	> 1	32
Si	1.12	3.6	11.7	1350	450	> 1	> 1	14

Table 2-1 Some key material properties[22] for semiconductors commonly used in radiation detection. Mobilities, $\mu_{e,h}$ are given in units of $cm^2 V^{-1} s^{-1}$ and mobility-life time products, $\mu\tau$ are given in units of $cm^2 V^{-1}$.

The replacement of 10-20% of the cadmium in CdTe with zinc to form CdZnTe

results in a wider band gap which reduces the intrinsic free carrier concentration

and the leakage current[24] below that expected for binary CdTe. This yields

enhanced detection performance at room temperature when compared to binary

CdTe [25, 26]. The high atomic number of constituent elements in both CdTe and

CdZnTe and high density give a high photoelectric cross section for photon

energies below 180 keV [27].

CdTe has a bandgap of 1.44 eV [28] and ZnTe has a band gap of 2.0 eV [28].

Variation of the zinc composition allows the bandgap to be tuned. It has been

found empirically by Olega et al [29] that the bandgap is given by:

$$E_g(x) = 1.510 + 0.606x + 0.139x^2 \ eV \tag{2-6}$$

where x defines the atomic fraction of Zn in the relation $Cd_{1-x}Zn_xTe$.

This yields a high resistivity $(10^{10} - 10^{11} \ \Omega cm)$ [26] ternary semiconductor with a bandgap of around $1.6 \ eV$ depending on zinc composition. The introduction of zinc also strengthens the lattice due to its shorter bond length [30].

The low leakage current of both CdTe and CdZnTe is essential for low noise operation and is a desirable characteristic where power consumption is a primary concern i.e. in the fabrication of low power detectors for hand held devices and astrophysical instrumentation [27].

2.3   Charge Transport in a Detector

Charge is generated within the detector by interaction with an ionising particle of energy greater than or equal to the ionisation energy, ω. The charge then drifts under the influence of an applied electric field towards the contacts.

The underlying physics of charge transport in a detector can be expressed by taking a particular case where the detector is composed of a perfect dielectric medium with uniformly spaced plane parallel contacts separated by a distance, d. The more general treatment is given by the use of the Shockley[31]-Ramo[32] theorem and is reported widely in the literature [33,34,35].

The detector geometry is illustrated in Fig 2-2. Here it is assumed that the separation of the contacts is small compared to the length and width of the detector allowing edge effects to be ignored.
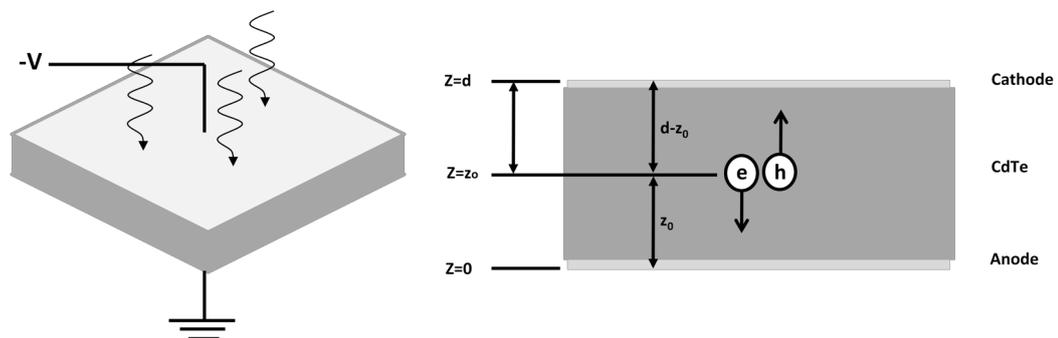
Fig 2-2 Diagram showing a planar detector with an applied bias voltage, -V. The cross section illustrates the generation of electron-hole pairs due to absorption of ionising radiation. The electrons and holes then drift towards the contacts under the influence of the electric field.

If the point of interaction of an ionising particle is defined as z_0, the distance of the charges generated by this interaction from the respective electrodes is shown in Fig 2-2. Assuming full depletion, the electric field, E across the device is:

$$E = \frac{V}{d}$$
<div align="right">2-7</div>

where d is the device thickness and V is the applied voltage.

If a negatively charged electron and a positively charged hole are placed at position z_0 within the detector, the charges will be swept out towards the respective contacts under the influence of the electric field. After a time t, the electron will drift a distance $z = v_e t$ towards the anode and the hole will drift a distance $z = v_h t$ towards the cathode, where v_e and v_h are the electron and hole velocities respectively. The effect of an electron moving in a positive direction is the same as a hole moving in a negative direction as the charges are of opposite sign. This means that the directional component of velocity can be ignored.

For a plane parallel detector, the charge induced on the electrodes by the drift of electrons and holes is given by:

$$Q_I(t) = \frac{Q_0 t}{d}(v_e + v_h)$$
<div align="right">2-8</div>

where $z_0 > v_e t$ and $d - z_0 > v_h t$.

3: "

Once the charges have drifted to the readout electrodes, the induced charge becomes equal to the total charge, at which point the signal becomes constant at a level defined by the initial charge, Q_0. The ratio of electron and hole contribution to the total induced charge is defined by the distance moved by each carrier type. For a charge created at an arbitrary position, z_0 within the detector and in the absence of charge trapping, the induced charge by electrons and holes is given by:

$$Q_e = \frac{Q_0}{d} z_0 \qquad\qquad \text{2-9}$$

$$Q_h = \frac{Q_0}{d}(d - z_0) \qquad\qquad \text{2-10}$$

For low to moderate electric field intensities the electron and hole velocities are given by [22]:

$$v_{e,h} = \mu_{e,h} E = \frac{\mu_{e,h} V}{d} \qquad\qquad \text{2-11}$$

2.4 Signal Dispersion

The magnitude of the induced charge (or current) is the key parameter in determining the absorbed energy from incident radiation. Fluctuations in signal magnitude can occur for a number of reasons including charge trapping and variation in the depth of interaction of the radiation. These effects lead to uncertainty in the incident energy of ionising radiation which is detrimental to detector performance and must be corrected for.

2.4.1 Charge Trapping

The simplified model in Section 2.3 considers the effect of the movement of charge within a perfect dielectric. The final charge induced on the contacts, Q_I, is therefore equal to the charge generated by a photon interaction within the material, Q_0 where:

$$Q_0 = n_0 e = \frac{E_\gamma}{\omega} e \qquad\qquad \text{2-12}$$

If the electric field is assumed to be constant across the device, the velocity of electrons and holes is dependent on their respective mobilities and is given by 2-11.

In CdTe the hole mobility is much lower than the electron mobility ($1100\ cm^2 V^{-1}$ for electrons compared to $100\ cm^2 V^{-1}$ for holes [22]) resulting in

20

a lower drift velocity and therefore longer collection time across the depletion region within the detector. Taking the example of a planar detector as outlined in Section 2.3 charge is lost in the dielectric region between the point of creation and the point of collection. This effect is known as charge trapping and arises from imperfections in the crystal lattice introduced during growth, fabrication or by radiation damage during operation. The total electron or hole charge remaining after a time, t, is given by:

$$Q(t)_{e,h} = Q_0\, exp\left(-t/\tau_{e,h}\right)$$ 2-13

where τ is the mean carrier lifetime, which is a measure of the average time before trapping or recombination occurs. As this is a function of the trap density this parameter varies depending on the defect density in a given detector.

The remaining untrapped charge which is available for signal contribution falls as a function of time. The charge induced at the contacts becomes lifetime dependant and is given by integrating Equation 2-8 over the drift time of the electrons and holes to the anode and cathode respectively:

$$Q_I(t) = \frac{Q_0}{d}\left(v_e\tau_e.\left[1 - exp\left(-\frac{t}{\tau_e}\right)\right] + v_h\tau_h.\left[1 - exp\left(-\frac{t}{\tau_h}\right)\right]\right),$$ 2-14

where τ_e and τ_h are the lifetimes of electrons and holes respectively.

At $v_e t \geq z_0$ and $v_h t \geq (d - z_0)$ the remaining charge is completely read out and the induced charge reaches a maximum of:

$$Q_I = \frac{Q_0}{d}\left(v_e\tau_e\left[1 - exp\left(-\frac{z_0}{v_e\tau_e}\right)\right] + v_h\tau_h\left[1 - exp\left(-\frac{(d - z_0)}{v_h\tau_h}\right)\right]\right) \qquad \text{2-15}$$

The collection time of the electrons and holes to the contacts is a function of the interaction position, z_0, and the electron and hole velocities. The electron and hole velocities are in turn a function of the mobility and the applied electric field given by 2-11.

Higher electric fields therefore result in less charge trapping as the carriers spend less time in the vicinity of traps. Rewriting 2-15 highlights the bias dependence of the induced charge signal.

$$Q_I = \frac{Q_0 V}{d^2}\left(\mu_e\tau_e\left[\left(1 - exp\left(\frac{-z_0 d}{\mu_e\tau_e V}\right)\right)\right]\right) + \cdots \qquad \text{2-16}$$

Rearranging Equation 2-16 gives an equation in a more familiar form known as the Hecht Equation[36]. Here the value Q_I/Q_0 is referred to as the charge collection efficiency (CCE) of the detector. It is shown here as the single carrier form where the creation of the charge is assumed to be at the cathode, resulting in induced charge from the electrons only.

$$\frac{Q_I}{Q_0} = \frac{\mu_e\tau_e V}{d^2}\left[1 - exp\left(\frac{-d^2}{\mu_e\tau_e V}\right)\right] \qquad \text{2-17}$$

The parameter $\mu_e \tau_e$ in Equation 2-17 is known as the electron mobility-lifetime product. The Hecht equation is not independently solvable for mobility or lifetime and therefore the mobility-lifetime product forms a key parameter in characterising charge transport properties of semiconductor detectors. Measurement of the mobility-lifetime product is typically carried out using alpha particle irradiation [37]. Due to their shallow depth of interaction (a few microns) the signal is comprised of only one carrier type and in the case of cathode irradiation the approximation $z_0 = d$ can be made. Measurements of the mobility-lifetime product are then carried out by fitting 2-17 to a plot of the alpha peak centroid as a function of bias voltage, referred to as a Hecht Plot.

Fig 2-3 shows the induced charge as a function of time from electrons and holes generated at the centre of the detector as they drift towards the collection electrodes. This graph illustrates the importance of achieving good charge collection efficiency as the pulse height read out from the detector for a given photon energy is dependent on the amount of charge trapping which occurs in the detector. Operation at charge collection efficiencies below 100% therefore results in a loss of pulse height information. As the pulse height is proportional to the impinging photon energy, this in turn leads to an uncertainty in the detected photon energy.
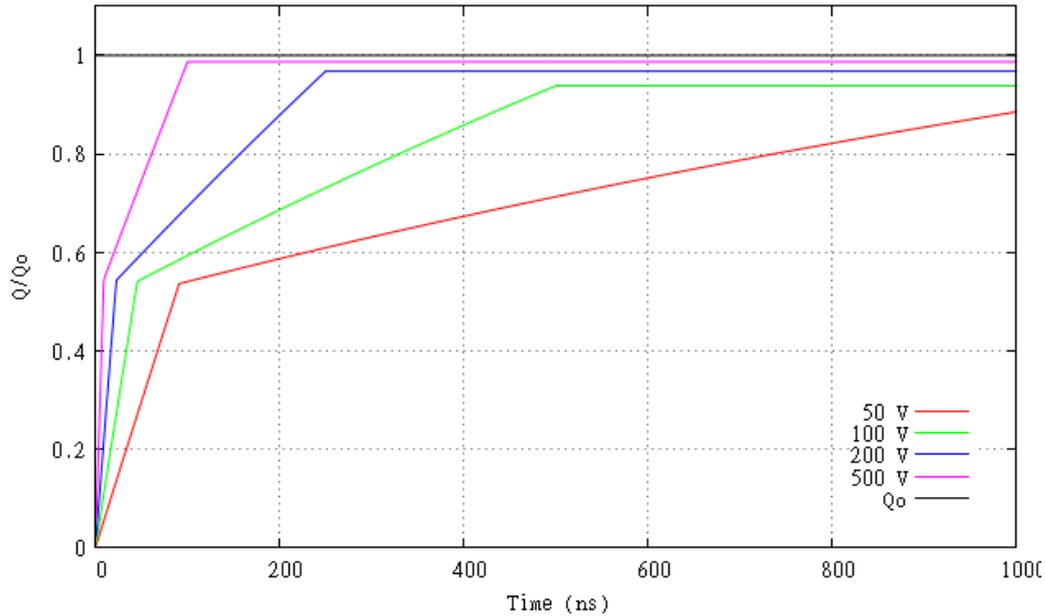
Fig 2-3 Graph showing the bias voltage dependence of the magnitude of the induced charge signal. Here the variation in amplitude is primarily due to the trapping of holes as they move a distance $z = d/2$ to the cathode. The detector thickness is 0.1 *cm* and the mobility lifetime product of electrons and holes is 3×10^{-3} *cm^{2}V^{-1}* and 2×10^{-4} *cm^{2}V^{-1}* respectively.

As the depth of interaction is a probability function defined by 2-2, in a real system photons of the same energy will have differing interaction depths. This results in a variation in signal amplitude for mono energetic radiation which leads to uncertainty in the energy of the radiation incident on the detector. Without knowledge of the depth of interaction of the radiation this signal amplitude information is not recoverable. In absence of this knowledge it is desirable that the detector response is depth of interaction independent. This requires that the charge signal can be fully read out from any depth within the detector without any loss of charge. In addition to this, the signal rise time must be sufficiently fast to be read out within the acquisition time of the read out electronics.

This phenomenon presents a problem for spectroscopy applications where the magnitude of the convoluted electron and hole signal is used to define the energy of the incident photon. When a pulse height spectrum is formed, variation in pulse height results in a dispersed energy peak, in turn producing an asymmetric tail on the low energy side of the peak. This effect is known as hole tailing and arises due to the poor hole transport properties which result in less than full height pulses.

2.5 Read Out Electronics

A typical detector system is shown in Fig 2-4. The signal from the detector is read out by a preamplifier followed by a shaping amplifier. The height of each shaped pulse is measured using a MCA.
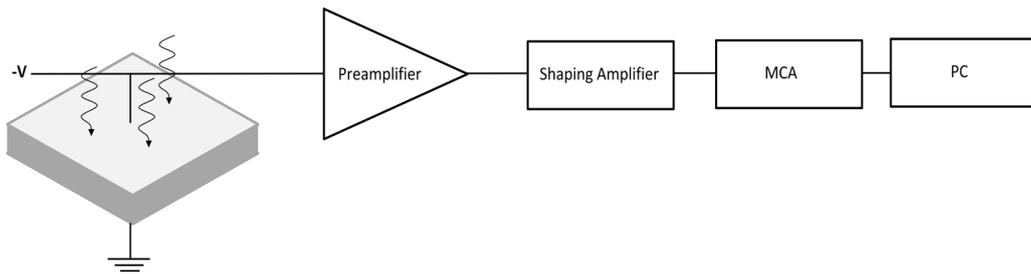
Fig 2-4 Diagram showing a typical semiconductor detector system consisting of detector, preamplification and shaping stages and pulse height analysis via a MCA and PC.

Pulses are then added to a histogram where the pulse height is recorded on the x-axis, referred to as the bin number, and the y-axis records the number of counts in each bin. The bin number is proportional to the energy of the detected event

with the proportionality constant defined by the gain of the system and the number of electron-hole pairs produced in the detector.

2.5.1 Preamplifier

The charge created by a photon interaction with CdTe is very small (of the order of a few fC). For CdTe with an ionisation energy of $4.43\ eV$ per electron-hole pair this equates to just 2.3×10^4 electron-hole pairs at an energy of $100\ keV$ meaning a high gain preamplification stage is needed before any signal processing can begin. This part of the signal chain is the most critical due to the high gain required. Noise ingress at this stage has the potential to completely mask out the signal. The preamplifier therefore provides a very high gain, low noise amplification. This is done by use of a charge sensitive or voltage sensitive preamplifier.

In voltage sensitive preamplification, the output voltage is proportional to the charge generated by the incident radiation for an assumed fixed detector capacitance. Any change in input capacitance affects the constant of proportionality between output voltage and induced charge. This is undesirable as instability in the detector or connecting circuit can lead to changes in the output voltage.

The alternative and more desirable approach for semiconductor detectors is to use a charge sensitive preamplifier which is largely insensitive to changes in input capacitance[21]. It is for this reason that a charge sensitive rather than voltage sensitive preamplifier was selected for this application. A schematic diagram of a charge sensitive preamplifier is shown in Fig 2-5.
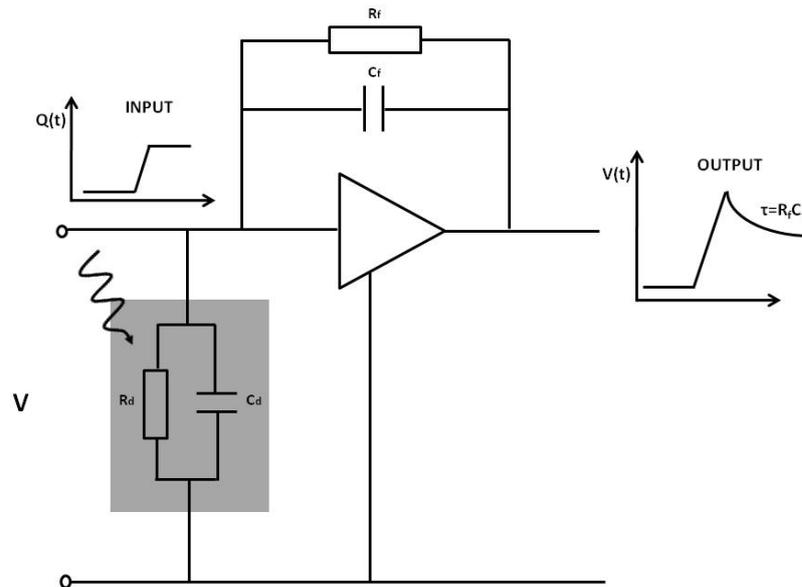
Fig 2-5 Schematic diagram of a charge sensitive preamplifier showing the input signal, $Q(t)$ and the output signal, $V(t)$. The exponential decay of the output signal is defined by the time constant, τ of the feedback resistor and capacitor C_f and R_f respectively.

From Fig 2-5 it can be seen that the fast rising edge of the square wave pulse has been maintained by the preamplifier while the pulse amplitude has been increased. The time constant of the decay of the pulse beyond the point where the charge signal flattens off is defined by the feedback capacitor and resistor C_f and R_f respectively.

Whilst it is not a requirement that the rising edge of the pulse starts at a defined voltage, continual step increases in the DC level of the output would eventually result in the preamplifier reaching saturation. A feedback resistor must therefore be selected in order to bleed off the charge. The selection of the feedback resistor value is generally made with reference to the detector rise time and is selected to provide a large enough time constant to allow the longest rise time signals to reach maximum amplitude without significant decay.

2.5.2 Pulse Shaping

Some detector systems directly sample and digitise the preamplifier signal but in most cases some form of analogue pulse shaping is used prior to the analogue to digital conversion stage. Pulse shaping serves a number of purposes including:

1. Minimising the noise contribution to the signal output by filtering with an optimised bandwidth;

2. Signal amplification to a usable level;Formation of a slow rate of change peak in order facilitate sampling by an analogue to digital converter;

3. Preservation of proportionality between radiation energy and signal amplitude with correct pulse shape selection.

The most common pulse shaping method is the use of a passive CR-RC network which produces a Gaussian type pulse shape where the CR component is a high pass filter (differentiator) and the RC component is a low pass filter (integrator) and is used throughout this work.

The selection of the value of the resistors and capacitors, *R* and *C* define the time constants of the filters, τ. This in turn defines the shape of the output signal and the signal to noise characteristics. A simple CR-RC network is shown in Fig 2-6. Here the input is shown as a step voltage which is characteristic of a typical preamplifier output. The falling RC component has not been considered as this is typically long compared to the time constants of the shaping network.
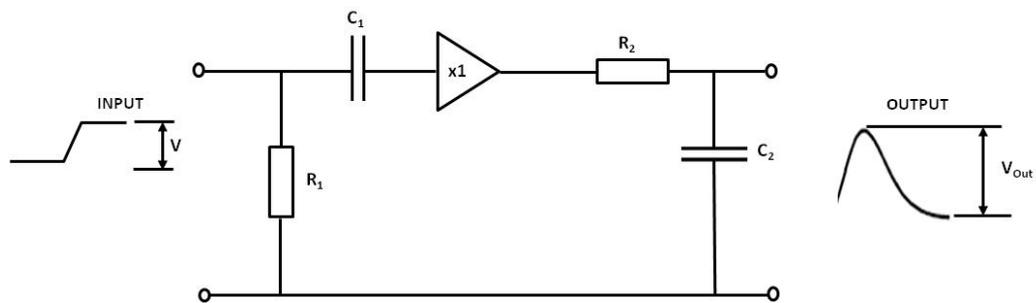
Fig 2-6 Schematic diagram of a simple CR-RC network. The unity gain buffer amplifier separates the filter stages for impedance isolation.

The general solution to a CR-RC network to a step voltage, *V*, is given by [21]:

$$V_{Out}(t) = \frac{V\tau_1}{\tau_1 - \tau_2}\left(e^{-t/\tau_1} - e^{-t/\tau_2}\right)$$

2-18

where $V_{Out}(t)$ is the output amplitude as a function of time and τ_1 and τ_2 are the time constants of the filter networks defined by C_1R_1 and C_2R_2 respectively.

The selection of τ_1 and τ_2 defines the so called shaping time of the amplifier circuit, which is defined as the time equivalent of the standard deviation of output pulse [38]. The addition of further differentiation stages to form a $CR-(RC)^n$ network results in a near Gaussian pulse shape which has a shorter return

time to the baseline. This symmetrical pulse shape is advantageous in high count rate applications due to the narrower total base width. If τ_1 and τ_2 are equal, the shaping time is defined by $n\tau$. This particular solution is given by [21]:

$$V_{Out}(t) = \frac{V}{n!}\left(\frac{t}{\tau}\right)^n e^{-t/\tau} \qquad \text{2-19}$$

Owing to the Gaussian shape produced by this type of network, this form of pulse shaping is known as Gaussian pulse shaping and has the added advantage of further noise suppression when compared to a simple CR-RC network. For this reason Gaussian pulse shaping is used in this application.

2.5.3 Shaping Time Selection

Two key considerations in shaping time selection are the preservation of proportionality between the preamplifier and shaping amplifier pulses, and minimisation of pulse pile up. These considerations set two conflicting requirements on the shaping time.

The first requires that the shaping time must be large in order to ensure that the preamplifier output has sufficient time to reach maximum amplitude. Shaping times comparable to or less than the preamplifier signal rise time results in a loss of signal height. This effect is known as 'ballistic deficit' [39] and results in loss of pulse height information. The amount of ballistic deficit observed on a given pulse is a function of the signal rise time which as previously discussed is a

function of both the charge transport properties of the signal charge and the depth of interaction within the device. This leads to a continuously variable pulse height deficit which degrades spectral resolution making operation in a ballistic deficit regime very undesirable.

The second requirement suggests that shorter shaping times are preferable as these result in a narrower base width which reduces the probability of pulse pile up, a phenomenon which is of particular concern at high count rates. The most appropriate shaping time selection for a particular application is generally found empirically and emerges from a trade off between these two requirements and any additional noise filtering requirements. These requirements clearly reinforce the need to achieve fast signal rise times from the detector.

In the case of a detector with widely differing rise times, for example in a large volume detector where the depth of interaction may vary widely, a trapezoidal pulse shaper is often a preferred approach. This technique is commonly used in large volume Germanium detectors [40]. The addition of a flat top results in a shaper which is less sensitive to signal rise time and therefore removes the problem of variable ballistic deficit.

2.5.4 Noise Considerations

Noise is present in all detector systems to some degree and produces undesirable baseline fluctuations which appear superimposed on the output signal. In the case of pulse height analysis this serves to distort the measured height and therefore energy of a given event. In addition to signal fluctuations from the detector such as charge trapping, the presence of noise places a limit on the minimum detectable energy. The presence of noise also leads to reduced energy resolution due to broadening of the energy peaks. It is therefore critical that the detector and electronics are designed in order to maximise the signal to noise ratio.

Noise has a Gaussian amplitude distribution and therefore unlike charge trapping results in a symmetrical broadening of energy peaks in a pulse height spectrum. The noise frequency spectrum is broad and generally assumed to be 'white' i.e. having a uniform frequency distribution. Fundamental noise sources exist in all nuclear pulse amplifiers where very high input impedances are used to match the high detector impedance. Sources of noise in a detector system can be defined as either voltage noise due to noise sources which are effectively in parallel with the input or current noise from those which are in series with the signal source.

Noise in the detector system can be described by random fluctuations in the number and velocity of carriers in the circuit. These two mechanisms are statistically uncorrelated and therefore add in quadrature to form the total fluctuation in current. Velocity fluctuations are due to random thermal motion

superimposed on the drift velocity of carriers. Number fluctuations, termed 'shot noise' occur in many circumstances and are due to sources such as thermionic emission over a barrier. Fig 2-7 (left) shows a schematic diagram of a typical detector circuit and the equivalent circuit for noise analysis (right) where voltage and current sources are used to describe the noise at each point.
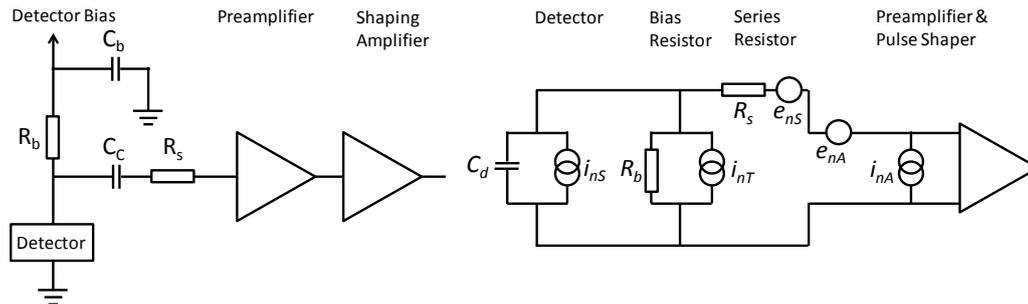
Fig 2-7 Schematic diagram showing a typical detector circuit (left) and the equivalent circuit for noise analysis (right).

The noise in the preamplifier and shaping amplifier is described by a current source, i_{nA} and a voltage source, e_{nA}. Equation 2-20 describes the spectral current noise density, i_{nT}^2, of thermal (Johnson) noise.

$$i_{nT}^2 = \frac{4kT}{R} \qquad \text{2-20}$$

Where R is the resistance, T is the temperature and k is Boltzmann's constant. This can also be described as a noise voltage, given by:

$$e_{nT}^2 = 4kTR \qquad \text{2-21}$$

The spectral noise density of Shot noise is described by Equation 2-22.

$$i_{nS}^2 = 2eI \qquad \text{2-22}$$

Where I is the average current and e is the electronic charge.

Trapping and detrapping processes in resistors, dielectrics and semiconductors can introduce additional voltage fluctuations whose noise power typically exhibits a $1/f$ spectrum. The spectral density of this so called '$1/f$' noise is given by:

$$e_f{}^2 = \frac{A_f}{f} \qquad\qquad \text{2-23}$$

Where the noise coefficient A_f is device specific[22] and of the order of $10^{10} - 10^{12}\ V^2$ and f is the noise frequency.

Noise is typically characterised in terms of an equivalent noise charge (ENC) which is defined as the signal charge which yields a signal to noise ratio of 1. As noted in Section 2.5.2 one objective of pulse shaping is to filter the noise from the output of the preamplifier. This is done by varying the shaping time of the amplifier in order to tailor the noise response. Various pulse shaping methods exist which offer superior noise filtering performance to that achieved by Gaussian pulse shaping however other factors such as the rapid return of the pulse to the baseline and the low rate of change at the peak make Gaussian pulse shaping the most desirable for this application.

The equivalent noise charge for the circuit in Fig 2-7 is given in Equation 2-22 and assumes equal time constants for the differentiation and integration stages of the shaping amplifier [22].

$$Q_n{}^2 = \left(\tfrac{e}{8}\right)\left[\underbrace{\left(2eI_d + \tfrac{4kT}{R_b} + i_{na}{}^2\right).\tau}_{\text{Current Noise}} + \underbrace{(4kTR_s + e_{na}{}^2).\tfrac{C^2}{\tau}}_{\text{Voltage Noise}} + \underbrace{4A_f C^2}_{1/f\ \text{Noise}} \right] \qquad \text{2-24}$$

Fig 2-8 shows a plot of the ENC and it can be seen that the contribution from current noise increases with shaping time, voltage noise decreases with shaping time and $1/f$ noise is independent of shaping time. This leads to the minimum where the contributions from current and voltage noise are equal and represents the ideal operating condition from a noise perspective.
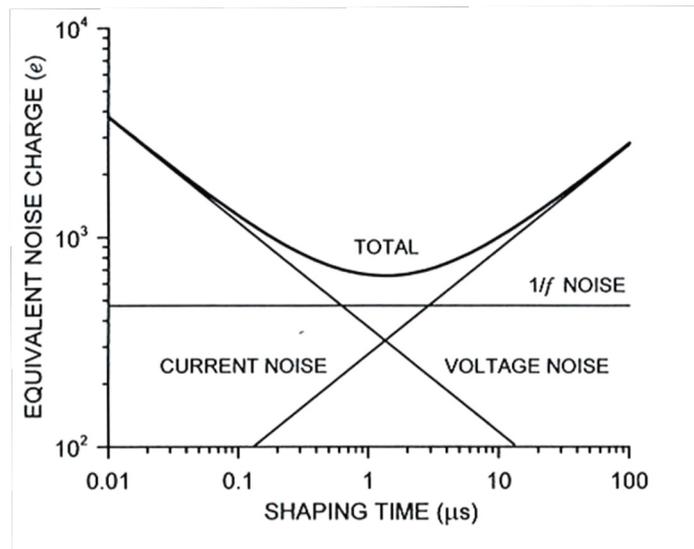
Fig 2-8 Diagram showing ENC as a function of shaping time [22] for a typical detector system as outlined in Fig 2-7.

Clearly other factors affect the shaping time selection including the rise time of the preamplifier signal and the operating count rate. This requires a compromise to be made which depends on the requirements of the application. For the purposes of this application the shaping time is primarily chosen on the grounds of count rate and ballistic deficit and the noise is minimised by appropriate design of the detector signal chain.

2.6 Solutions to Poor Hole Charge Collection

As previously discussed, charge induced on the contacts of a planar device is proportional to the distance moved by the carriers and neglecting charge trapping increases linearly during the entire collection time of the carriers to the contacts. For certain device geometries the charge signal is only induced when the charge cloud is very close to one of the collecting electrodes. Charge induced due to movement throughout the rest of the detector volume is negligible. This is beneficial in dealing with the problem of poor hole charge collection efficiency as, if the anode is defined as the sensitive electrode, the device is insensitive to the heavily trapped hole signal. This results in an electron only signal which has previously been shown to be completely collected under most bias conditions. This therefore restores the proportionality of pulse height to the energy of the ionising radiation.

As the charge is only induced when the electron cloud is in close proximity to the anode, resulting signals have rise times which are much shorter than the actual transit time of the charge to the collection electrode.

A wide range of detector geometries have been devised in order to reduce the sensitivity to the hole signal. Among the most widely discussed in the literature are the Coplanar Grid detector [41,42], Frisch grid collars [43] and the Small Pixel detector[44]. All three geometries report significant improvements when compared to a planar detector.

36

2.6.1 Electronic Compensation Techniques

An alternative to geometrical type approaches is to use an electronic compensation technique. Such methods are broadly referred to as biparametric (BP) correction techniques as they measure both the rise time and height of a pulse [45]. Typically signals with long rise times will be due to interactions near to the cathode region and therefore suffer significant loss in pulse height due to trapping. With knowledge of the rise time and pulse height information, pulses can then be simply filtered by a rise time discrimination technique or a more sophisticated compensation approach [46] can be used by applying an appropriate correction factor in order to reconstruct the correct pulse height.

Mestais et al [47] have reported the design of front end electronics and an ASIC for large volume (6 mm thick) imaging detectors. The 3D view of the BP [57]Co spectrum is shown in Fig 2-9.
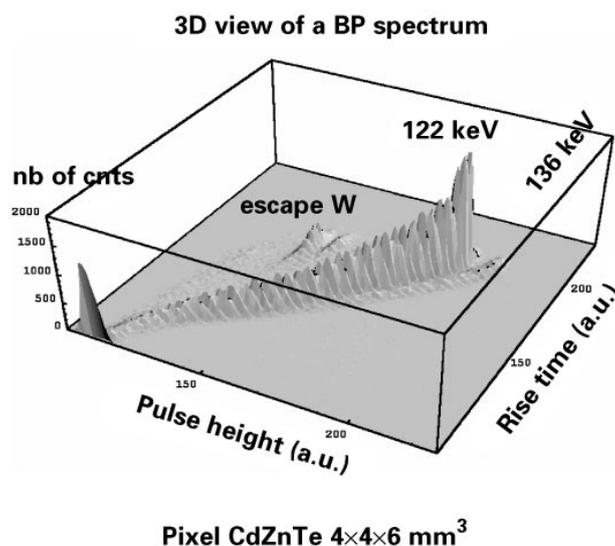
Fig 2-9 Biparametric spectrum from a [57]Co source [47].

The correction technique involves first producing a two dimensional plot of rise time as a function of pulse height. Compensation can then be carried out by fitting a polynomial to the empirical relationship between pulse height and rise time and shifting long rise time events accordingly. Such a technique is reported to show promising results in imaging applications, however the typical reported count rates are of the order of 200 counts per pixel per second which is clearly not suitable for an x-ray application. A new approach to this type of electronic correction will be discussed in Chapter 7.

2.7   Spectral Degradation Due to Pulse Pile Up

Perhaps the most detrimental effect to the resolution of a detector in this particular application is the effect of pulse pile up at high count rates. This will be dealt with in detail in the following chapters. Pulse pile up arises due to the random nature of photons arriving at the detector and can lead to interfering effects between two or more pulses. The effect of pulse pile up on the spectrum is twofold, firstly the height of each of the interfering pulses may be incorrectly measured and secondly for closely interfering pulses the absolute number of pulses may be difficult to discern, leading to counting losses. This clearly becomes more of a problem at high count rates but is also observed at low count rates due to the non zero probability of pulses arriving within the time window defined by the base width of the shaped pulse.

Most pulse height analysis systems broadly fall into one of two categories known as paralyzable or non paralyzable systems [48]. Paralyzable behaviour describes a system with a dead time, d, which follows the arrival of each event. This dead time is extended by d following the arrival of each subsequent pulse, thereby preventing the system from counting further pulses until the total dead time for the entire pulse chain has elapsed. In a non paralyzable system counts appearing during the dead time period following the arrival of an event are lost. This results in a system where the total dead time is only defined by the sum of the individual dead times which follow each recorded event.

The recorded count rate as a function of the input count rate for paralyzable and non paralyzable systems is given in Equations 2-25 and 2-26 respectively. Where m is the recorded count rate, n is the input count rate and d is the system dead time (shaped pulse width) [21].

$$m = ne^{-nd} \qquad\qquad\qquad\qquad \text{2-25}$$

$$m = \frac{n}{1 + nd} \qquad\qquad\qquad\qquad \text{2-26}$$

Plotting Equations 2-25 and 2-26for a dead time of $560\ ns$ [i] the two models shown in Fig 2-10 can be seen to significantly deviate from the ideal $m = n$ case at count rates above 200,000 to 300,000 counts per second (cps).

---

[i] The use of a dead time of $560\ ns$ is due to the choice of electronics which is discussed in the following section.
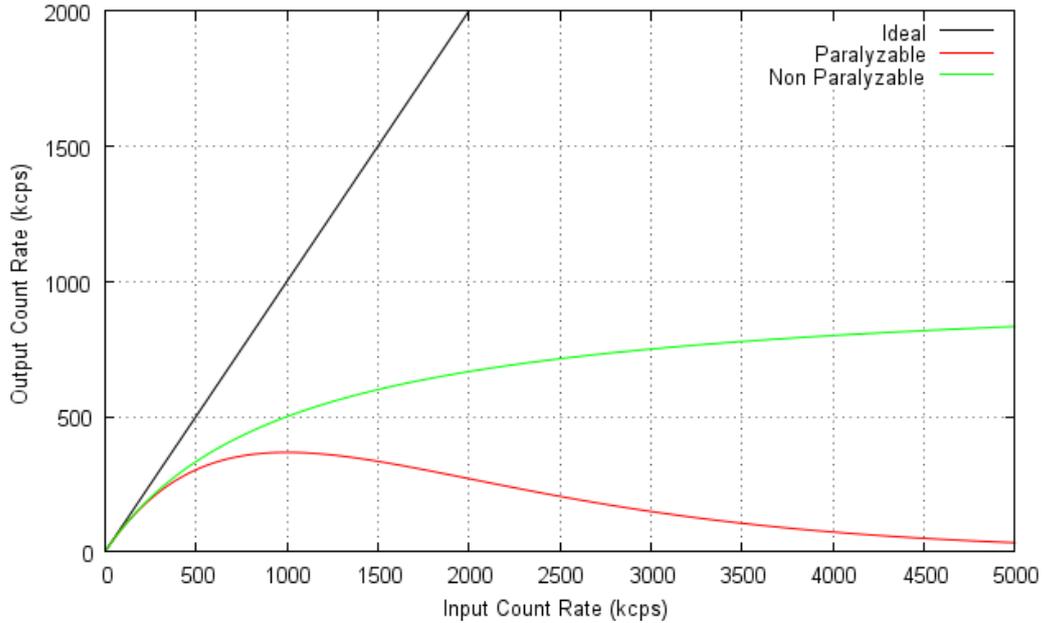
Fig 2-10 Output count rate as a function of input count rate for both paralyzable and non paralyzable pulse height detection systems. Here the dead time for both systems is 560 *ns* which is defined by the width of each pulse.

As expected from Equations 2-25 and 2-26 both paralyzable and non paralyzable curves show a continuous deviation from the ideal case even at very low count rates. This illustrates the finite probability of two or more counts arriving at the detector within the same time window defined by the dead time for a single count.

A number of techniques are described in the literature for dealing with counting losses. Live time clock correction is possibly the simplest method of count loss correction and involves the use of a live time clock which measures the time periods during which the system is sensitive to an incoming event. The true count rate can then be inferred from the total acquired counts divided by the live time. This works well at low to moderate count rates [49] but is not suited to situations

where live times become small with respect to real time. The inaccuracy inherent in this technique is the reliance on the acquired spectrum in order to infer the true incident count rate. In addition to this, such a method does not deal with energy distortion resulting from piled up events which are included in the live time spectrum.

A similar approach can be taken by use of a random pulse generator. In this method a random test pulse of known amplitude is injected into the preamplifier stage during a measurement, resulting in a random mixture of pulses. As both types of pulse will be equally affected by pulse pile up, the loss of counts in the pulser peak formed by the MCA will give a measure of the percentage loss of real pulses. Again this technique does not deal with energy distortion and has the additional complexity of requiring a random test pulse which accurately simulates the pulses received from the detector.

More sophisticated methods of live time correction include the loss free counting (LFC) technique which is used in the Canberra Model 599 Loss Free Counting Module and the Gedcke-Hale method [50] which is used in the Ortec DSPEC[PLUS]. A comparative study of the performance of these systems was carried out by Makarewicz and Burns [51]. Both methods are effective at allowing the determination of peak position and peak area in gamma-ray spectroscopy where peaks are generally discrete. The difficulty in application to an x-ray spectrum is that the photon energies are from the bremsstrahlung continuum making it

impossible to identify wrongly binned counts simply by inspection of the output spectrum.

Other approaches outlined in the literature [52,53] involve the deconvolution of pulses in order to restore the original pulse shape of piled up events. This type of approach is preferable to simple count loss correction as the energy information from each pulse is retained.

2.8   Summary

In this chapter a summary of the scientific background to semiconductor detector physics have been outlined. The principles discussed here form a foundation for the results discussed in the following chapters.

A description of the signal formation and propagation as the electrons and holes move through the material under an applied electric field has been given. The effect of charge trapping on electrons and holes results in an undesirable signal variance. This has been shown to be most pronounced in the hole component of the signal due to the lower mobility and lifetime of holes. Under certain conditions this introduces a depth of interaction dependence to the signal magnitude due to variation in charge trapping.

Increased bias voltages are shown to reduce trapping however this results in an increase in leakage current which is detrimental to the signal to noise ratio. Various methods have been developed in order to resolve the depth of interaction problem including electrode geometries and electronic correction techniques which have been outlined.

The main elements of detector electronics have also been outlined along with some important operational notes such as the selection of shaping amplifier shaping time and the effect of electronic noise and ballistic deficit on the signal

output. These are common to most semiconductor detector systems and are used in the work discussed in subsequent chapters.

Finally the phenomenon of pulse pile up was discussed which will be shown in the following chapters to be highly significant in optimising the Bottle Scanner system performance. Paralyzable and non paralyzable counting systems were discussed and it was shown that both give significant deviations from linearity at high count rates. Whilst this treatment describes the counting losses from such systems, the change in spectral shape due to pile up is not considered and as will be shown in the following sections is of key importance for the Bottle Scanner application.

Chapter 3   The Bottle Scanner System

3.1   Introduction

In this chapter an overview of the Bottle Scanner system is given along with a description of the basic methods used for liquid threat detection. Liquid threat detection is not the focus of this work, however, this brief discussion gives an appreciation of the challenges faced in the design of pulse height detection algorithms discussed in subsequent chapters. The particular challenges relate to the requirement for a high throughput of counts which results in shaped pulses piling up.

A description of the detector and electronics used for this work is given, including a description of the FPGA which is used in this application to perform the operation of a MCA. Key characteristics of the shaped output signal are also shown including an ideal shaped pulse from a square wave test pulse input. A function is fitted to this trace and is used in the simulation work discussed in Chapter 5. Also shown is the electronic noise floor of the system which limits the minimum detectable pulse energy.

A low count rate spectrum acquired using a ^{57}Co source and a commercially available Canberra Multiport II MCA is shown and will be used in Chapter 5 as a reference from which to compare the performance of pulse height detection algorithms developed.

Finally the effect of high input count rate on the shaping amplifier and preamplifier outputs is shown by irradiation of the detector with a beam of x-rays. This highlights the problems of pulse pile up in the shaping amplifier which are simulated in the subsequent chapter.

3.2   An Overview of Liquid Threat Detection using the Multi-Spectral Analysis of X-rays

In this section a brief overview of the basic technique of materials identification will be discussed. The full details of the ADMIT algorithm are confidential and not relevant to this work however it is necessary to describe some of the underlying principles in order to understand the basis behind the detector system design.

The liquid threat identification technique is an energy dispersive technique based on the material specific interaction of x-rays with matter. An x-ray beam is fired at the liquid under test and the absorption/transmission of x-rays through the liquid as a function of energy gives a signature which is unique to the elemental constituents of the material in the beam, i.e. the liquid and container walls.

The x-ray generator used in this application has a bremsstrahlung energy spectrum which extends from 0 to 160 keV. The principle modes of energy loss for photon interactions at these energies are via elastic scattering, Compton scatter or photoelectric absorption [20]. The attenuation of x-rays is therefore sensitive to both the atomic number and electron density of the absorbing medium and is described by the Beer-Lambert law (2-2).

This is a material specific parameter which varies as a function of the mass fraction of each of the contributing elements and as a function of the energy of incident x-rays. Further details of the full treatment can be found in the literature [54,55].

The identification technique involves deriving a transmission function from the liquid under test. The transmission is defined by the ratio of the x-ray intensity transmitted through the liquid to the intensity of the unattenuated open beam. In practice this is carried out by taking an open beam (I_0) measurement closely followed by a measurement with the liquid under test in the beam path (I).

As the detector is an energy dispersive detector, the transmission is calculated as a function of energy. Transmission ratios at different energies can then be calculated in order to produce a signature, which is characteristic of the liquid in question. These intensity ratios can then be compared to a database in order to identify the liquid. The density and thickness of the liquid does not have an energy dependence and therefore cancels out of a transmission ratio leaving only the energy dependant mass attenuation term as shown below:

$$ln\left(\frac{I^{E1}}{I_0^{E1}}\right)\Bigg/ ln\left(\frac{I^{E2}}{I_0^{E2}}\right) = \alpha^{E1}/\alpha^{E2} \qquad \text{3-1}$$

where $E1$ and $E2$ superscripts refer to a ratio between two different energies. This intensity ratio technique is advantageous as thickness dependency is removed, meaning that the shape and width of the container in the beam path do

not affect the identification procedure (provided that the container is made from the same material as that in the database entry).

3.2.1 Database Matching

The database matching is carried out using a Z-test approach to compare the transmission spectra of the sample to a reference database entry. The Z-test hypothesis is used on the mean value of two normal distributions where the variances are known. The system does not work in strict accordance with the theory behind the test however it has proven to be a useful tool. In this treatment it is assumed that the two populations of interest, X_1 and X_2, are the detected counts in a specific energy bin for the test and reference object respectively.

It is assumed that X_1 has an unknown mean M_1 and a known variance σ_1^2, and that X_2 has an unknown mean M_2 and a known variance σ_2^2. It is also assumed that the populations satisfy the conditions of the Central Limit Theorem [56] and the integrated counts returned by the detector (I, or I_0) are used in place of the sample means $\overline{X_1}$ and $\overline{X_2}$.

The variance is calculated from the sample means by assuming Poisson statistics apply, so for example $\sigma_1 = \sqrt{\overline{X_1}}$. The test procedure is based on the distribution of the difference in the sample means. In general

$$\overline{X_1} - \overline{X_2} \sim N\left(M_1 - M_2, \frac{\sigma_1^2}{n_1} + \frac{\sigma_2^2}{n_2}\right)$$

3-2

Therefore, if the null hypothesis $H_0: M_1 = M_2$ is true, the test statistic

$$Z_0 = \frac{\overline{X_1} - \overline{X_2}}{\sqrt{\frac{\sigma_1^2}{n_1} + \frac{\sigma_2^2}{n_2}}}$$

3-3

follows the $N(0,1)$ distribution. By taking a single measurement each time (i.e. n=1) the test statistic reduces to:

$$Z_0 = \frac{\overline{X_1} - \overline{X_2}}{\sqrt{\sigma_1^2 + \sigma_2^2}}$$

3-4

where transmission values, $\overline{X_1}$ and $\overline{X_2}$ are defined by the I/I_0 values for the test object and database entry respectively. The variances are calculated via the propagation of errors formula:

$$\left(\frac{\sigma_T}{T}\right) = \left(\frac{\sigma_I}{I}\right)^2 + \left(\frac{\sigma_{I_0}}{I_0}\right)^2$$

3-5

where $T = I/I_0$ is defined as the transmission and σ_T is the error in transmission.

Since a strict interpretation of the theory is not followed, normal distribution tables are not used to reject the null hypothesis. Instead experimentally validated thresholds for Z_0 are chosen which incorporate additional error sources such as system drift, tool matching and other systematic errors. Better quality matches are characterised by the maximum number of bins with a Z_0 threshold close to zero.

This technique is very much focussed on the shape of the transmission curve produced by a given material. As many liquids contain similar mass fractions of common elements such as carbon, oxygen and hydrogen, one difficulty found in distinguishing between such liquids is the similarity in transmission curves produced. The implication of this is that the shape of the transmission curves and therefore the individual I and I_0 spectra must be as well resolved and as reproducible as possible. A further difficulty of this technique is the low interaction cross section of many liquids with x-rays which makes any change in mass fraction difficult to discriminate.

This leads to a requirement for a detector system which produces stable, reproducible spectra. In order to achieve sufficient discrimination between similar materials the Poisson errors, σ_1 and σ_2 in 3-4 must also be kept as low as possible. As the measurement time is limited by customer defined needs this results in a requirement for a detector capable of operating at high count rates. The detector and the pulse height analysis system must therefore be designed with careful consideration of high count rate, resulting in stable operation.

3.3 The Bottle Scanner System

Fig 3-1 shows a cross section of the Bottle Scanner system and the location of the detector and x-ray generator [57]. The bottle is placed in a cradle which is driven in the vertical axis to align the liquid inside the bottle with the x-ray beam. The x-ray beam is measured by the detector with the bottle in the beam path. The bottle is then moved out of the beam by the cradle and an open beam, I_0 measurement is taken. This process takes around 10 seconds with a pass or fail message returned to the user within 20 seconds.

Lid for loading bottles

Bottle carriage

Detector

X-ray generator
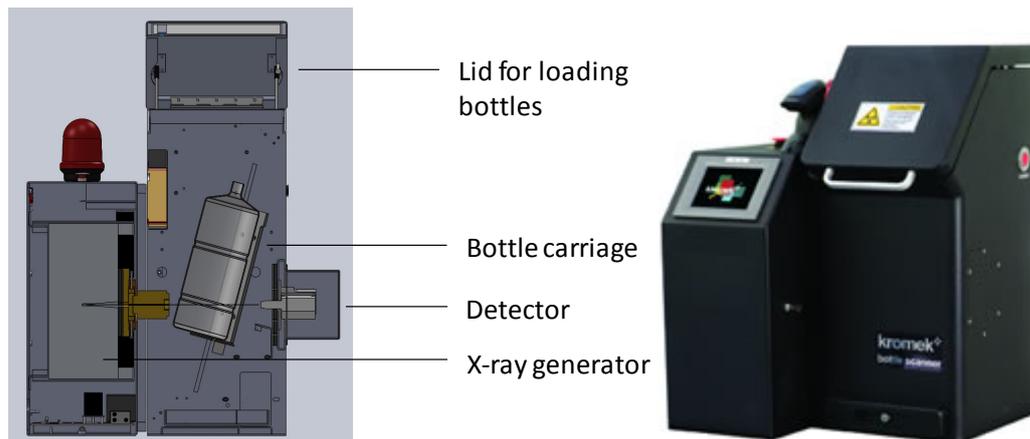
Fig 3-1 Cross sectional diagram of the Bottle Scanner system (left) and photograph of a Bottle Scanner system (right).

There are currently two types of scanner available. The first is the Verifier which is shown in Fig 3-1 and uses a barcode scanner to identify the bottle type and contents. The bottle is then scanned and the x-ray signature is compared to a database entry for the bottle. If the scanned bottle does not match the database entry the bottle is flagged up as a 'fail'. The second type of scanner is the Identifier which does not rely on a database entry for each bottle but instead uses

a more complex algorithm to classify bottles as threat or benign based on their x-ray signature. Both systems weigh around $240\,kg$ and are mounted onto a trolley for ease of transportation.

The detector selected for trials of the pulse height detection algorithm is a $5 \times 5 \times 1$ mm Amptek XR-100T CdTe detector. A bias voltage of $+600\,V$ is applied to the indium side of the Schottky detector[ii]. The detector is operated in reverse bias so that the leakage current is only a few nA resulting in low noise and low dark counts. The detector also includes an inbuilt preamplifier with an onboard Peltier cooler which cools the detector and the field effect transistor (FET) for low noise operation.

A power supply of $\pm 8\,V$ is used to power the preamplifier and an additional 0 to $4\,V$ supply is used to provide power to an onboard Peltier cooler. The gain of the unit is set to give $0.82\,mV/keV$ [58] and the detector is claimed to have a resolution of $< 1.5\,keV$ at $122\,keV$. However under the short shaping times used in this application such resolutions are not achievable.

Pulse shaping is carried out using a Cremat CR200-100ns shaping amplifier. The ideal response of the shaping amplifier is shown in Fig 3-2. Here the signal has been generated by connecting the output of a CR110 preamplifier to the input of the shaping amplifier.

[ii] Unless otherwise stated all measurements and simulations are carried out with a detector bias of $+600\,V$ applied to the indium side of the detector.

The x-ray generator is an XRB202 Spellman Monoblock™ which has a tube voltage range of 20 to 160 kV and a beam current range of 0.1 to 1.2 mA with a tungsten target. Both current and voltage accuracy are specified to be within $\pm 2\%$ of the programmed value.
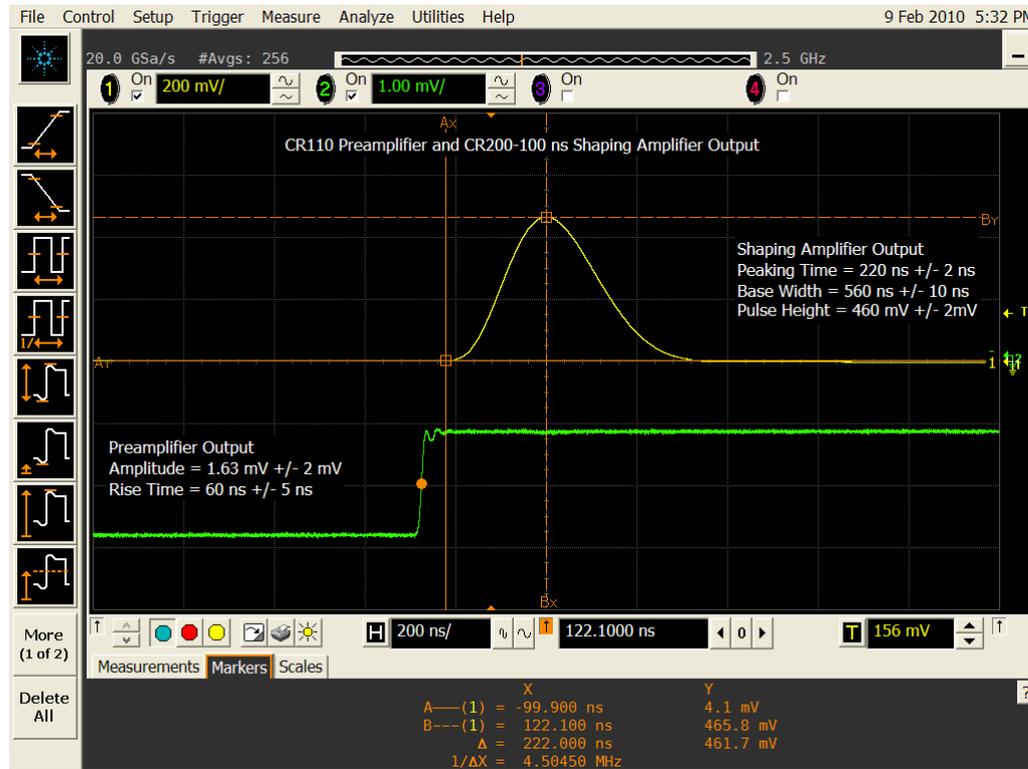
Fig 3-2 Shaping amplifier output generated from the output of a CR110 preamplifier.

The shaping amplifier output signal is defined by Equation 3-6. The constants were found empirically by fitting the shaping amplifier output to 2-19. The values $\tau = 34$ and $n = 6$ were found to produce the best fit giving:

$$V_{Out}(t) = \frac{V_p}{6!}(t/34)^6 . exp(-t/34)$$

3-6

Equation 3-6 will be used in Chapter 4 in order to simulate the shaping amplifier output.

3.4   Multi Channel Analyser

The x-ray spectrum is produced using an FPGA programmed to perform the function of a MCA. This was specifically designed for this application and is comprised of a buffered input with a 200 MHz, 8 bit analogue to digital (A to D) converter. The 8 bit digital information is then processed by an Altera cyclone II FPGA and stored in the embedded memory. The data is then read out by a PC every 16 ms via RS232. This data stream consists of a 1x32 array of counts where each element in the array represents a single energy bin and contains the total recorded counts in 16 ms.

The incoming pulse is expected to have a peak amplitude ranging from 0 to 1 V. In this application 1 V is defined as corresponding to a pulse generated by a 160 keV photon. This was done by dual source calibration of the gain setting on the shaping amplifier using the 122.1 keV and 59.5 keV lines from ^{57}Co and ^{241}Am sources respectively [59].

The A to D converter is limited to an 8 bit resolution, dividing the input voltage into 256 levels. Each level corresponds to an energy of 0.625 keV. The peak voltage values are sorted into 32 bins where each bin represents 8 least significant bits (LSB) or an energy range of 5 keV.

For the outlined detector system the shaped output is typical of that shown in Fig 3-3, noise appears predominantly below $60 \, mV$, corresponding to an energy of less than $10 \, keV$.
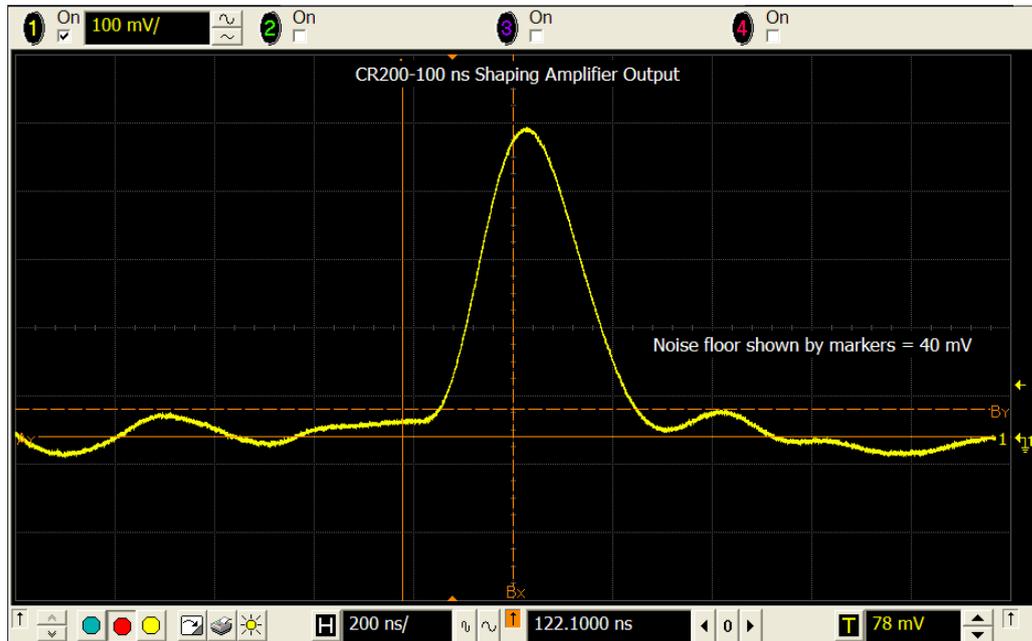
Fig 3-3 Shaped output signal from a CR-200-100ns shaping amplifier. As can be seen the noise appears below $60 \, mV$.

Dividing this voltage range into 32 equally spaced energy bins it is clear that counts appearing in bin 1 and bin 2 of the MCA are predominantly noise, consequently a low level discriminator (LLD) is implemented at approximately $63 \, mV$ (7 LSBs) in all of the algorithms discussed in this work. Signals below this level are regarded as noise and are not added to the spectrum therefore no counts are returned into bin 1 and only a small proportion of bin 2 is sensitive to counts.

3.5 Initial Detector System Tests

Initial system tests were carried out by connecting the detector and CR-200-100ns shaping amplifier to a commercially available 8192 channel Canberra Multiport II MCA. The voltage input range of this MCA is $10\,V$ which corresponds to $1.22\,mV$ per channel. A schematic diagram of the experimental set up is shown in Fig 3-4.
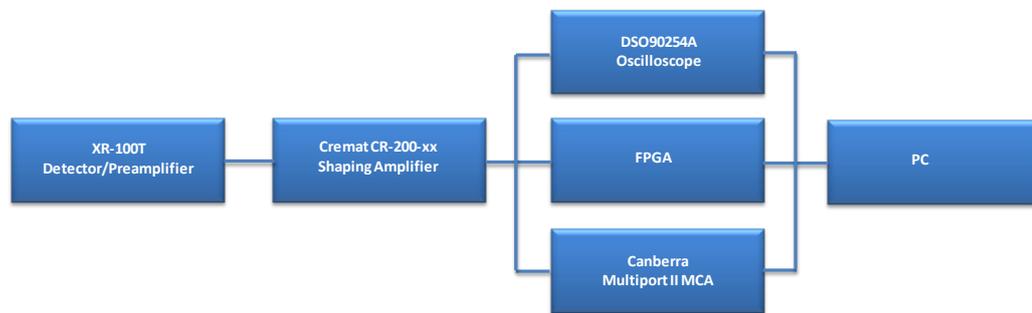
Fig 3-4 Schematic diagram showing the experimental setup of the XR-100T detector, FPGA and shaping amplifier.

Fig 3-5 shows a pulse height spectrum from a low activity ^{57}Co source acquired using a Canberra Multiport II MCA and a CR-200-100ns shaping amplifier.
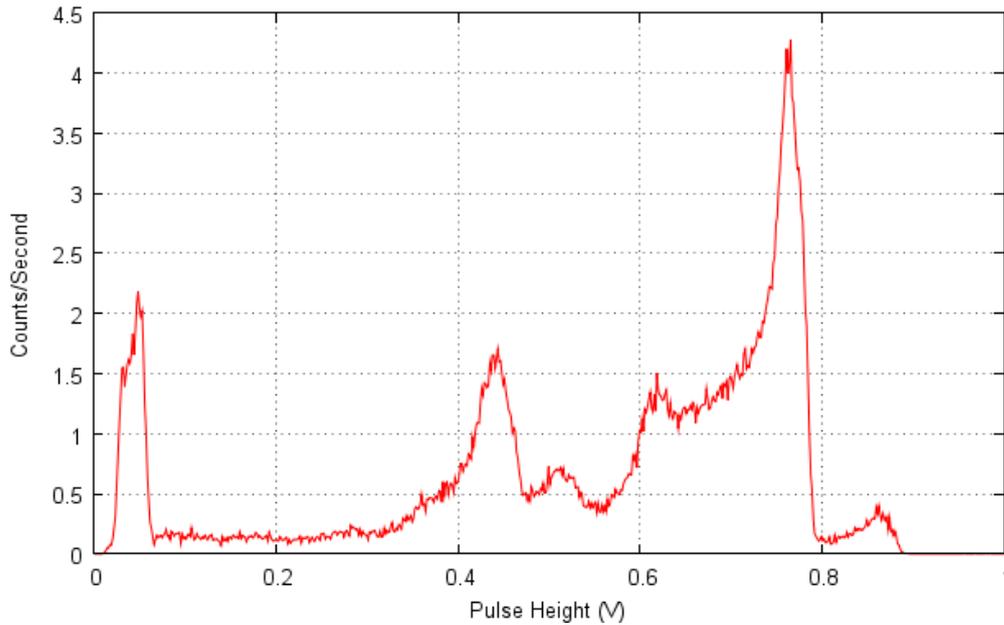
Fig 3-5 ^{57}Co spectrum acquired from the Amptek XR-100T detector using a CR-200-100ns shaping amplifier and a Canberra Multiport II MCA. The acquisition time was 300 seconds.

The full width half maximum (FWHM) was measured to be $2.7\ keV\ \pm 0.3\ keV$.

This spectrum provides a baseline of the system performance and pulse height

detection algorithms developed in the following chapters are compared to this.

3.5.1 High Count Rate Test

Fig 3-6 shows an oscilloscope trace from the outputs of the XR-100T detector

and shaping amplifier. Here the detector was irradiated with x-rays from a

tungsten tube with a beam current of $0.143\ mA$ and a tube voltage of $160\ kV$. At

very high count rates pulses become piled up, potentially resulting in a lowering

of the observed count rate. In addition to this the statistical behaviour of accepted

counts is also modified [60] meaning that correction is required in order to reinstate

Poisson type uncertainty.
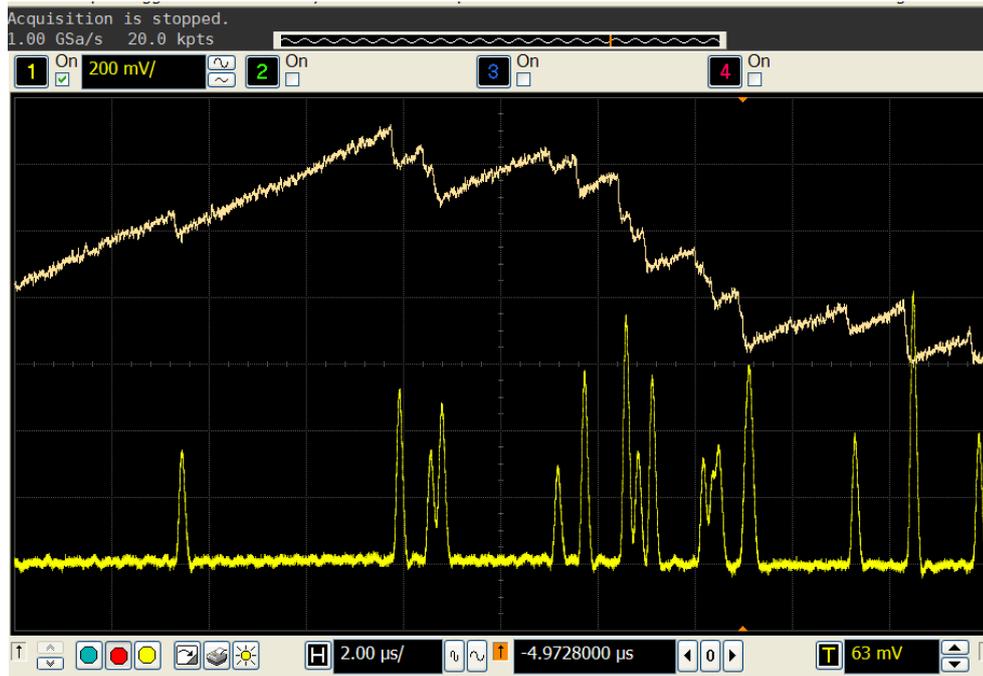
Fig 3-6 Preamplifier and shaping amplifier oscilloscope traces from an XR-100T detector under x-ray illumination from a tungsten tube with a beam current of 0.143 mA.

Pile up in the counting system is clearly undesirable leading to distortion of the Poisson process resulting in a new type of distribution, the characteristics of which depend on the specific type of count loss [61],[62]. Measurements under a fixed real count time as required in the Bottle Scanner application are reported to suffer increased uncertainty when count losses exceed 20% of the total count [49]. The additional consideration in the Bottle Scanner application comes from the fact that the detection algorithm is energy sensitive, therefore unlike a simple counting system, in addition to counting losses, pulse pile up has the affect of distorting the energy of the piled up pulses.

3.6 Conclusion

In this chapter an overview of the underlying theory behind the operation of the Bottle Scanner was given. This work is not intended to focus on the area of materials identification, however, an understanding of the requirements of the application enables a greater appreciation of the design requirements of a detector system.

The transmission for a given bottle is calculated by the ratio of the measured open beam and transmitted beam through the bottle. This measurement removes the sample thickness dependency resulting in a spectral shape which is a function of the mass fraction of each element present in the sample plus any convoluted measurement artefacts. The transmission spectrum is then compared to a database entry by a Z-test approach in order to identify the threat status of the liquid.

As discussed the materials identification is highly sensitive to the shape of the transmission spectrum therefore the individual I and I_0 spectra must be as well resolved and as reproducible as possible. In addition the customer requirement for a scan time of no greater than 20 seconds requires a detector system capable of high count rate operation presenting specific challenges for the detector electronics.

The Bottle Scanner system was also outlined along with the selection of detector electronics. The XR-100T detector is used for this work along with a Cremat CR-100T shaping amplifier. A function was fitted to the shaping amplifier output which will be used in the simulations discussed in the following chapter. Also shown was the output of the shaping amplifier for a single detected event. This exhibits a noise floor of around $60\ mV$.

An initial test of the system using a low activity ^{57}Co source was also shown, with the output measured using a commercially available Canberra Multiport II MCA. This provides a baseline for the system performance and the pulse height detection algorithms developed in the following chapters will be compared against this spectrum. Also shown was an oscilloscope trace of multiple events taken at a high count rate under x-ray irradiation. This illustrates the effect of pulse pile up with the random arrival of many pulses at the detector which become convolved together.

The following chapter is devoted to the design and test of pulse height detection algorithms in order to measure the I and I_0 spectra from the detector. The performance of these algorithms at high count rates is simulated using a Monte Carlo approach which simulates the random arrival of the x-rays at the detector.

Chapter 4   Pulse Height Analysis Techniques for Liquid Threat Detection

4.1   Introduction

The customer requirement of a maximum measurement time of 20 seconds per bottle presents the need for a pulse height analysis algorithm which is able to perform well at high count rates. A major problem encountered in high count rate systems is pulse pile up. This distorts the measurement of both energy and counts which, as previously discussed are both critical parameters in threat identification.

The problem of pulse pile up originates from the fact that radiation emitted from an x-ray tube is a random Poisson process resulting in random time intervals between events. Random deviations from the mean count rate can result in pulses piling up. Such behaviour can only be simulated by a Monte Carlo type approach.

A Monte Carlo simulation was carried out to model the random arrival rate of radiation at the detector and is discussed in Sections 4.2 and 4.3. Three pulse

height detection algorithms are then outlined in Section 4.4. These algorithms have varying levels of sophistication in dealing with pulse pile up.

These algorithms are then simulated in Section 4.5 and the effects of counting losses and energy distortion is reported. A quantitative measure of both the counting loss and a parameter defined here as the *spectral distortion* is given for each algorithm as a function of input count rate. The spectral distortion gives a measure of the degree of deviation of the output spectrum from that of the input spectrum and provides a useful metric for comparison between algorithms.

4.2   Simulation of the Random Time of Arrival of X-rays

In this section a Monte Carlo simulation which was written in order to simulate the random arrival of x-rays at the detector is discussed. The aim of this modelling is to enable the performance of various pulse height detection algorithms to be tested by simulation of pulse pile up. In general if the pulse height detection algorithm is known, counting losses for a given input count rate can be estimated by applying Equations 2-25 or 2-26. In reality most MCA systems are not accurately described by either of these equations and typically operate somewhere in between. In addition to this, Equations 2-25 and 2-26 give no indication of the energy distortion resulting from pulse pile up.

A further subtlety comes from the variability of the shaping amplifier base width as a function of height. This results in high energy events having a larger probability of pulse pile up than low energy events on an event by event basis. This leads to a pile up probability which is biased towards high energy which is not considered in Equation 2-25 or 2-26.

The Monte Carlo simulation described in this section is based on an input spectrum which is defined from an x-ray tube model [63] of the spectral output from the x-ray generator used in the Bottle Scanner. The input spectrum can be considered as the expected result in long run for a perfect detector and pulse height detection system. A random time series of events (RTSE) is then

generated by simulating the random time interval distribution of the emission of radiation from the x-ray tube.

As the RTSE is generated from the probability distribution of the input spectrum both the RTSE and input spectrum should be in agreement to within the Poisson error. The output spectrum is then simulated by applying point spread functions to each event in the RTSE in order to simulate the behaviour of the read out electronics. The pulse height detection algorithms are then applied to the simulated shaping amplifier output to generate an output spectrum.

As the RTSE and the output spectrum are known this gives a unique opportunity to quantitatively analyse the efficiency and precision of various pulse height detection algorithms. Such an approach exploits the so called 'Monte Carlo truth'. This type of analysis is impossible to perform empirically as the RTSE can never be absolutely known. In addition to this, variations in x-ray generator output, detector alignment and detector variability may lead to undesirable measurement artefacts if attempted experimentally.

4.2.1 Random Time Distribution and Energy Distribution of Radiation Incident on a Detector

As the emission of an x-ray from an x-ray tube occurs randomly in time the total number of x-rays produced over a given time interval represents an average value with a related uncertainty. If we treat these events as identical point processes [64] and temporarily ignore the variance in energy of each photon, the arrival time of each event can first be understood.

In order to specify the point in time at which an event occurs the timescale over which a measurement takes place is divided into N elements of length, δt. The size of the element δt is governed by the accuracy to which the time of an event must be specified. The consequence of specifying a small time element is that the probability of an event occurring within any given time element is very small. If the time at which a single event occurs is completely unaffected by neighbouring events then the process is described by Poisson statistics and the probability of observing r events in a time interval t_0 is expected to conform closely to the Poisson distribution:

$$p_r = \frac{\mu^r e^{-\mu}}{r!}$$

4-1

Where μ is the expected number of events defined as the probability, p, of an event occurring within a given time element multiplied by the number of elements, N in the time interval t_0:

$$\mu = pN = p\frac{t_0}{\delta t}$$

4-2

The average arrival rate at the detector i.e. the average number of events per second can be defined in terms of Equation 4-3 as:

$$\langle R \rangle = \frac{pN}{t_0} = \frac{\mu}{t_0} = \frac{p}{\delta t}$$

4-3

The interval distribution between events describes the probability that the time interval between two successive events is of a certain length. The probability that an event will occur within the next time element from a previous event is given by p. This is because the probability of a subsequent event occurring is not affected by the occurrence of the first event. Therefore the probability of an event occurring in any given time window is constant.

The probability of an interval of $2\delta t$ between events on the other hand requires both that an event must be observed at $2\delta t$ after the first event and that there must not be an event at time δt after the first event. This can be written as:

$$p_{2\delta t} = (1 - p)p$$

4-4

This argument can be extended to the more general case where the probability of duration $n\delta t$ between events is given by:

$$p_n = (1 - p)^n p$$

4-5

Where p_n is referred to here as the *time interval probability*.

The occurrence of an event in a Poisson process gives no indication of when the next event may occur therefore simulation of such processes requires the use of a Monte Carlo approach.

The dead time associated with each individual random even can overlap with one or more preceding or following pulses, this pulse pile up leads to a convoluted signal making pulse height analysis difficult. This results in a maximum input count rate which is significantly less than the dead time for a single pulse divided by the total acquisition time i.e. pulses in a continuous evenly spaced chain.

If a dead time of $560\ ns$ is assumed for each pulse by reference to the base width of the shaping amplifier output in Fig 3-2 then in order to avoid pulses piling up the interval following each event must be greater than $560\ ns$. The probability of observing an interval greater than t_w is given by [21]:

$$p(t_w) = exp(-Rt_w) \qquad \text{4-6}$$

Where R is the input count rate.

The energy of a given photon is also random with the distribution given by the emission spectrum of the source in question. This could result in discrete energies in the case of a radioactive isotope or in the case of this application a bremsstrahlung continuum of energies from an x-ray tube.

4.2.2 Modelling of the Arrival of Randomly Time Spaced Radiation at a Detector

The energy and time of arrival of radiation at a detector was modelled using a Monte Carlo simulation written in Matlab. As described in Chapter 3, the application for the detector system requires a 32 bin MCA where the energy range 0 to 160 keV is represented by 32 voltage levels each of 31.25 mV ranging from 0 to 1 V.

For illustration purposes, three discrete energy levels have been chosen which span the energy range in question. These are 40 keV, 80 keV and 120 keV and on a 1 to 32 bin scale relate to bins 8, 16 and 24 respectively. Results from the model will later be shown using the bremsstrahlung spectrum predicted by the tube model.

A reduced simulation time of 1 ms has been carried out in order to illustrate the basic operation of the random event generation. If it is assumed that on average the beam of x-rays is evenly composed of 33 events from each of the three incident energies (33,000 counts per second per energy), repeat measurements would yield a mean deviation of $\sqrt{33}$ from the expected count for each of the three energies. In long run i.e for large n, the percentage variance tends to zero and the measured number of counts converges to the expected number of counts.

Fig 4-1 shows the time space probability as a function of time interval $n\delta t$ between events as defined by 4-5. Also shown is the cumulative probability defined by 4-7. Here the cumulative probability gives the probability of an event occurring between time $t = 0$ to $t = n\delta t$ from a previous event.

$$P(n) = \sum_{n=1}^{N} p_n = \sum_{n=1}^{N} \left(1 - \frac{\mu}{N}\right)^{\mu/n} \qquad \text{4-7}$$
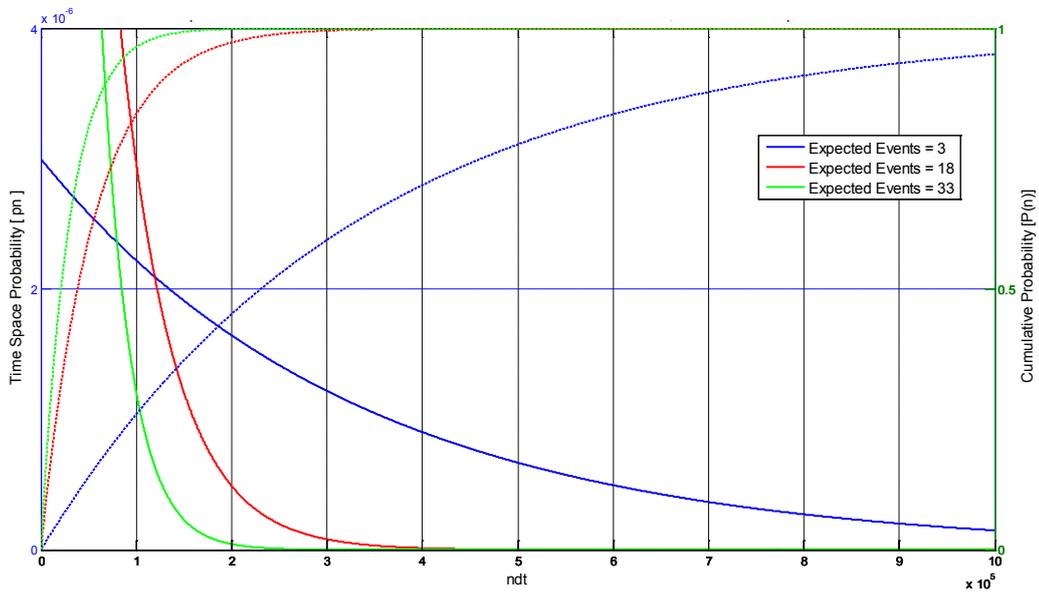
Fig 4-1 Time interval (solid line) and cumulative (dashed line) probabilities as a function of time interval, $n\delta t$. Here the expected total count is 99 in a total time, $N\delta t = 1\ ms$ where $N = 1 \times 10^6$ and $\delta t = 1\ ns$.

As can be seen from Fig 4-1 the time space probability asymptotes to zero with $n\delta t$. The rate of change of the curve is defined by the input count rate and shows that for high event rates the probability of a short interval between events is large and the probability of a long time interval is very small.

4.2.3   The Input Spectrum

In order to enable accurate comparisons to be made between the three pulse height detection algorithms it is important to maintain both small and consistent Poisson errors at each input count rate. The modelling is carried out by varying the total simulation time over which one million RTSE are emitted and detected. This approach means that the count rate can be varied whilst maintaining a constant total count and therefore total Poisson error across the spectrum.

The data file of one million RTSE is generated offline from the main program and is used as the input file for all simulations. Aside from reducing computational time this also ensures that each simulation is carried out using the same set of RTSE meaning that changes in the output spectrum are due to the variation in performance of the pulse height detection algorithms only.

As shown in Fig 4-2 the spectrum from the tube model is re binned into 32 bins and a region of interest (ROI) is defined from 30 to 125 keV (bins 6 to 25). The total counts in the spectrum are adjusted such that the sum of counts in the ROI is equal to one million, as can be seen in Fig 4-3 this gives a maximum Poisson error of $< 1\%$ for each bin in the ROI.
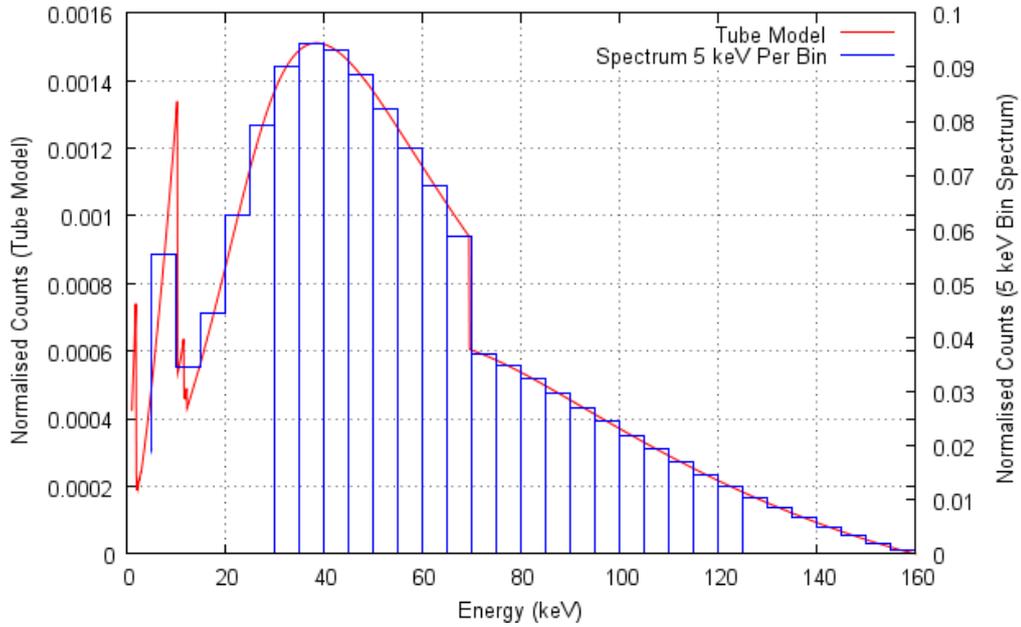
Fig 4-2 Input spectrum from the Tube Model re binned into 32 energy levels. The region of interest (ROI) shows the area covered by the simulation which has a total count of 1 million.
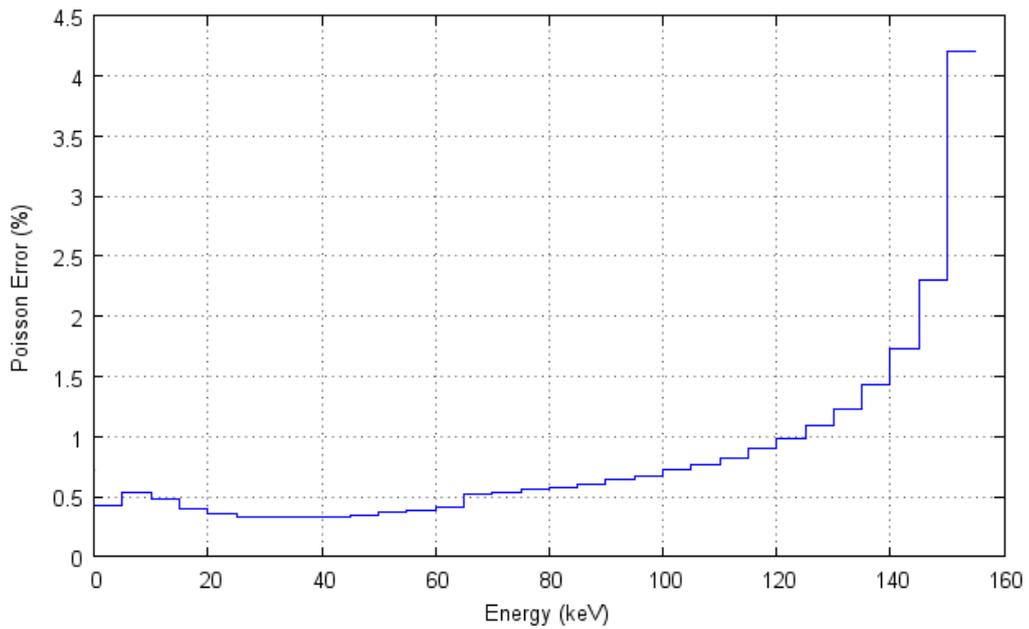
Fig 4-3 Poisson error per bin from the spectrum shown in Fig 4-2.

The simulation of pulse height detection algorithms that follow will span the ROI only and energies outside this range will not be considered. The selection of this

73

small region of interest is beneficial as the total counts required to achieve a Poisson error of less than 1% across the entire spectrum is reduced.

In addition to this, the total number of segments, N required to accurately calculate both p_n and $P(n)$ in Equations 4-5 and 4-7 respectively is dependent on the expected count rate, μ and the width of the time interval, δt. The number of segments is therefore selected with reference to the expected count rate from the input spectrum.

As can be seen from Fig 4-1 high input count rates result in a time interval probability curve which rapidly tends to zero. This is because under this condition the probability of a small time space between events is high and the probability of a large time space is vanishingly small. A selection of $n\delta t$ which is not suitably narrow enough to numerically integrate the rapidly falling probability curve would therefore result in an asymptote of less than unity. This can be solved by reducing $n\delta t$ accordingly, however this then leads to problems with low rate events as seen in bin 32 of Fig 4-2 requiring very large values of N.

The cumulative probability of low rate events have a very slow asymptote to unity meaning that large values of $n\delta t$ are required. Clearly a cumulative probability of $P(n) = 1$ is not achievable as the asymptote is infinite. In this model a value of N is selected such that $P(n) = 0.999$ at $t = N\delta t$. An event which occurs outside the time which is spanned by the cumulative probability

$(P(n) = 0$ to $P(n) = 0.999)$ is placed at $t = N\delta t$. This results in an average error in the placement of 1 in 1000 events which represents a negligible contribution to the overall spectrum.

The selection of the 30 to 125 keV energy range ensures that each value of μ is sufficiently high in order to allow a workable value of N. In the case of this simulation a value of $N = 1 \times 10^{12}$ was selected. This is sufficiently large to ensure that all values p_n and $P(n)$ asymptote to 0.999.

4.2.4 Simulation of Random Time of Arrival and Energy

The time of arrival of an event of energy, E, is simulated by use of a 0 to 1 random number generator with the probability distribution is weighted by Equation 4-7. Here the expected counts, μ is defined by the number of counts in the input spectrum of energy, E.

The input spectrum is returned by Monte Carlo simulation of the tube model [65] as described in Fig 4-2. Whilst the tube model represents the expected long run distribution of x-rays emitted by the x-ray tube, the input spectrum represents the actual events observed in a single acquisition of one million events.

The count rate is defined by variation of the time represented by each segment. The time spacing of each segment is calculated by:

$$\delta t = \frac{R}{1 \times 10^6. N} \qquad \text{4-8}$$

Where R is the mean count rate defined in the model.

As previously mentioned this approach is advantageous as it enables accurate comparisons to be made between algorithms without concern for variance in the input RTSE.

Fig 4-4 shows a simulation of the random arrival rate of radiation for a simulation time of $1\ ms$ from the input spectrum outlined above. As can be seen the events are distributed randomly in both energy and time spacing. The graph shows regions of large deviations from the expected count rate. This further illustrates the need for a rigorous analysis of the behaviour of the full signal chain in order to ensure that the system is able to satisfactorily perform under real conditions.
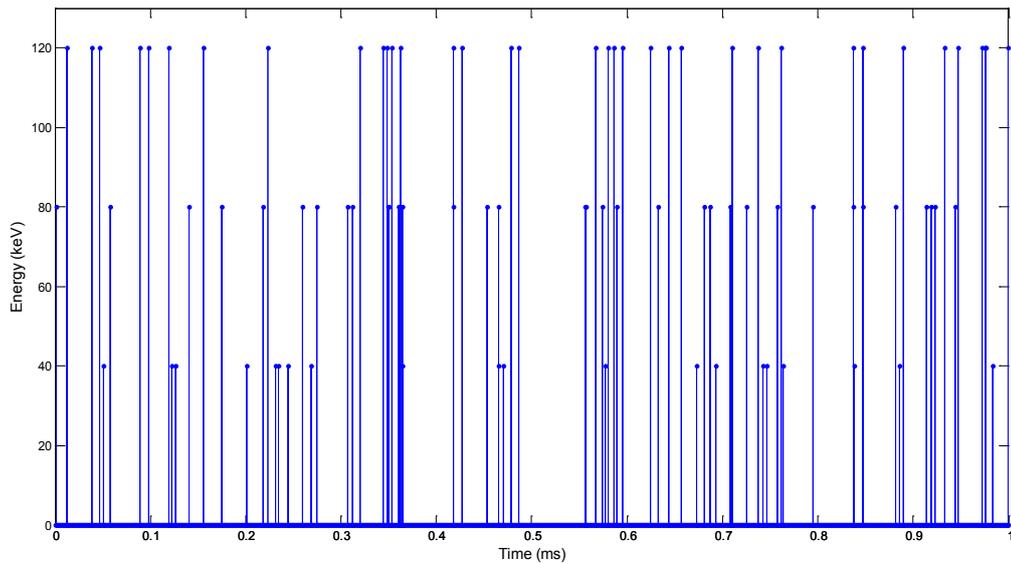
Fig 4-4 Simulation of the random arrival of events at a detector over $1\ ms$. Here the expected count rate for each of the three energies is 33,000 counts per second.

In Section 4.7 the simulation will be extended to the entire one million events and the input spectrum will be expanded to that described in Fig 4-2.

4.3 Modelling of the Response of the Detector Electronics to Randomly Time Spaced Radiation

In the previous section the model was developed in order to simulate the random nature of the time spacing between successive photons arriving at the detector. The arrival of photons in this context is a point process with no significant time component.

In this section the response of the detector electronics to the arrival of varying energy and time spaced radiation will be modelled. Unlike incident radiation, the

response of the preamplifier and shaping amplifier are not point processes and have response times which in some cases will exceed the time spacing between successive photons. Here the point the spread function defined by Equation 3-6 is used to model the output signal from the shaping amplifier. This will form the basis for a discussion of various pulse height detection algorithms which can be implemented on an FPGA.

The focus of this simulation is mainly directed at pulse pile up in the shaping amplifier stage and the development of pulse height detection algorithms which are able to deal with this. For this reason it is assumed at this stage that the rise time of the preamplifier is instantaneous.

Fig 4-5 and Fig 4-6 show the preamplifier and shaping amplifier response respectively as a function of time. The random series of events has also been added to Fig 4-5 in order to illustrate the effect on the preamplifier signal. As can be seen the offset of the preamplifier signal increases with the rate of incident radiation. A sustained high input count rate would result in the preamplifier output reaching saturation.
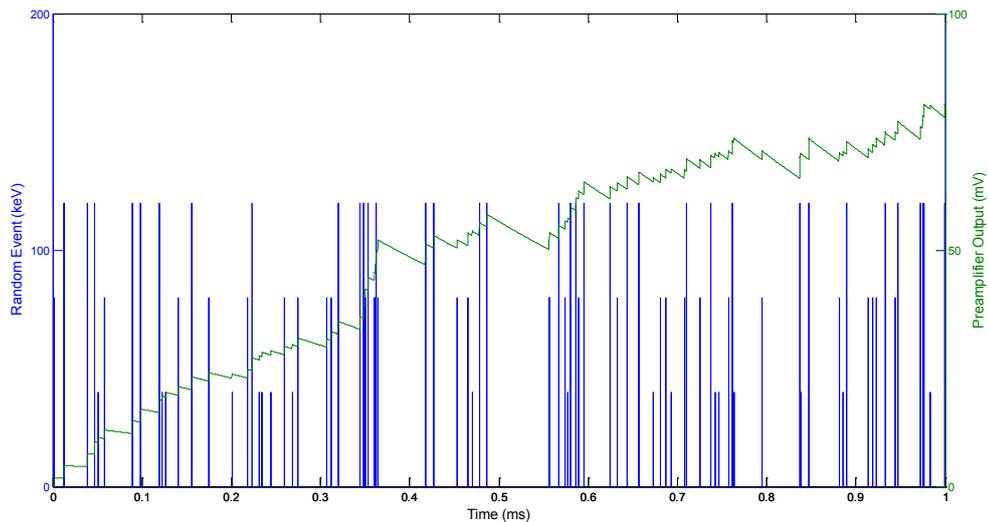
Fig 4-5 Graph showing the randomly time spaced events from Fig 4-4 with the modelled preamplifier response overlaid.

The saturation level for the XR-100T preamplifier is $\pm 8\,V$. For the purposes of this simulation any rise in the preamplifier offset above the saturation level will be ignored. No restriction has been added in order to prevent an offset of $> 8\,V$. Although this does not accurately represent the true system behaviour this can be avoided by optimisation of R_f and C_f which is more easily performed empirically.
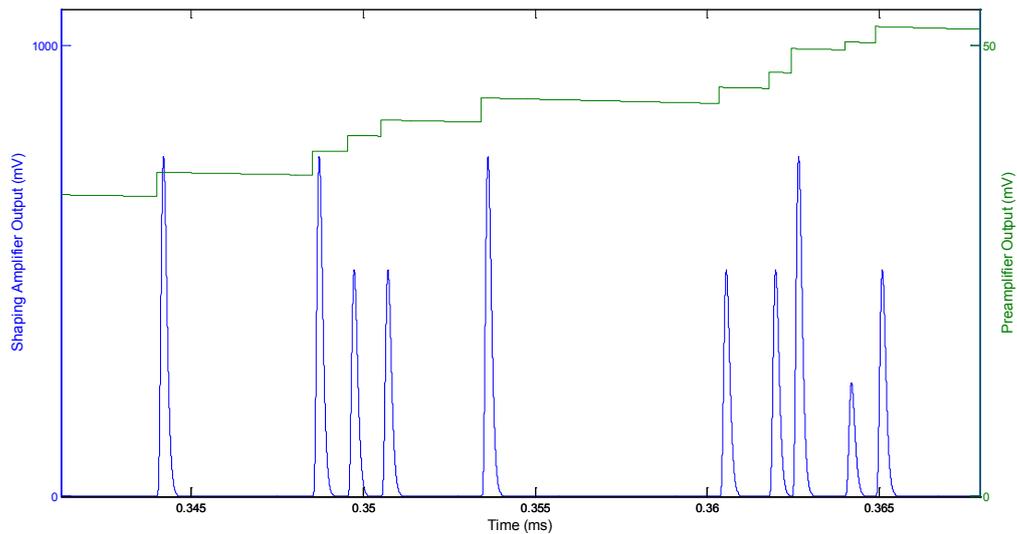
Fig 4-6 Simulation of the shaping amplifier response to the random events shown in Fig 4-5. Here only a small portion of the 1 ms simulation is shown for clarity.

The shaping amplifier signals in Fig 4-6 are clearly resolved due to the low input count rate. Fig 4-7 shows an example of two piled up events where the time spacing between incident radiation is less than the width of the shaped pulse. All events shown are of the same energy but as can be seen the height of the final pulse is modified due to pile up with the preceding pulse.
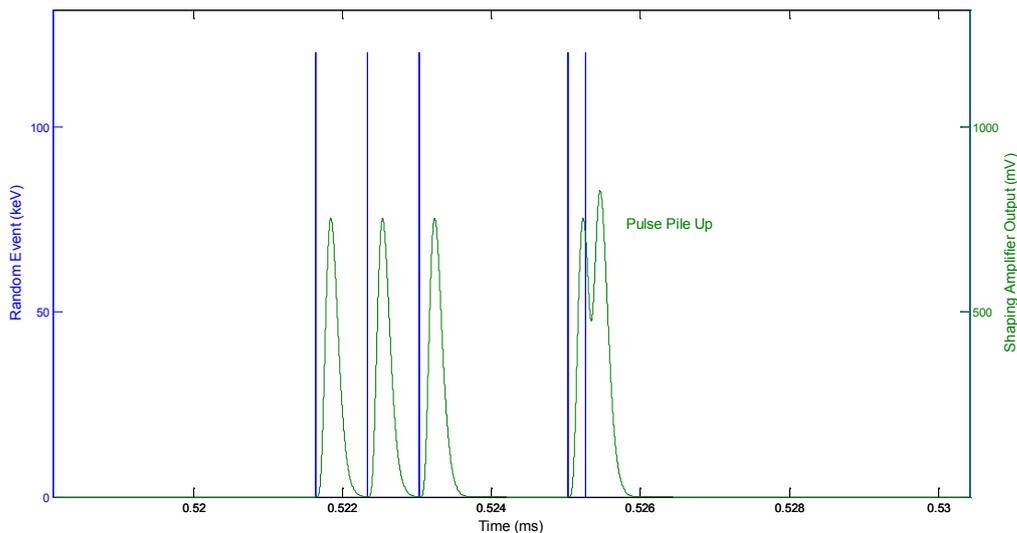
Fig 4-7 Illustration of two piled up events. The time interval between two successive 120 keV events is less than the width of the shaped pulse. This has the effect of distorting the height of the second piled up pulse.

In the next section the development of pulse height detection algorithms will be described with reference to the shaping amplifier pulse shape outlined above.

4.4 Pulse Height Detection Algorithms

Three algorithms have been developed to analyse the simulated output from the shaping amplifier. In this section these algorithms will be modelled and simulated at various input count rates. The algorithms have been designed to be implemented on an FPGA[iii]. This limits the complexity of the algorithms which can be implemented and Algorithms 1 to 3 outlined below were all developed with these restrictions in mind.

Two parameters are reported for each of the algorithms in these simulations. Firstly the counting loss which is simply the difference between the total counts in each of the output spectra and the input RTSE. Secondly a spectral distortion is calculated where the spectral distortion is defined as the sum of the absolute difference between the input, C_j, and output, c_j, spectra across all bins normalised to the input count in each energy bin, given by:

$$D = \sum_{j=1}^{32} \frac{|c_j - C_j|}{C_j}$$

4-9

Here D is the spectral deviation and C_j and c_j are the counts in the input and output spectrum respectively. The use of normalisation to the input count in each

---

iii The FPGA and associated electronics were designed and built by dBTechnologies[66]   .

bin is useful as it gives an accurate measure of the degree to which the shape of the spectrum has changed and decouples any effects from straightforward counting losses.. If the input and output counts are equal $D = 0$ and the input and output spectrum are in agreement. A negative value of D indicates a loss in counts and a positive value of D indicates an excess of counts, taking the sum of the absolute values of D across all bins give the spectral distortion. This approach is used in the Fig 4-12, Fig 4-14 and Fig 4-16 in the following section.

As both the counts and spectral shape are important in this application an ideal pulse height detection algorithm would minimise both counting losses and energy distortion. Clearly these two factors will be affected by the input count rate and therefore a balance must be struck between minimising Poisson errors through high count rate operation and minimising counting losses and energy distortion.

The operation of Algorithm 1 is described in detail in the flow chart in Fig 4-8. As Algorithms 2 and 3 employ the same peak detect procedure only a description of the differing pulse pile up handling is given.
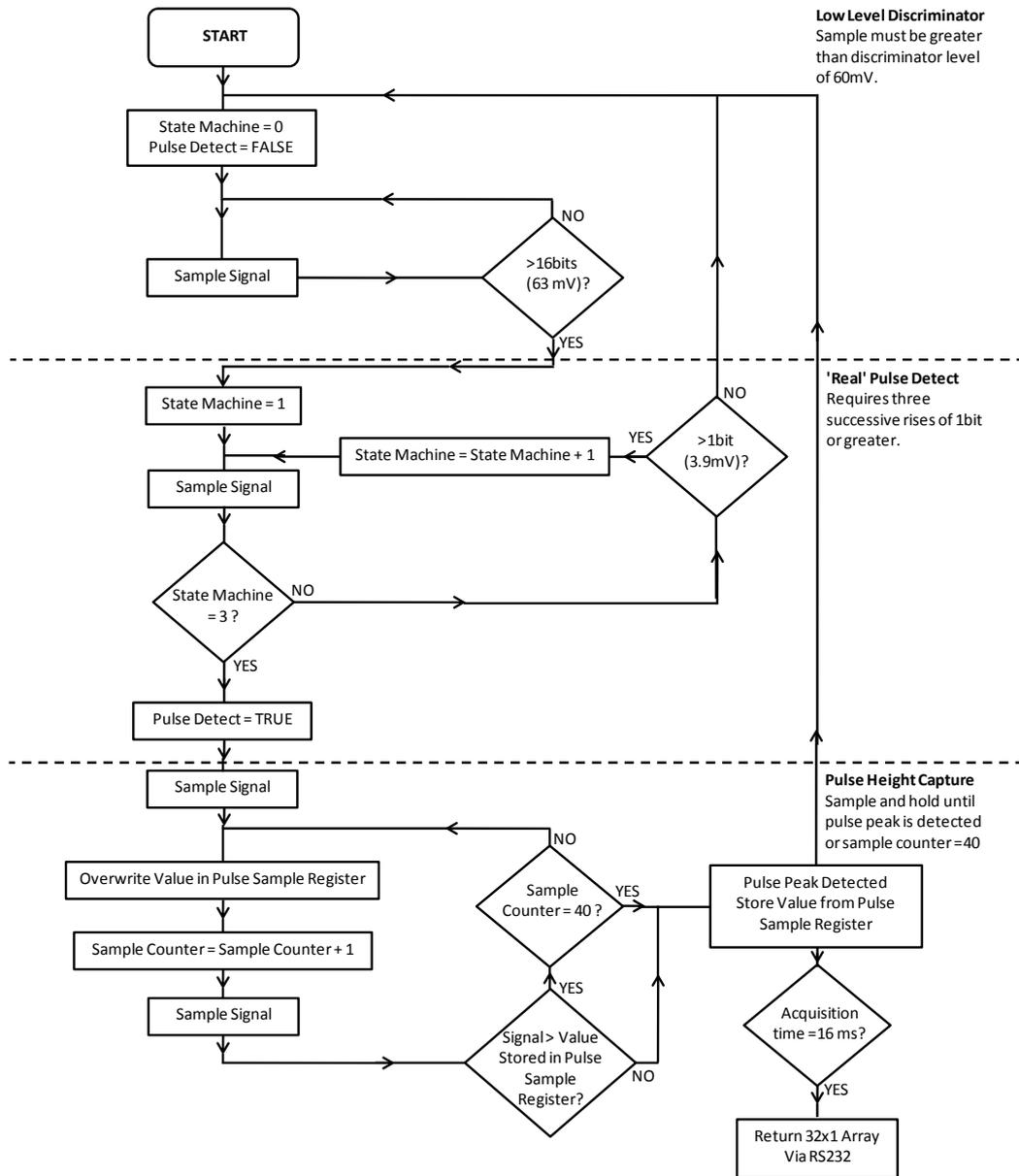
Fig 4-8 Flow chart describing the operation of pulse height detection Algorithm 1.

Fig 4-9 shows an illustration of the operation of the three algorithms on a series of shaping amplifier pulses. The green squares on top of the pulses denote when each of the algorithms has registered a count.
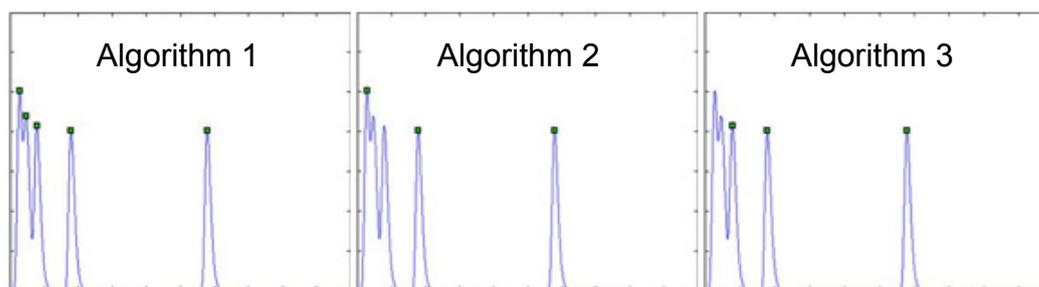
Fig 4-9 Illustration of the operation of three pulse height analysis algorithms on a series of pulses representative of those from a shaping amplifier.

The key features of the three algorithms are as follows:

Algorithm 1. *Sample and hold highest value* – the pulse detection 'arms' once the signal goes above a threshold value of $63\ mV$. The pulse is then regarded as 'real' if three successive rises of $3.9\ mV$ (1 LSB) or greater are observed. The algorithm then continues to sample and hold the highest value for 40 further samples. As shown in Fig 4-9 the algorithm records all five counts regardless of the distortion in pulse height due to the pile up of events 2 and 3 with event 1.

As can be seen from Fig 4-8 the maximum value is stored by a series of 40 sample and hold steps. The total number of samples above the $63\ mV$ threshold is 43 samples which is equivalent to $210\ ns$. The time from $63\ mV$ to the peak is approximately $165\ ns$ meaning that the sampling continues beyond the peak maxima.

The disadvantage of Algorithm 1 is that if the pulse has not peaked within the sampling time due to pulse pile up for example, the value of the 40th sample and

hold beyond the pulse detect stage is incorrectly recorded and wrongly assigned to the corresponding energy bin. Additional pulses which are piled up with the first pulse will re arm the pulse detect and be included in the final output spectrum.

Algorithm 2. *Sample and hold with return below threshold condition* – samples and holds the highest value of a pulse as in Algorithm 1 but waits for the sampled pulse to return below the 63 mV threshold before arming for the next pulse. Here the algorithm does not record counts 2 and 3 in Fig 4-9 because the shaping amplifier output has not dropped below the threshold level before a new pulse is observed.

Algorithm 3. *Pile up rejection with add back of deleted counts* – measures the number of samples between two successive peaks and discards events which are too closely spaced. As illustrated in Fig 4-10 (right) if the time spacing, S is less than 600 ns the second peak becomes distorted by the tail of the first peak and is therefore discarded. As the peak spacing is further reduced to 200 ns, the rising edge of the second peak begins to affect the height of the first peak. This is illustrated in Fig 4-10 (left) and in this case both peaks are discarded.
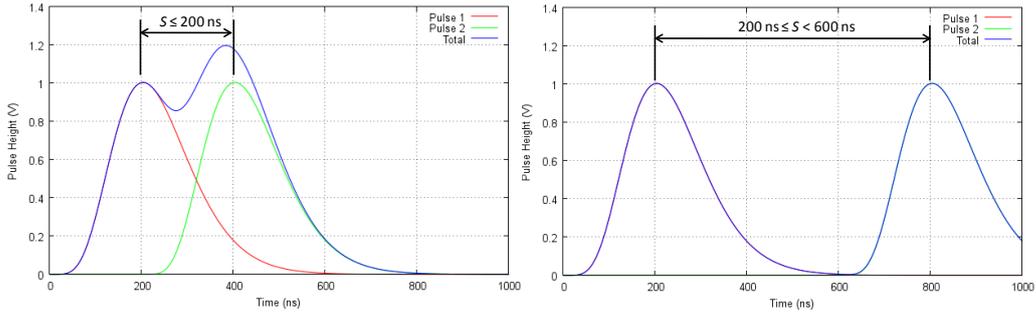
Fig 4-10 Illustration of Algorithm 3 showing the conditions for discarding pulses. Here if pulse separations, $S \leq 200\ ns$ both pulses are discarded, if $200\ ns\ \leq S <\ 600\ ns$ (right) only pulse 2 is discarded.

A registry of discarded pulses is kept and these are added back into the spectrum in a ratio defined by the counts in the collected spectrum. As shown in Fig 4-9 this algorithm does not record counts 1 and 2 because the peak spacings are less than the defined time interval. Counts 1 and 2 are then recorded in a discard registry to later be added back into the spectrum as follows:

$$Count(bin) + Count(bin). \left[Discard\ Count / \sum_{bin=1}^{32} Count(bin) \right] \qquad 4\text{-}10$$

This method should theoretically give correctly binned pulses irrespective of the percentage of discarded counts. The accuracy of redistribution of counts is however limited to the Poisson error associated with each bin. Bins with low counts will have large percentage errors making redistribution of counts into these bins erroneous.

The other limitation which is common to all three algorithms is in treating very closely piled up pulses. If the peaks have a separation of less than a $15\ ns$ the

sampling rate of the A to D is not sufficiently fast to detect the presence of two peaks. Equally the A to D converter has a maximum resolution of 8 bits across a voltage range of $1\,V$ meaning that changes of less than $3.9\,mV$ (1 LSB) are not resolvable.

Piled up pulses with a total height $> 1\,V$ are placed in bin 32 and for this reason these counts are generally discarded in analysis due to the low intensity of $160\,keV$ photons and the proportionally higher probability of the presence of piled up pulses.

4.5   Simulation of the Response of Pulse Height Detection Algorithms

In this section the results from simulation of the response of the three pulse height detection algorithms is shown using the model which has been outlined throughout the previous sections. Simulations have been carried out at varying count rates in order to assess the maximum throughput of counts for each algorithm. Here the simulation is extended to a random series of events across the 30 to 125 keV (bins 6 to 25) energy range. With this the ability of each algorithm to reproduce the input spectrum from the simulated RTSE can be examined and quantified.

4.5.1   Simulation of Algorithm 1

A simulation was carried out for Algorithm 1 using the data set of one million RTSE. Fig 4-11 shows the simulated output spectra for various input count rates[iv]. As can be seen the total number of events in the output spectrum decreases with increasing input count rate. This is due to the increase in the number of piled up events as a function of count rate.

[iv] Note Fig 4-11 and subsequent figures are plotted using a scatter plot style with straight lines joining points. This is not an entirely precise representation as each energy bin occupies a finite width along the x axis however this style of plotting is advantageous as it enables differences to be seen more easily where multiple spectra are plotted on a single graph and does not compromise the conclusions drawn.
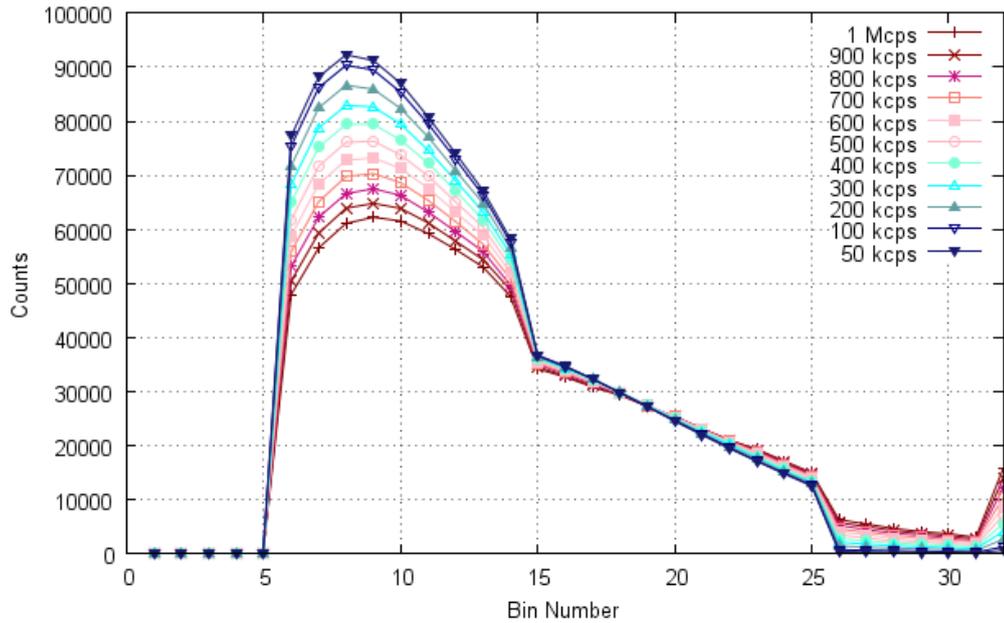
Fig 4-11 Spectra produced by pulse height detection Algorithm 1 for various input count rates using a data set of one million random events from 30 keV to 125 keV.

In addition to the counting losses shown in Fig 4-11 distortion of the output spectrum can also be observed due to the incorrect assignment of piled up events. Events which are piled up are incorrectly binned into higher energy bins by the algorithm resulting in a reduction in low bin events and an excess of high bin events.

This can be seen more clearly in the normalised deviations plot in Fig 4-12. Here the deviations plot is the difference between the bin count in the output spectrum and the input spectrum for various input count rates. This is then normalised by the bin count in the input spectra as described in Equation 4-9.
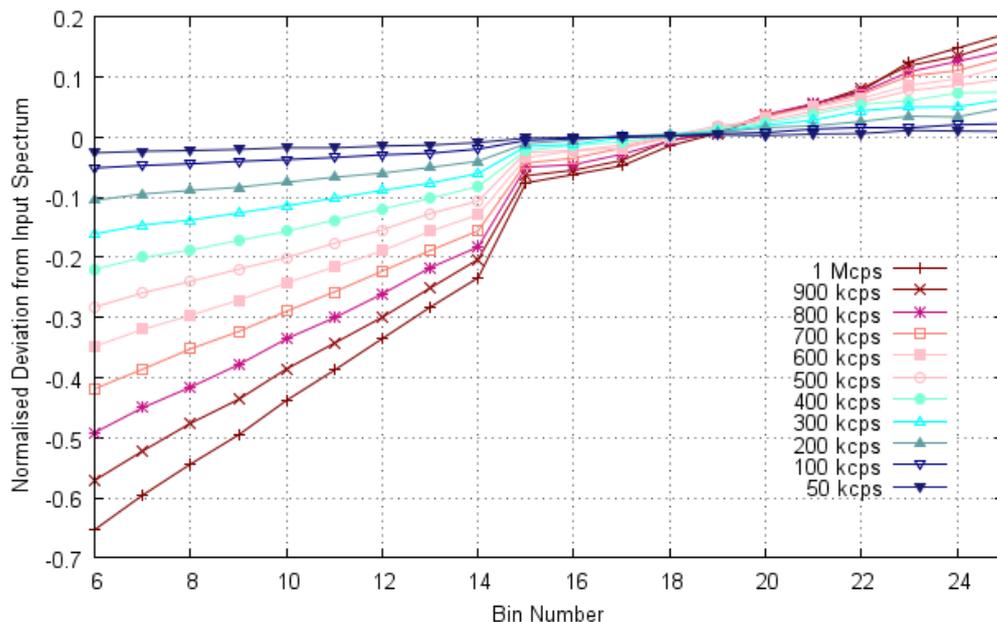
Fig 4-12 Normalised deviations plot of Algorithm 1. Here the deviation of the normalised output spectrum from the normalised input spectrum is shown as a function of bin number.

The large counting losses and spectral distortion from this algorithm make it undesirable for high count rate operation. This will be compared to the performance of Algorithms 2 and 3 in Section 4.5.4.

4.5.2 Simulation of Algorithm 2

Algorithm 2 was simulated using the same one million RTSE as in the previous section. The addition of pulse pile up rejection criteria reduces the spectral distortion but increases the counting losses. This can be seen by the large reduction in the counts in Fig 4-13 at increased count rates.

90
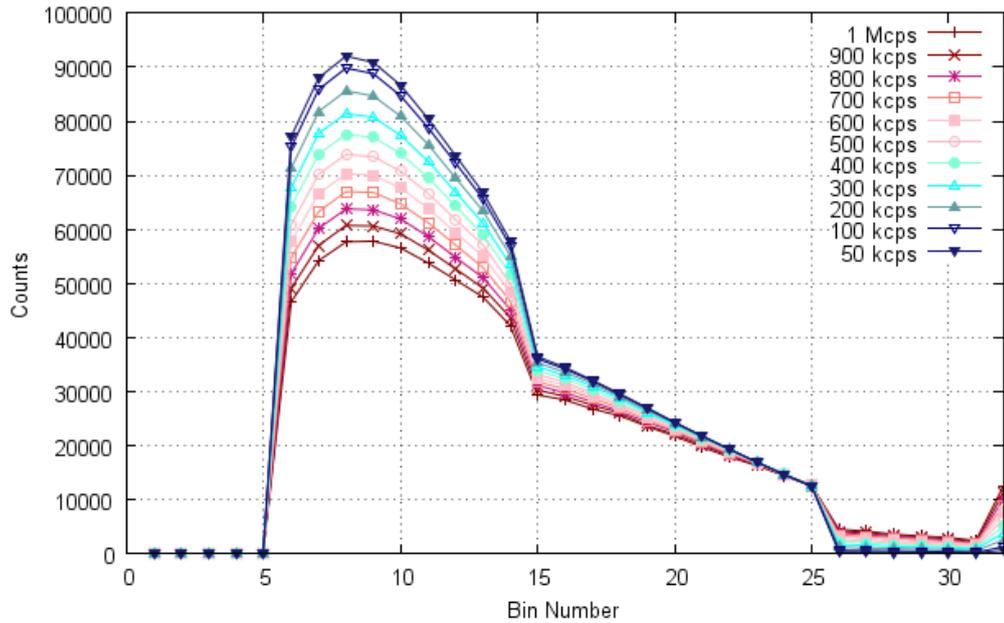
Fig 4-13 Spectra produced by pulse height detection Algorithm 2 for various input count rates using a data set of one million random events from 30 keV to 125 keV.

The normalised deviations plot in Fig 4-14 shows a reduced level of energy distortion due to the discarding of detected piled up pulses. The deviation from the input spectra reduces as a function of energy and shows no significant deviation in the positive region of the graph. This is because unlike Algorithm 1, pulses which are detected as piled up are discarded rather than being assigned to higher energy bins.

The large negative deviation in the low bins shows that incorrect bin assignment still occurs with this algorithm. As with Algorithm 1 the undetected piled up pulses are incorrectly assigned to higher energy bins.
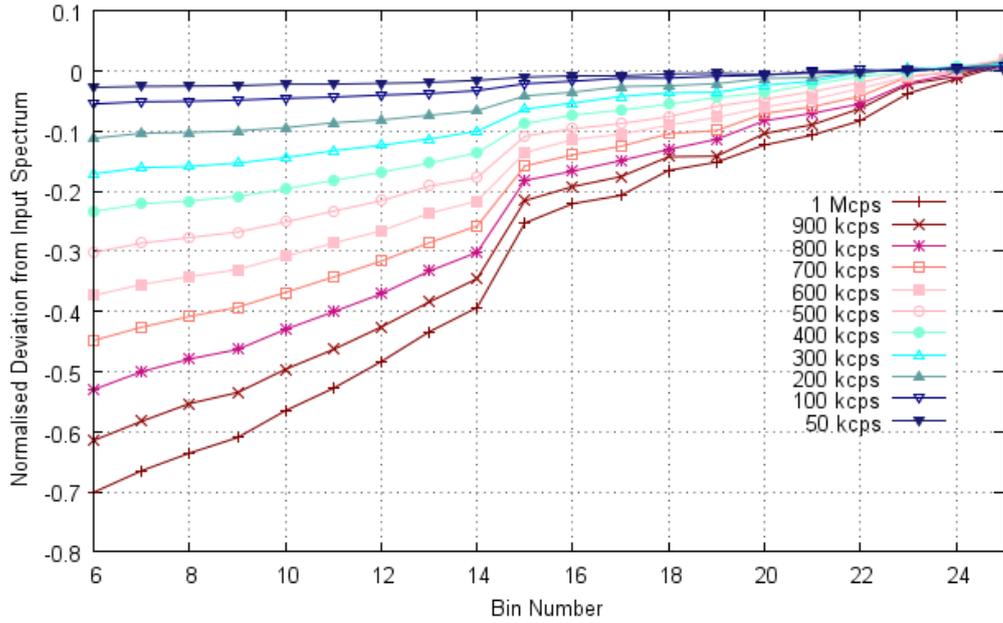
Fig 4-14 Normalised deviations plot of Algorithm 2. Here the deviation of the normalised output spectrum from the normalised input spectrum is shown as a function of bin number.

4.5.3 Simulation of Algorithm 3

The output spectra from Algorithm 3 shows reduced counting losses due to the adding back of deleted counts into the spectrum. As a result the output spectra shown in Fig 4-15 are more closely matched to the input spectrum.
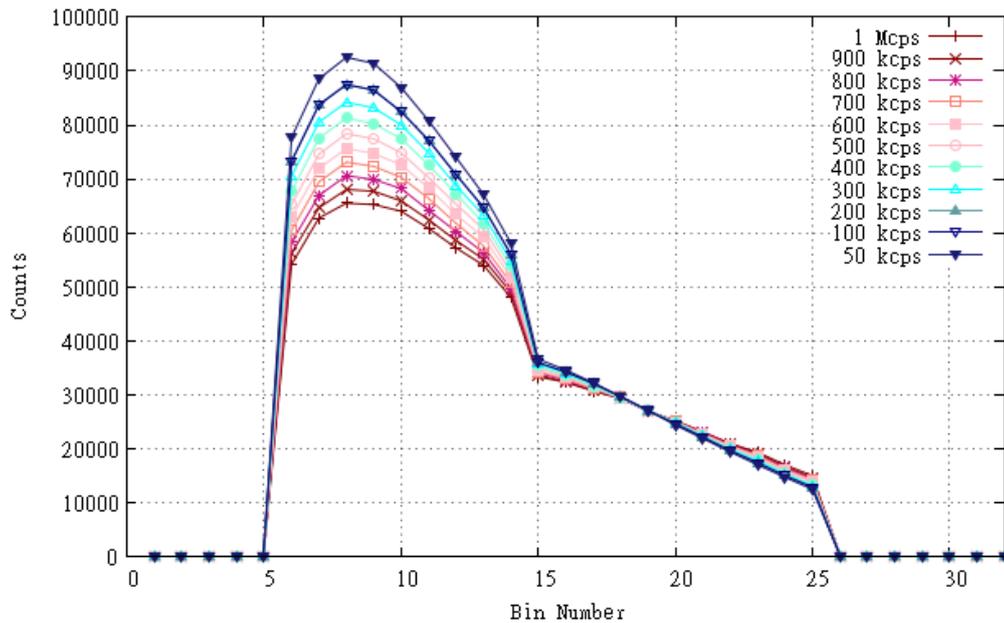

Fig 4-15 Spectra produced by pulse height detection Algorithm 3 for various input count rates using a data set of one million random events from 30 keV to 125 keV. Here discarded counts have been added back into the spectrum by reference to the non piled up output spectrum.

The deviations plot in Fig 4-16 shows the smallest overall range of variation when compared to Fig 4-12 and Fig 4-14 suggesting the best match to the shape of the input spectrum. The pile up rejection is limited by the ability to discriminate very closely piled up pulses and therefore some incorrect bin assignment is still observed giving rise to the characteristic shape.
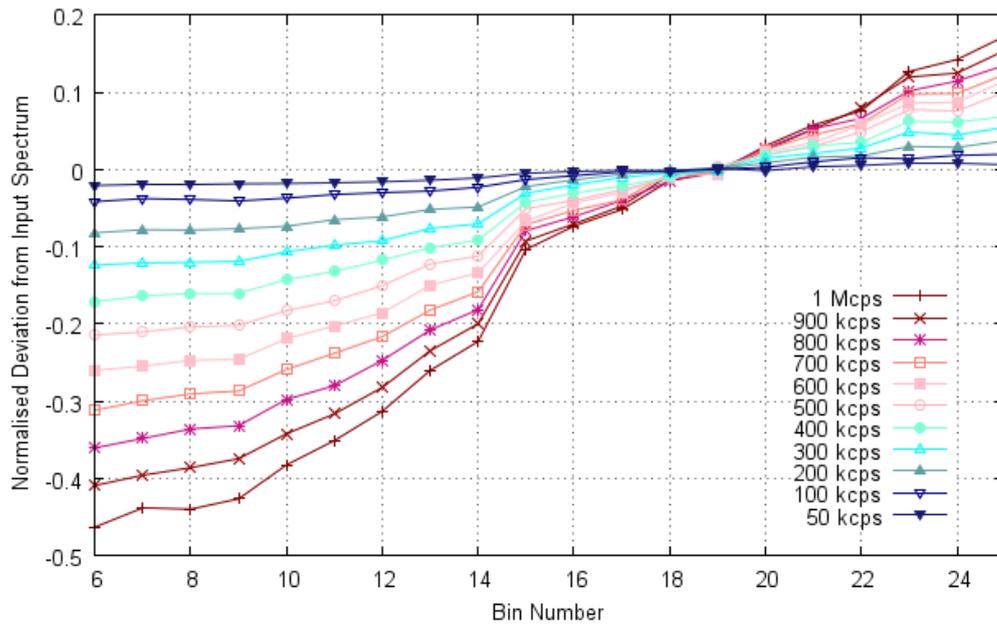
Fig 4-16 Normalised deviations plot of Algorithm 3. Here the deviation of the normalised output spectrum from the normalised input spectrum is shown as a function of bin number.

As the RTSE for this simulation is known, the energy of the events which have led to pulse pile up at the shaping amplifier stage can be identified. This allows the accuracy of the add back approach to be quantified by comparing the energy assignment of the added back counts to the true energy of the piled up events. The deviation of the number of added back counts from that of the true piled up events is shown in Fig 4-17. This is normalised to the input counts for each given bin.
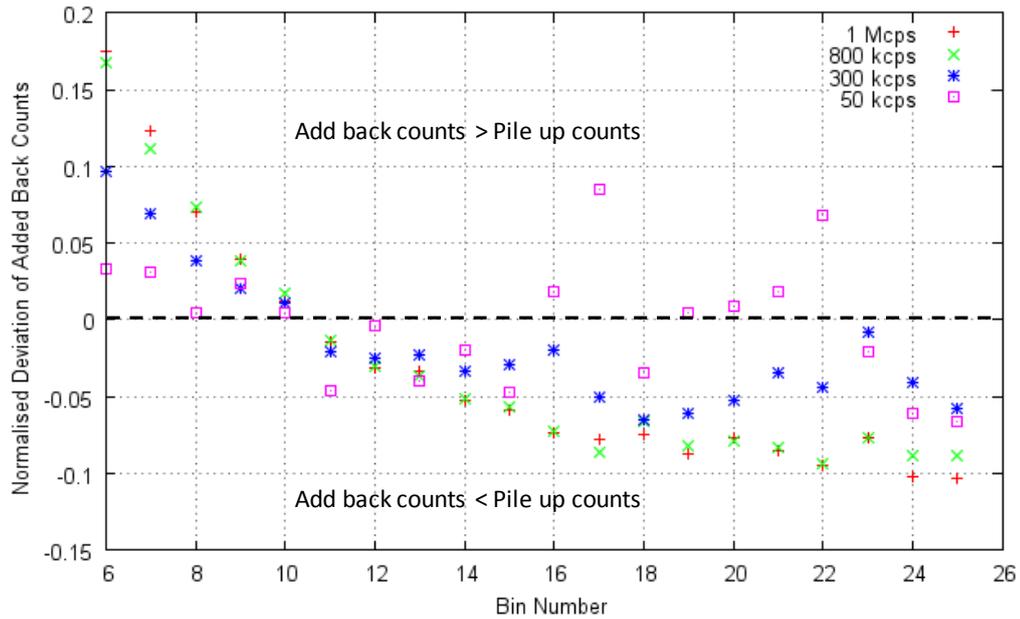
Fig 4-17 Normalised deviation of the added back piled up events from Algorithm 3 from the true energy of the piled up events found by inspection of the RTSE. Note each bin is plotted as a point for greater clarity.

At high input count rates the low energy bins are over compensated by the add back procedure and the high energy bins are under compensated. This is due to the variation in the shaping amplifier base width as a function of energy. High energy pulses have a larger base width and therefore have a greater probability of piling up. This is discussed in more detail in Chapter 7 and a graphical representation of this effect can be seen in Fig 7-1.

4.5.4   Comparison of Algorithms 1, 2 and 3

As seen in the previous sections none of the three algorithms are wholly successful in reproducing the spectral shape or the total counts from the input spectrum. None of the algorithms address the problem of very closely piled up events explaining the positive gradient observed in all of the deviations plots. Variations in the deviations plots in Fig 4-12, Fig 4-14 and Fig 4-16 to the gradient and the crossing point of the energy axis are due to the various ways of dealing with the piled up pulses.

Fig 4-18 shows the spectral distortion from Fig 4-12, Fig 4-14 and Fig 4-16 as a function of input count rate.
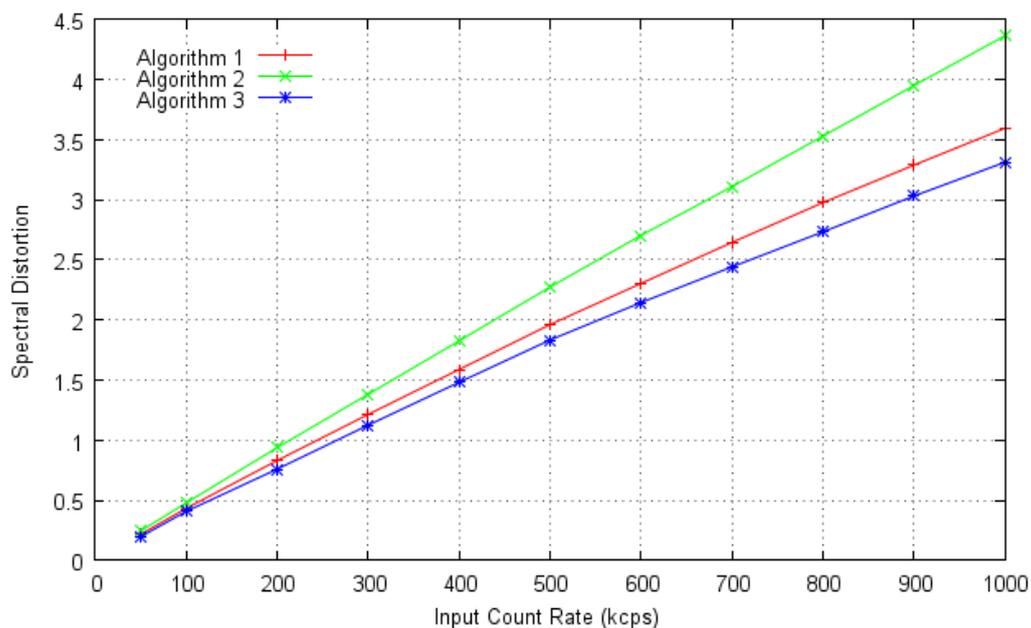
Fig 4-18 Total spectral distortion for Algorithms 1, 2 and 3 across all bins as a function of input count rate.

From Fig 4-18 it can be seen that Algorithm 3 performs most effectively in terms of maintaining spectral shape. The spectral distortions of all three algorithms converge at low count rate due to the negligible probability of pulse pile up. As the algorithms differ only in the treatment of piled up events this convergence is expected.

As the Bottle Scanner application involves a fixed time measurement rather than a total count measurement a more insightful way of analysing the counting losses from the three algorithms is to fix the simulation to one second of acquisition time rather than the acquisition of a total of one million counts. The output counts for each algorithm over a one second simulation time is shown in Fig 4-19 as a function of the input count rate.
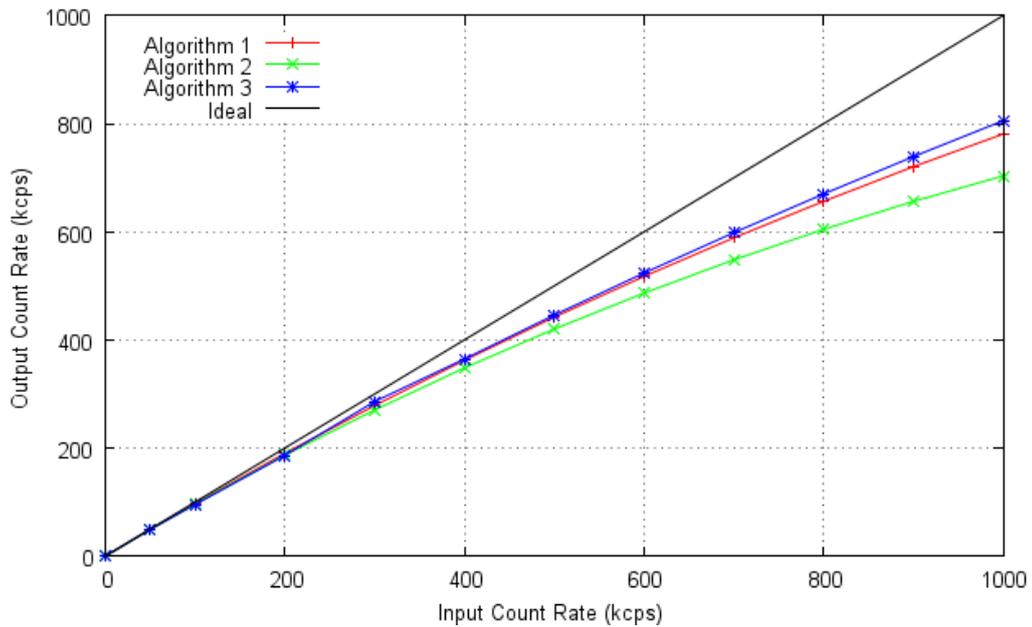
Fig 4-19 Output counts as a function of input count rate for Algorithms 1, 2 and 3 from a simulation of a one second acquisition time.

Algorithm 3 shows the lowest counting losses per unit time followed by Algorithm 1. As expected Algorithm 2 shows the highest counting losses due to the discard of piled up counts and the absence of any add back procedure. This could be regarded as operating in a manner similar to that described by the paralyzable system outlined in Section 3.14.

From Fig 4-18 and Fig 4-19 it is clear that Algorithm 3 performs best both in minimising spectral distortion and counting losses.

4.5.5   Problems Associated with Adding Back Piled up Pulses

Deleting piled up pulses results in the loss of information and this cannot be precisely regained by direct reference to the output spectrum. This is because the counts in the output spectrum have all arisen from pulses which were not piled up, the use of this information in order to back predict the true spectrum relies on the assumption that the energy distribution of piled up pulses is identical to that of the non piled up pulses in the output spectrum.

One clear illustration of this is in Fig 4-17 . The simplistic approach of adding back pulses to the spectrum in ratios relative to the number of counts in the output (non piled up) spectrum leads to errors due to the variability in pile up probability as a function of energy – large pulses having wider base widths are

more likely to pile up. In general a prior knowledge of the incident spectra is required in order to add back the piled up events.

Such problems are widely discussed in the literature and a detailed discussion closely relating to the problem faced here is given in [67,68,69]. One approach is to collect a low count rate equivalent spectrum where pulse pile up is negligible. This approach is not easily realisable with the current experimental setup and presents a range of problems which make it an unfeasible approach for such an application.

A full statistical treatment is required in order to satisfactorily add back such discarded counts and is beyond the scope of this work. Future work is planned to exploit the advent of very fast analogue to digital conversion and pulse processing in order to perform real time front end analysis within an FPGA. This is expected to lead to improvements as preamplifier pulses occupy a shorter time interval and are therefore not reliant on statistical approximations.

4.6   Conclusion

In this chapter the design of a pulse height detection algorithm for the Bottle Scanner system has been discussed. The primary characteristics of the algorithm are defined by the materials identification procedure. This procedure requires a pulse height analysis system which produces stable reproducible spectra. Errors including the Poisson error must be kept to a minimum in order to enable the system to distinguish between subtle differences in transmission spectra from different liquids.

The major source of error in this high count rate system originates from pulse pile up. This was addressed by adding varying levels of pile up handling into the three pulse height detection algorithms. The algorithms were then evaluated by Monte Carlo simulation of an incident x-ray spectrum. For a supposed operating condition of 300 $kcps$ the counting losses and spectral distortion are summarised in Table 4-1.

	Algorithm 1	Algorithm 2	Algorithm 3
Counting Losses (%)	7.7	10.9	4.9
Spectral Distortion	1.4	1.2	1.1

Table 4-1 Counting losses and spectral distortion for Algorithms 1, 2 and 3 at an input count rates of 300 $kcps$.

Algorithm 1 is the most simple of the three algorithms proposed and does not include any means of rejection or correction of piled up pulses. Consequently the behaviour at count rates exceeding a few hundred thousand counts per second

100

shows large counting losses and spectral distortion. Algorithm 2 in contrast shows lower spectral distortion at high count rates due to the discarding of piled up counts however this results in larger counting losses.

Whilst Algorithm 3 appears to offer the best solution both in terms of minimising spectral distortion and counting losses, the reliance on the output spectrum to perform the add back procedure may potentially lead to errors in the final spectrum. For this reason it was decided that Algorithm 2 offeres the best performance for the required application. The use of this algorithm represents a trade off between counting losses and spectral distortion. This choice is justified by the perceived value of the informational content of the spectral shape over that of the absolute counts when designing materials identification algorithms.

Future work is planned to find an improved statistical approach to adding back counts to the spectrum. This is aimed at removing the energy dependence of the add back procedure shown in Fig 4-17 and reinstating true Poisson uncertainty. In addition to this a faster A to D and FPGA may allow some form of deconvolution of piled up pulses to be carried out.

Chapter 5 Experimental Results from Pulse Height Detection Algorithms

5.1 Introduction

In this chapter experimental results will be presented from pulse height detection Algorithms 1 and 2 which were modelled in Chapter 3. Initial system tests using an emulation of Algorithm 1 programmed to run on an Agilent DSO90254A oscilloscope are discussed. The results from this were used to validate the efficacy of the algorithms prior to programming onto an FPGA. These results are then compared to an acquisition carried out on a commercially available Canberra Multiport II MCA and to the same algorithm implemented in firmware on an FPGA.

The effect of shaping time on resolution is shown at a low count rate by acquisitions using a ^{57}Co source and $100\,ns$ and $50\,ns$ shaping amplifiers. Results from high count rate x-ray measurements are discussed in Section 5.4 and the linearity of Algorithms 1 and 2 are tested as a function of beam current and shaping time. The spectral variation as a function of count rate is also

presented and shows good overall agreement to the modelling work carried out in Chapter 3.

It is also shown that both algorithms exhibit artefacts due to pulse pile up. The effect of this pulse pile up on the transmission spectrum is discussed in Section 5.5 and is shown to produce curves with a rollover in intensity at high energies which appears counter to the basic physics. It is also shown that due to pulse pile up the shape of the transmission spectra vary as a function of input count rate. This is detrimental to the operation of the Bottle Scanner and means that the procedure of normalisation of spectra against an open beam, I_0 measurement is ineffective. Methods of reducing this effect are discussed in Section 5.6.

Results from tests of threat items are shown in Section 5.8 and highlight the difficulty in detection of threats due to the similarity in transmission spectra which arises from the low x-ray interaction cross section of liquids and further reinforces the need for a stable system with minimal variance with respect to the input count rate.

5.2   Matlab Emulation of FPGA Algorithms

A Matlab program was written to emulate Algorithms 1 and 2 in order to test their efficacy prior to implementation on an FPGA. This method of algorithm testing is very useful as it allows easy debugging prior to implementation on an FPGA and can then be used as a reference from which to test the final FPGA firmware. This was done using an Agilent DSO90254A oscilloscope controlled using software written in Matlab.

A sampling frequency of $200\,MHz$ was selected in order to match the clock speed of the target Altera Cyclone II FPGA and an Analogue Devices AD9480 A to D converter. The memory depth of the scope was reduced to 1024 points in order to minimise the CPU time required to transfer and analyse the data. A rising edge hardware trigger was set at 63 mV in order to ensure that only events crossing this voltage threshold were passed to the program. The use of a hardware trigger minimises the amount of CPU time required to analyse events which do not pass the low level discriminator condition set by the algorithm, thereby increasing the efficiency of the software.

Once an event has been triggered the voltage and time data are passed in array form to the Matlab program. The program converts the high precision voltage measurements from the oscilloscope into 8 bit values in order to match the precision of the A to D converter in the real system. These values are then passed to Algorithms 1 and 2. Once pulse height measurements have been returned by

105

Algorithms 1 and 2 the oscilloscope is rearmed in order to capture the next event. This is repeated until the desired number of events has been acquired.

Unlike the FPGA implementation it is not possible to make a real time acquisition with this software due to a dead time between triggers. This dead time consists of the time taken to pass the data to the Matlab program, the analysis time and finally the time taken for the program to rearm the oscilloscope trigger. Therefore rather than acquiring for a fixed measurement time the program is instead set to acquire a predetermined number of events. The time taken to acquire these events is a function of both the count rate and the system dead time.

This approach is used in this chapter in order to validate the FPGA algorithms and again in Chapter 7 in order to perform more advanced analysis of the shaped pulses. In all cases the number of acquired events is 100,000. Fig 5-1 shows the spectrum captured using the Matlab emulation of Algorithm 1 with a ^{57}Co source.
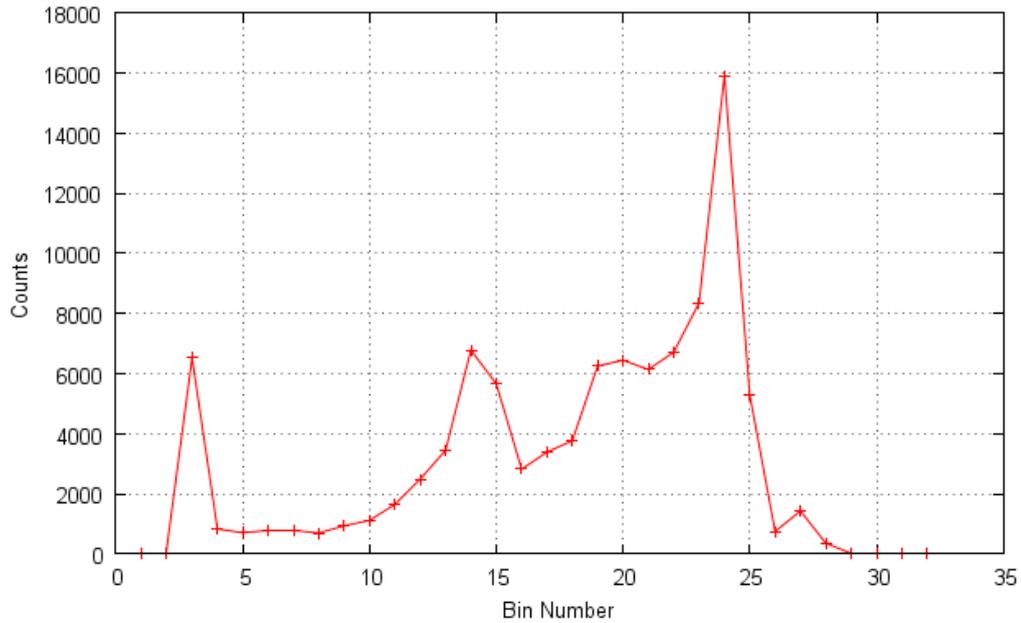
Fig 5-1 [57]Co spectrum captured using an oscilloscope emulation of Algorithm 1 with an Amptek XR-100T detector and a Cremat CR-200-100ns shaping amplifier. A total of 100,000 events were captured during this acquisition.

As shown the algorithm returns spectra of the expected general shape. The main peak in bin 24 is from the 122.1 keV [57]Co emission line and the smaller peak in bin 27 is from the 136.5 keV emission line [59]. The peak centred around bin 14 is a lead fluorescence peak and originates from the lead source holder which has an energy of 74.96 keV [70].

The following section shows a back to back comparison of both the oscilloscope and FPGA implementations of Algorithm 1 together with the [57]Co spectrum captured from the Canberra Multiport II MCA.

5.2.1 FPGA Test of Algorithm 1 using a ^{57}Co Source

Following emulation and testing using an oscilloscope, Algorithms 1 and 2 were coded in the hardware design language Verilog HDL [66] and programmed onto an FPGA. The algorithms were then tested as in the previous section using a low count rate ^{57}Co source.

Results shown here are for Algorithm 1 only as the low count rate of the ^{57}Co source results in identical outputs from both algorithms. Fig 5-2 shows a comparison between the oscilloscope and FPGA implementations of Algorithm 1 along with the Multiport II acquisition from Fig 3-5. The total number of counts in each spectrum have been normalised to one for comparison purposes and the spectrum acquired using the Multiport II MCA has been re binned into 32 bins.
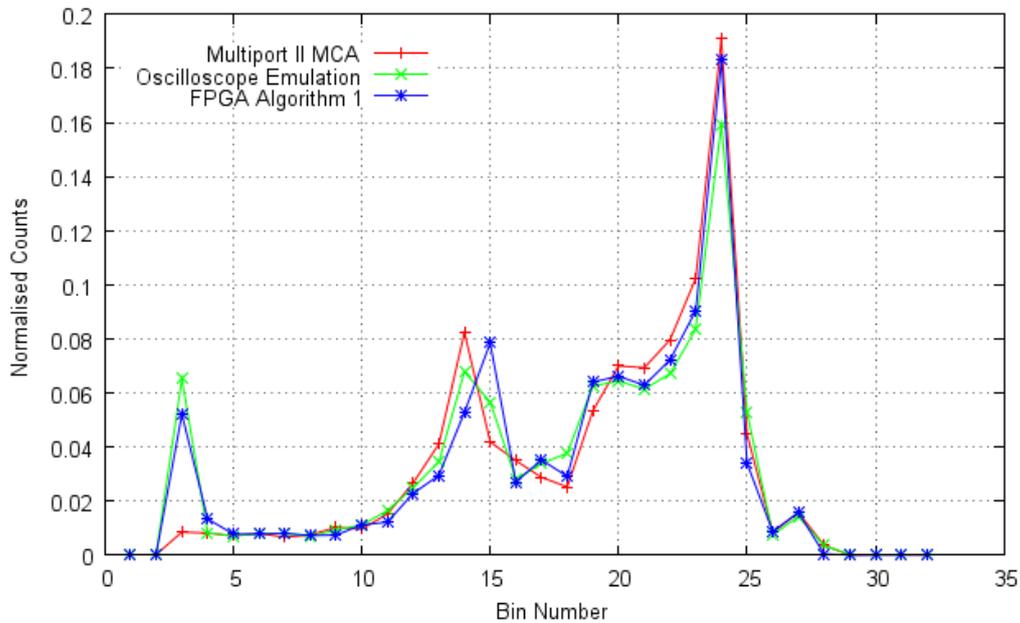
Fig 5-2 Comparison of ^{57}Co spectra acquired using oscilloscope and FPGA implementations of Algorithm 1 along with an acquisition taken using a Canberra Multiport II MCA. Here the Multiport II spectrum shown is from Fig 3-5 and has been re binned into 32 bins for comparison.

The acquisition time for the FPGA and Multiport II measurements was 300 seconds and the oscilloscope measurement was programmed to record 100,000 total events giving an approximately equal number of total counts in each spectrum.

As shown in Fig 5-2 the spectrum acquired from the FPGA is in good agreement with that of both the oscilloscope implementation of Algorithm 1 and the Multiport II MCA. This shows that the bin assignment methodology and the hardware are performing as expected. It is important to note however that this test was carried out at a low count rate and therefore does not assess the effects of pulse pile up on the output spectrum.

In order to assess the statistical significance of the slight differences in spectral shape from Fig 5-2, ten acquisitions were carried out using the FPGA and oscilloscope. The normalised spectra are plotted in Fig 5-3 with error bars.
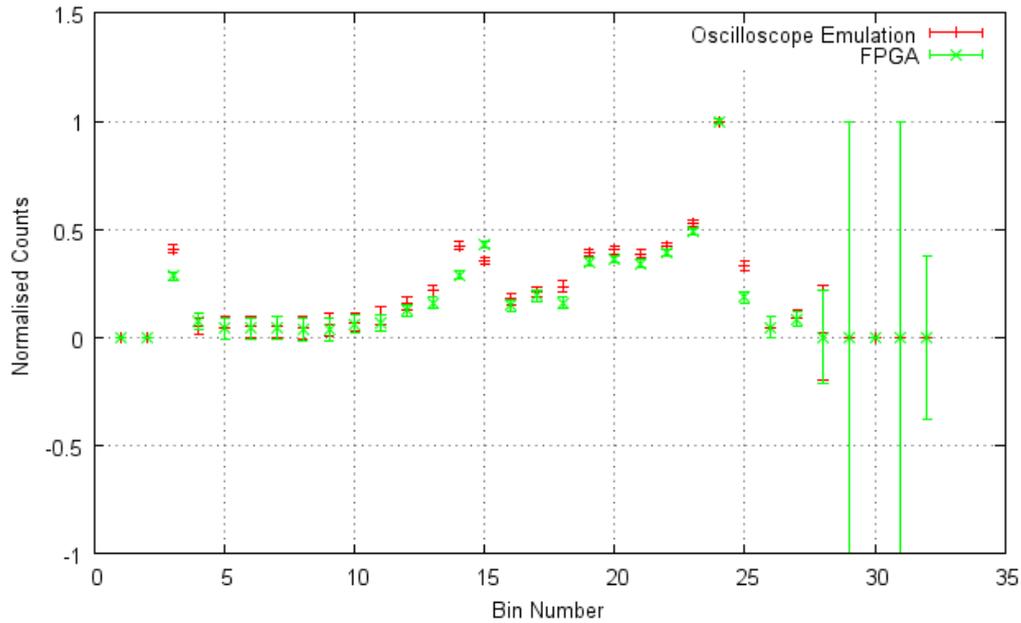
Fig 5-3 Graph showing ^{57}Co spectra using an oscilloscope emulation of Algorithm 1 and an FPGA running the same algorithm in firmware. The error bars are derived from ten repeat measurements.

The difference in the acquired spectra is marginally outside the error bars for certain bins. The major differences occur around bins 14, 15 and 25 which relate to regions of high local gradients between bins. Such regions are more susceptible to slight variations in calibration between the ADC used in the FPGA and in the oscilloscope. This level of agreement was deemed suitable for the purposes of testing the general functionality of the algorithm and of the FPGA hardware.

5.3   The Effect of Shaping Time on Resolution

As the XR-100T detector is a planar device, the signal is composed of the induced charge from both electrons and holes. The mobility of holes is typically around 10 times lower than that of electrons resulting in sweep-out times which are limited by the velocity of the hole charge. This sets a lower limit on the shaping time of the shaping amplifier.

Assuming a hole mobility of $100\ cm^2V^{-1}s^{-1}$ and a constant electric field of $6000\ Vcm^{-1}$ ($600\ V$ applied across a $1\ mm$ thick detector), the sweep-out time for a charge generated at the anode is approximately $170\ ns$ and represents the maximum theoretical sweep-out time for the device. For a typical electron mobility of $1100\ cm^2V^{-1}s^{-1}$, the sweep-out time for a charge generated at the cathode is approximately $15\ ns$ and represents the minimum theoretical sweep-out time for the device.

Fig 5-4 shows oscilloscope traces for the longest and shortest detected sweep-out times from the XR-100T detector. Whilst complete characterisation of the CdTe detector is not possible due to its inaccessibility, the difference in sweep-out times from the above values is clear.
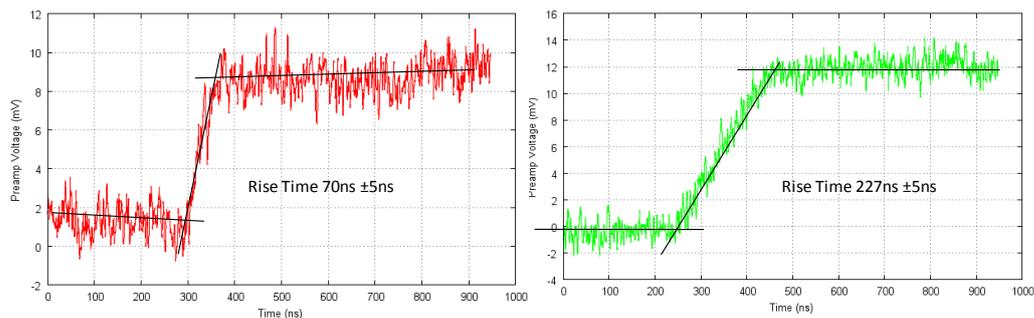
Fig 5-4 Preamplifier traces captured from the XR-100T detector illuminated by a [57]Co source. The traces on the left and right of the figure represent the fastest and slowest rise times observed from this detector respectively.

The signals have significantly longer rise times than predicted by the calculation above. These longer rise times are believed to be due to several factors including parasitic impedances such as series inductance and shunt capacitance in the measurement circuit. Additionally, incomplete depletion of the space charge inside the detector has been reported[71,72] to result in a region of low electric field close to the contact.

These long sweep-out times lead to a ballistic deficit problem for short shaping times. This can be seen in Fig 5-5. Here a [57]Co spectrum was acquired with an FPGA using a $100\ ns$ shaping time CR-200-100ns and $50\ ns$ shaping time CR-200-50ns shaping amplifier. In order to account for the reduced shaping time in the case of the $50\ ns$ shaper the firmware was modified to reduce the samples to peak from 40 samples to 22.
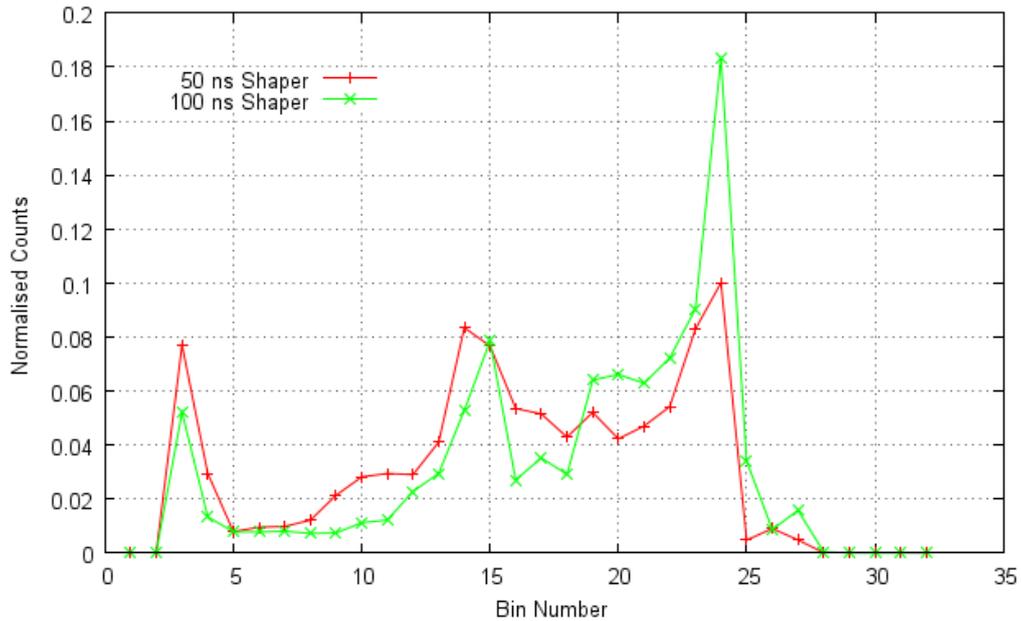
Fig 5-5 ^{57}Co spectra from an XR-100T detector with various shaping times. MCA spectrum captured using an FPGA programmed with Algorithm 1[v].

A ballistic deficit effect is observed in the cases where the shaping time is not long enough to capture the entire preamplifier pulse height. This results in pulse height dispersion as the pulse height becomes dependant on the rise time of the preamplifier signal which is in turn a function of the depth of interaction of the incident x-ray or gamma ray. As shown in Fig 5-5 the resulting pulse height spectrum is degraded and shows the characteristic hole tailing to the low energy side of the 122.1 keV peak.

The competing requirements of count rate and resolution often require a compromise to be made in shaping time selection. A method of correcting for the degraded resolution resulting from a reduced shaping time is discussed in Chapter 7 which enables an appropriate shaping time to be selected largely on

[v] Note the peak positions are unaffected by the change in shaping time as the system gain was adjusted to correct for this.

the grounds of count rate requirements. The corresponding degradation in the pulse height spectrum is then corrected by a computational method.

5.4 High Count Rate Tests

In this section results from the high count rate performance testing of the algorithms in a Bottle Scanner system will be discussed. All measurements were carried out on a single Bottle Scanner and algorithms were tested by re programming the firmware on the same FPGA.

A pyrex cuvette of water with a path length of 100 mm is used in the tests described in this section, here the path length is defined as the straight line distance through the cuvette along the x-ray beam path. The cuvette is designed for use in a spectrophotometer and hence the path length, wall thicknesses and optical properties are highly controlled. A specially designed holder is also used to minimise alignment errors. This setup therefore represents the ideal measurement condition without many of the variables expected when in operation in the field.

All measurements in this section were acquired using an FPGA and a total of 10,000 frames each of $16\,ms$ in length were collected for each spectrum giving an acquisition time of 160 seconds.

5.4.1   X-ray Spectra from Algorithm 1

The x-ray spectrum from Algorithm 1 was acquired at a beam current of 0.104 mA and a tube voltage of 160 kV using the CR-200-100ns and CR-200-50ns shapers. The results are shown in Fig 5-6. The total counts in each spectrum have been normalised for comparison. As can be seen the spectra show similar overall shape however the tungsten fluorescence peaks are less visible with the 50 ns shaper due to the poorer resolution. Also observable is the accumulation of counts in bin 32. These originate from events with a pulse height of greater than or equal to 1 V and are predicted by the model in Chapter 4. The spectra acquired using a 100 ns shaping time shows higher accumulation of counts in bin 32 due to the greater susceptibility to pulse pile up.
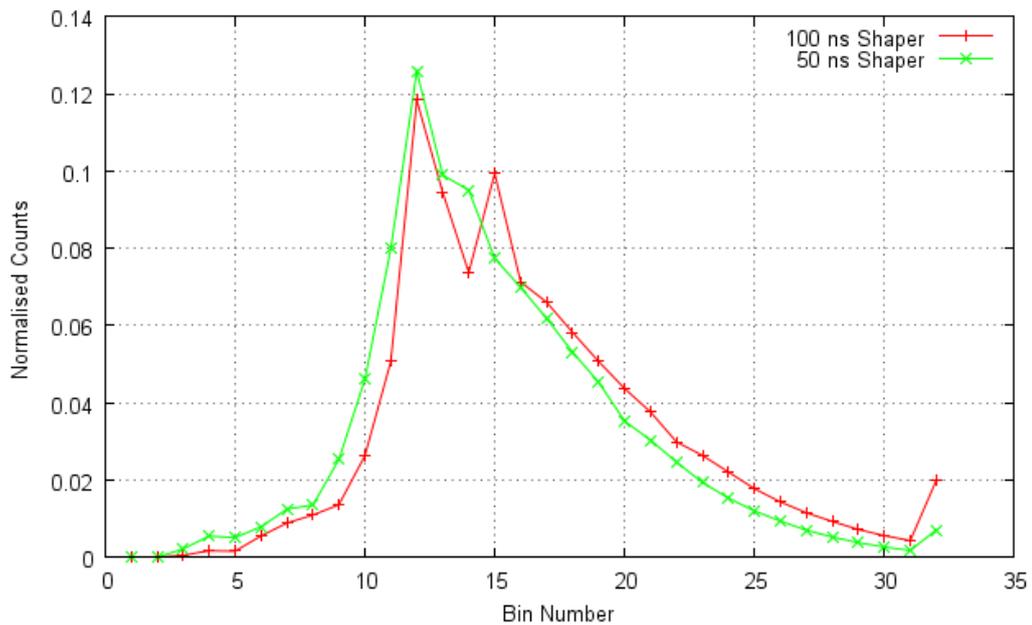
Fig 5-6 Graph showing the x-ray spectra acquired using Algorithm 1 on FPGA. Shaping times of 100 ns and 50 ns were selected. The x-ray beam current was 0.104 mA and the tube voltage was 160 kV.

5.4.2   Linearity Testing of the Detector and Electronics

The throughput of counts was investigated by plotting the total count rate across all bins as a function of x-ray beam current. This measurement was carried out for both Algorithms 1 and 2, using $50\,ns$ and $100\,ns$ shaping times. The rate of x-ray emission from the x-ray tube is directly proportional to the beam current and therefore any deviation from proportionality implies counting losses due to pulse pile up. Count rate proportionality with beam current is clearly not directly measurable as all detectors behave nonlinearly with count rate, however calculations based on the emission rate from an x-ray tube show this to be the case [73]. In addition many published results exist showing proportionality at low beam currents (count rates)[74].

Fig 5-7 shows a plot of the total count rate as a function beam current for both $50\,ns$ and $100\,ns$ shaping times using Algorithms 1 and 2. The acquisition time for each measurement was 160 seconds.
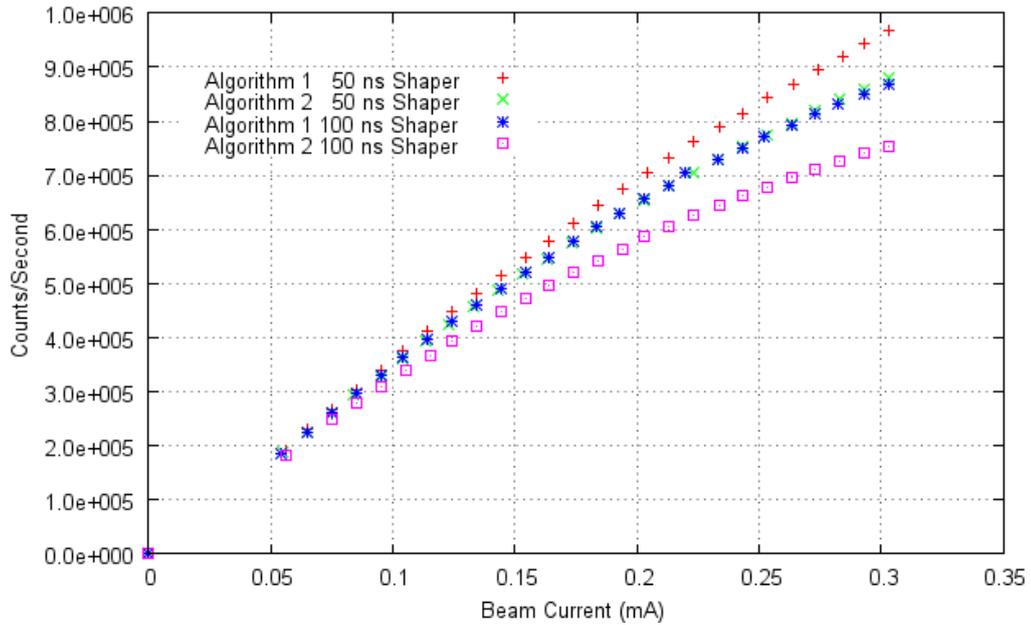
Fig 5-7 Count rate as a function of beam current for Algorithms 1 and 2 with shaping times of 50 *ns* and 100 *ns*.

The results in Fig 5-7 are as predicted by the modelling from Chapter 4. Algorithm 1 performs better in terms of the throughput of counts. By reducing the shaping time to 50 *ns* the throughput of counts is improved for both algorithms however as illustrated in Fig 5-5 the shorter shaping time reduces energy resolution due to ballistic deficit effects.

Due to limitations on the x-ray beam current the paralyzable nature of Algorithm 2 cannot be fully demonstrated. It is clear from Fig 5-7 that this algorithm shows poorer performance in terms of the total throughput of counts as predicted by the modelling work in Chapter 4.

5.4.3   Spectral Variation with Count Rate

In Chapter 4, the spectral variation as a function of count rate was studied using a series of randomly time distributed events. The key observed difference between Algorithms 1 and 2 was related to the loss of counts at the low end of the spectrum, in Algorithm 1 these were observed to shift to higher energies due to pulse pile up. This effect gave an apparent rotation about bins 18 to 20 as two or more low energy events were incorrectly binned as single or multiple higher energy events. The same was true for Algorithm 2 except the incorrect assignment of secondary pulses piled up with the first pulse is largely prevented due to the paralyzable nature of the algorithm. This resulted in a reduced rotational symmetry as a deficit in the low energy region of the spectrum did not transfer to the high energy region.

Fig 5-8 shows the output of the FPGA as a function of beam current for Algorithm 1. As can be seen the rotational variation in count rate predicted by the model is present in the real system. The centre of rotation also agrees with the model occurring around bin 19. The magnitude of the deviation also increases as a function of count rate as expected from the pulse pile up model.
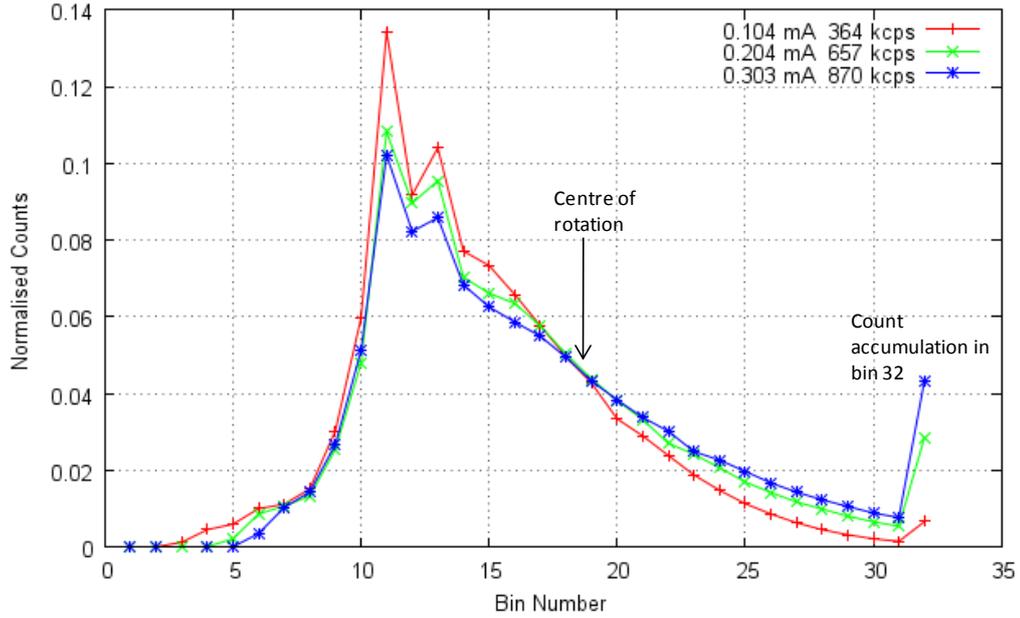
Fig 5-8 X-ray spectra captured using Algorithm 1 implemented on an FPGA with an XR-100T detector and a Cremat CR-200-100ns shaping amplifier. The total counts in all spectra have been normalised to one for comparison purposes.

5.4.4 X-ray Spectra from Algorithms 1 and 2

X-ray spectra were acquired for using Algorithms 1 and 2 with an x-ray beam current of $0.303 \, mA$ and a tube voltage of $160 \, kV$ using the $50 \, ns$ shaper. The spectra are shown in Fig 5-9. The measured count rates for Algorithms 1 and 2 were $967.6 \pm 0.7 \, kcps$ and $879.8 \pm 0.9 \, kcps$ respectively. Such count rates represent a condition with a significant amount of pulse pile up and are therefore useful in demonstrating the differences between the two algorithms.
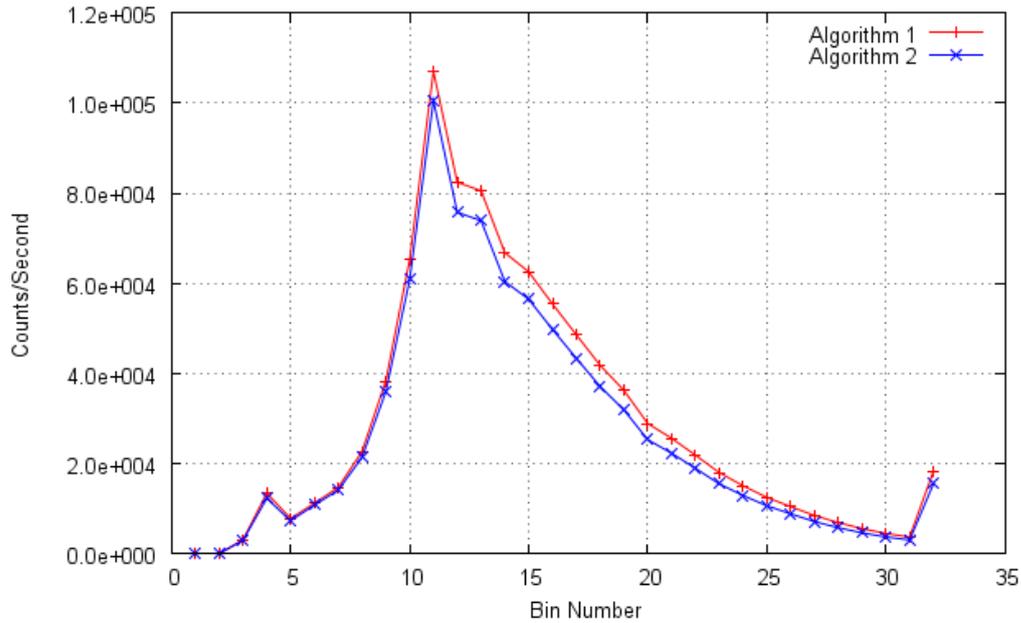
Fig 5-9 Graph showing the I_0 spectra acquired using Algorithms 1 and 2 with a beam current of 0.303 mA and a tube voltage of 160 kV using a CR-200-50ns shaper. The acquisition time for these spectra was 160 seconds.

Both algorithms show very similar characteristics in the low energy region with Algorithm 2 showing 6% lower counts at the peak and 9% lower counts overall. This is expected due to the paralyzable nature of Algorithm 2. The largest variation is in the high energy region above the main peak in bin 11. As expected Algorithm 1 shows higher counts in this region due to incorrect binning of piled up pulses from lower bins. Also clear from Fig 5-9 are the piled up counts in bin 32 which are higher in the Algorithm 1 spectrum.

These effects can be better seen in Fig 5-10 which shows a deviations plot of the normalised spectra from Fig 5-9.
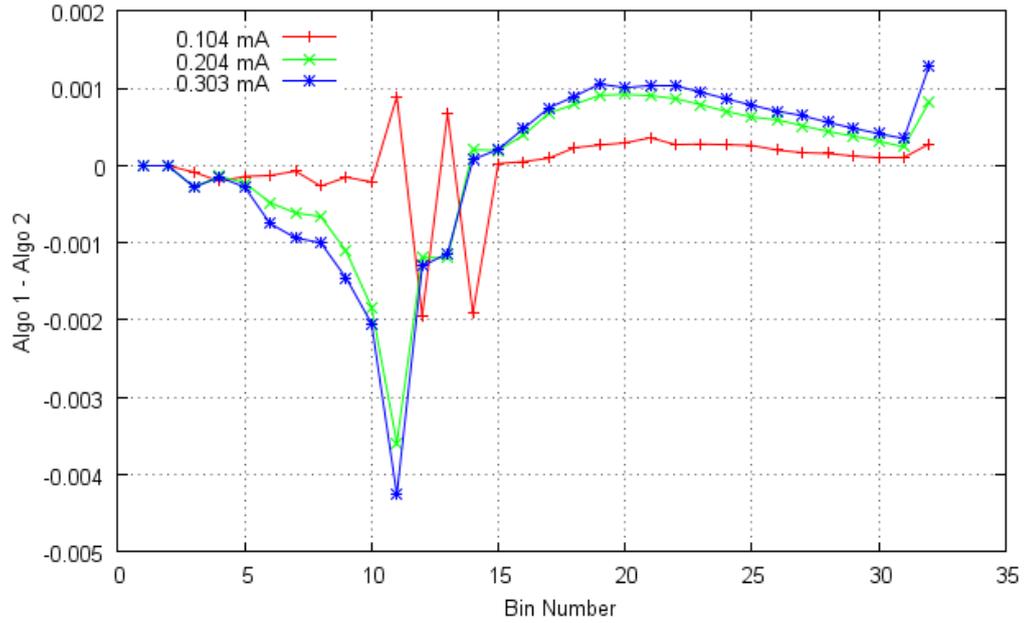
Fig 5-10 Plot showing the difference in counts between Algorithms 1 and 2 as a function of bin number for various beam currents. Here the total counts in each spectrum was normalised to one. A CR-200-50ns shaper was used for this measurement.

Algorithm 2 shows proportionally higher counts in the low energy part of the spectrum giving rise to the negative region between bins 1 to 14. This is because a smaller proportion of piled up pulses are wrongly assigned to higher energies and hence the high energy region of the graph from bin 15 onwards is positive.

5.5   The Effect of Pile up on Transmission

Until this point the analysis has been focussed on the variation of the open beam spectrum as a function of count rate. Due to the method of operation of the Bottle Scanner it is in fact the transmission spectrum, I/I_0, which is of most interest. Clearly under normal operating conditions the I_0 spectrum will be acquired at a significantly higher count rate than the I spectrum which results in differing amounts of pulse pile up in the two cases, producing undesirable artefacts in the transmission curve. Fig 5-11 shows transmission spectra using a 100 mm cuvette filled with water.
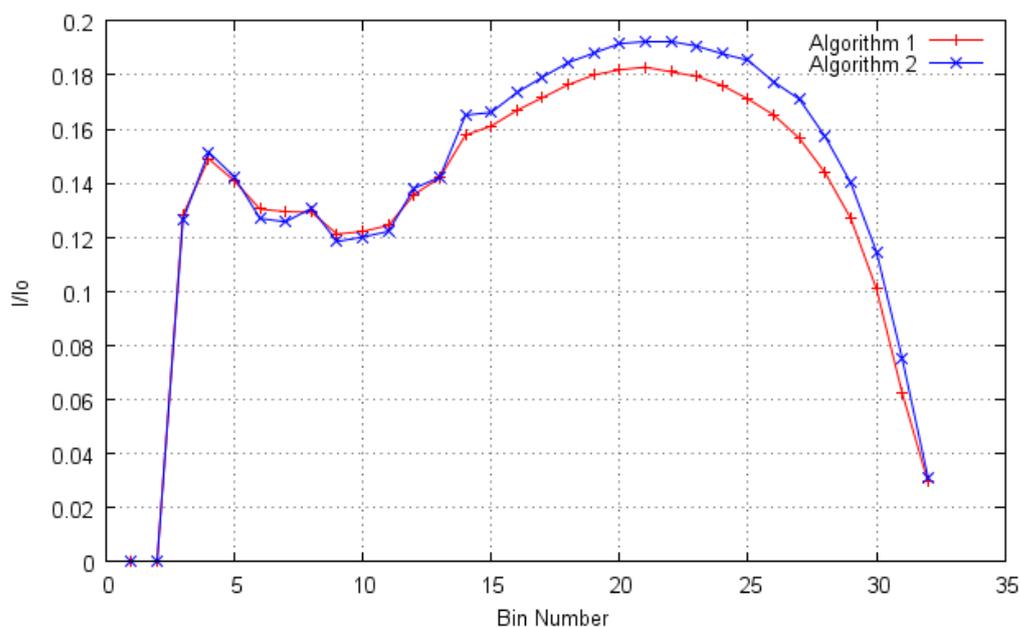
Fig 5-11 Graph showing the transmission spectra from Algorithms 1 and 2 for a cuvette filled with water with a path length of $100\ mm$. Here the beam current was $0.303\ mA$ and the tube voltage was $160\ kV$.

In Fig 5-11 transmission spectra show a rollover at high energies implying a decrease in transmission as a function of energy. This is counter intuitive as the

expected behaviour is a continual increase in transmission as a function of energy towards a value of 1.

This effect can be related back to pulse pile up in the I and I_0 spectra. The count rate in the I_0 measurement is greater than in the I measurement therefore the fraction of pile up is greater. As seen from Chapter 3, any piled up pulses which are not removed from the spectrum contribute towards an upward energy shift in the spectrum. Due to the differing count rates this shift is greater in I_0 than in I, thereby resulting in an artificial increase in the high bin counts in I_0 compared to I.

This can be seen more clearly in Fig 5-12 which is a normalised plot of the individual I and I_0 spectra used to produce the Algorithm 1 transmission spectrum in Fig 5-11. As shown the beam hardening effect of the bottle results in a higher average energy in the I spectrum compared to the I_0 spectrum. The origin of the rollover can be seen to be due to the convergence of the I and I_0 spectrum at high energy due to the upwards shift in the I_0 spectrum arising from incorrectly binned piled up pulses.
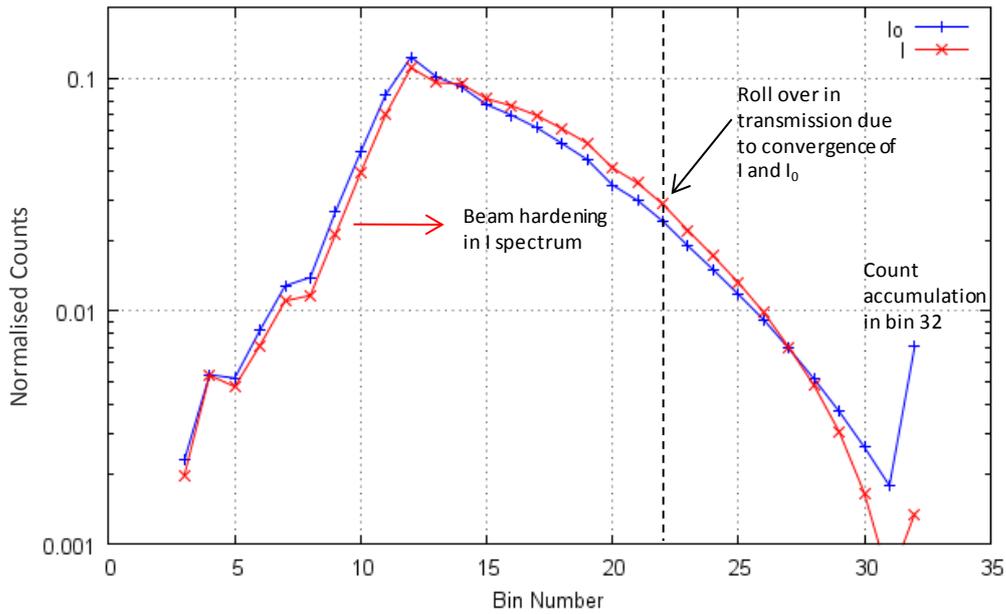
Fig 5-12 Normalised I and I_0 spectra using pulse height detection Algorithm 1. Here the I measurement is taken with a $100 \, mm$ cuvette filled with water in the beam path. Note the log y scale.

The rollover in transmission shown in Fig 5-11 highlights the fact that both algorithms produce spectra with artefacts due to pulse pile up. In the case of Algorithm 2 this is in part due to the fact that the first pulse in any chain of piled up pulses is always added into the spectrum, regardless of whether the pulse height has been affected by subsequent pulses.

This is a very important effect that had not been fully appreciated during the early development of the Bottle Scanner. It was incorrectly assumed that the transmission measurement contained information relating to the sample only, with all information regarding the x-ray beam removed by normalisation. Clearly this is shown here to be incorrect and the result of this has drastically changed the approach to system design and operation.

Fig 5-13 shows the transmission spectra produced by Algorithm 1 for three different beam currents. The beam current range was intentionally selected to be large in order to amplify the effect, and is not a representation of the true operation of the system. However, tolerance to variability in transmission for the purposes of threat identification is extremely small.
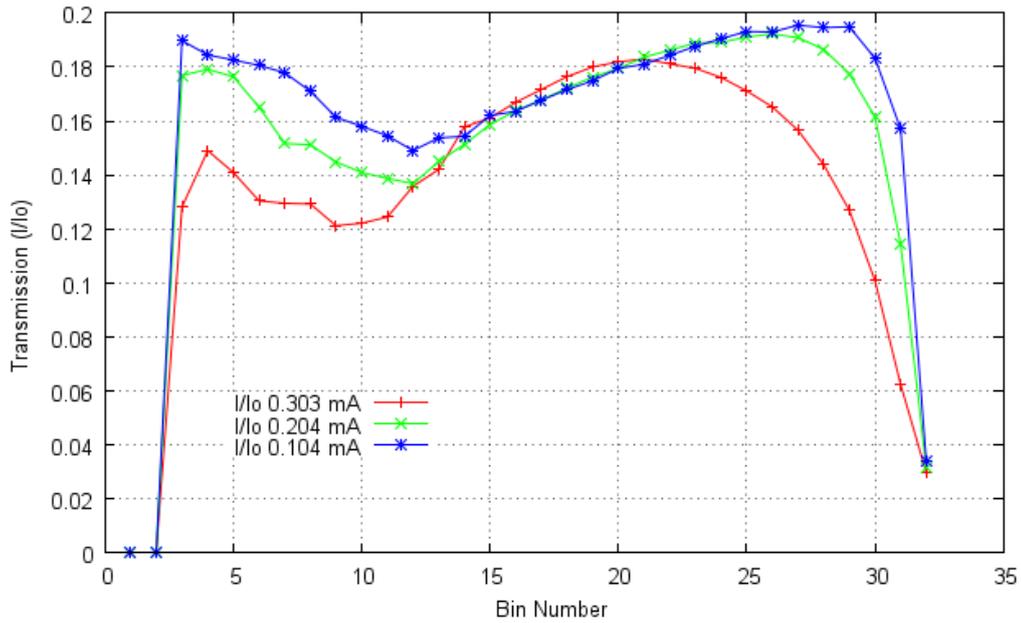
Fig 5-13 Graph showing the change in transmission spectra as a function of beam current for a 100 mm cuvette filled with water. Algorithm 1 was used with a CR-200-50ns shaper.

The problem with this standard method of calculating transmission is that the count rate measured in I must ideally be constrained to a level where the corresponding I_0 measurement is not taken at a count rate where pulse pile up becomes significant. Restricting the count rate by this method has the disadvantage of increasing measurement times. Methods of resolving this issue are discussed in the next section.

125

5.6 Improvements to Transmission Measurements

One of the problems in reducing the count rate such that the I_0 spectrum is not subject to a large amount of pile up is that the I spectrum contains significantly fewer counts and therefore the measurement time must be extended to achieve the same Poisson precision.

One way of avoiding this problem is to reduce the x-ray flux in the I_0 measurement only. This is done by replacing the so called I_0 scan with a new measurement at a lower count rate referred to here as I_c. This lower count rate can be achieved either by inserting an attenuator which is present only during the I_c measurement or alternatively by variation in the x-ray generator beam current. This new ratio, I/I_c, can then be acquired at a favourable rate for the I measurement whilst not resulting in a significant amount of pulse pile up in the I_c measurement. Clearly this new measurement does not give the true transmission spectrum however this does not present a problem to the material identification algorithms, provided that the database entries take the same form.

A 25 mm block of polyether ether ketone (PEEK) was selected for the attenuating material in the I_c measurement due to its radiation hardness. The I_0 and I_c spectra from Algorithm 1 can be seen in Fig 5-14.
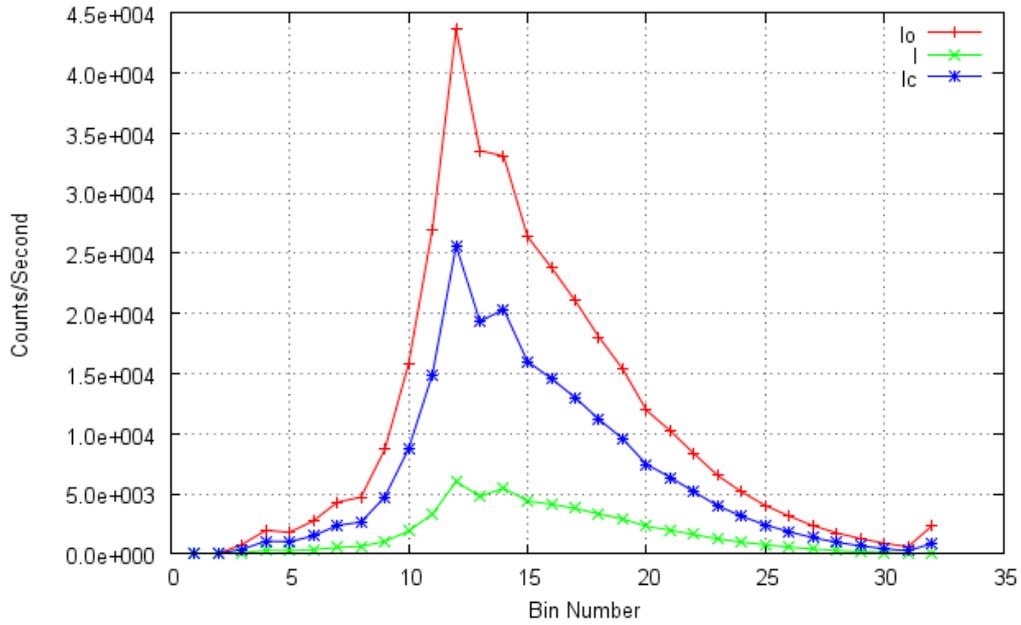
Fig 5-14 Graph showing the I, I_0 and I_c spectra from Algorithm 1 with a beam current of 0.104 mA and a shaping time of 50 ns.

The use of a PEEK block results in more than a 40% reduction in counts compared to that of I_0. The effect of this on the transmission curves can be seen in Fig 5-15. Here the I/I_0 and I/I_c spectra are shown for various beam currents and as can be seen the variability in transmission is reduced by the use of this new ratio.
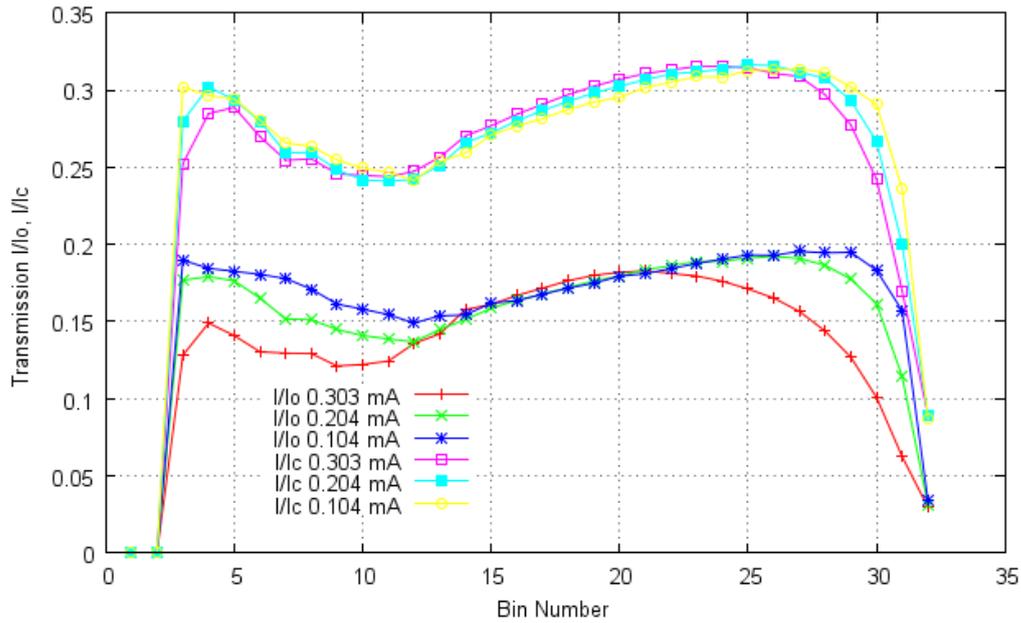
Fig 5-15 I/I_0 and I/I_c measurements of a cuvette of water with a path length of $100\ mm$. Here pulse detection Algorithm 1 is used with a CR-200-50ns shaper.

Reduction in the rollover effect can be achieved by further equalising the count rates in the I and I_c acquisitions. This results in similar amounts of pulse pile up in each spectrum meaning partial normalisation of the effect. This can be seen in Fig 5-16 where the count rate in the I measurement was increased by increasing the beam current to $0.303\ mA$. Here the sum of all spectra have been normalised for comparison purposes.
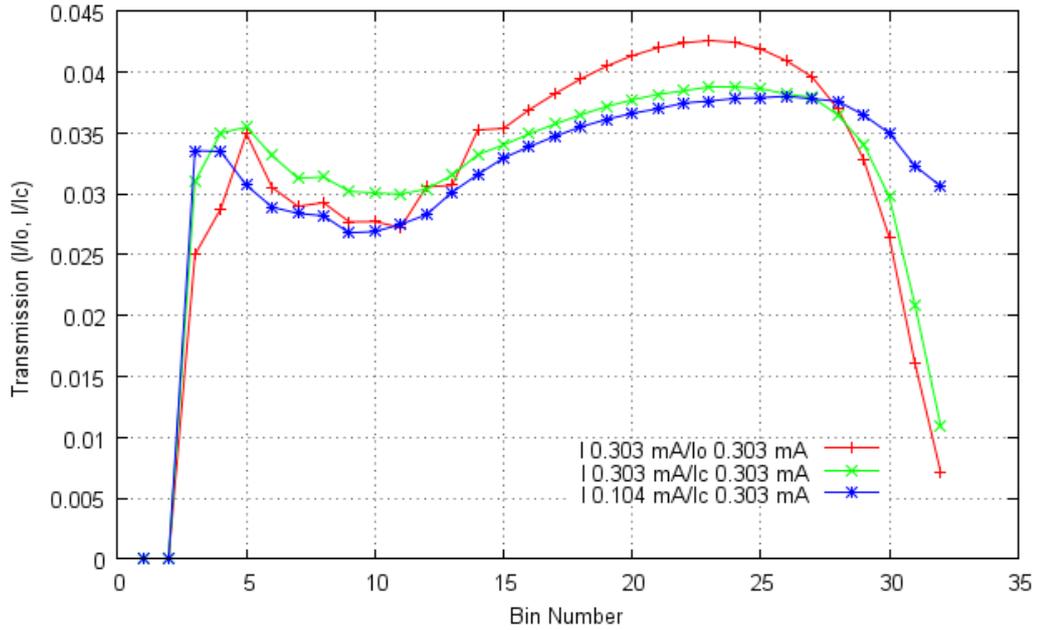
Fig 5-16 Transmission plots under various beam current and normalisation conditions showing the reduction in rollover which occurs when the count rate in the I and I_0 (or I_c) spectra are equalised.

The ratio of the total counts in I/I_0, I/I_c and $I\ 0.104\ mA/I_c\ 0.303\ mA$ are 0.15, 0.26 and 0.79 respectively. As can be seen from Fig 5-16 this rollover is reduced as the ratio approaches unity. This technique could be further optimised by selection of the calibration materials in order to more closely match the count rate in I. This could be done by using multiple thicknesses of calibration block which could be selected according to the path length through the measured bottle.

5.7 Stability Testing

Finally, the other important requirement is that the count rate for a given beam current is stable with time. Fig 5-17 shows the total counts over a series of repeat scans for various beam currents for I_0. Here the cradle is moved into the I_0 position and repeat 5 second acquisitions are taken for each beam current. As can be seen the output is stable over the entire series of scans. The maximum variability for a fixed beam current is a factor of 1.3 greater than the error expected from Poisson statistics.
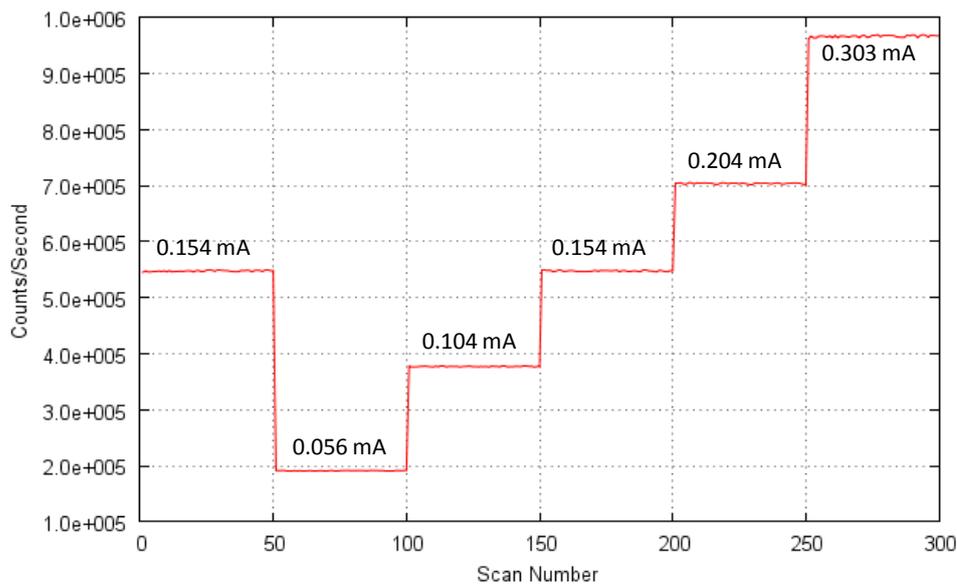
Fig 5-17 Total counts per second across all bins as a function of scan number for various beam currents. Here Algorithm 1 was used with a CR-200-50ns shaper.

5.8   Test of Threat Items

Fig 5-18 shows I/I_c spectra for various threat items[vi] measured on a different system to the one discussed previously. This is shown in order to highlight the fact that small shifts in spectral shape can significantly reduce the system sensitivity to the small differences between liquids. The similarity of liquids is particularly noticeable when compared to the transmission of water (black line) which lies very close to three threat items.
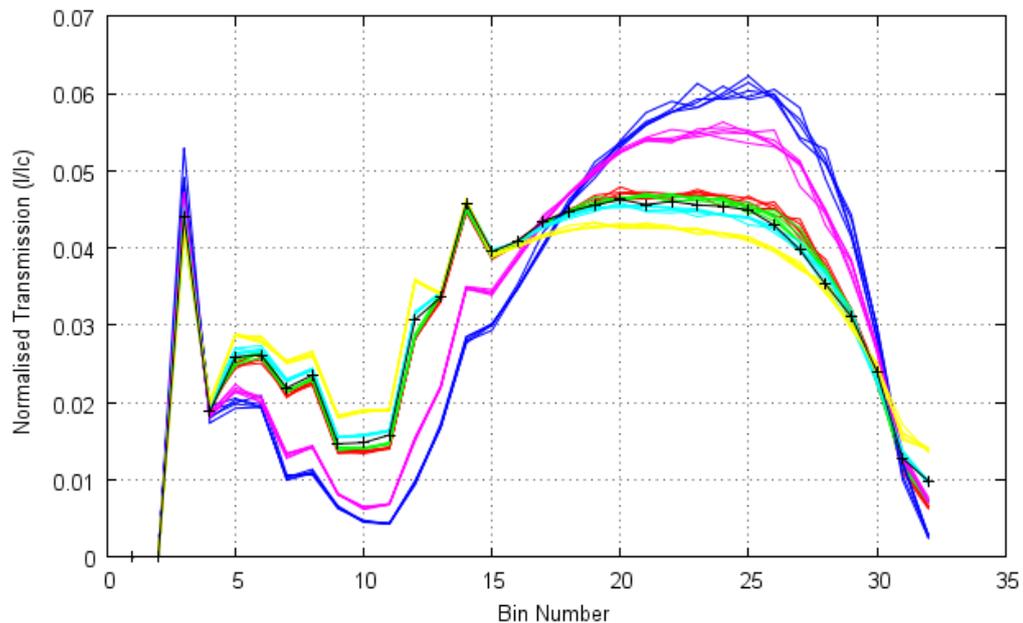
Fig 5-18 Graph showing I/I_c spectra for various threat items in a $100\ mm$ pyrex cuvette. The count rate here was set to $500\ kcps$ for I_c and pulse detection Algorithm 1 was used. The black line is the transmission of water shown for reference [vi].

[vi] Threat items in Fig 5-18 are intentionally not labelled due to confidentiality.

5.9   Conclusion

In this chapter results from experimental testing of Algorithms 1 and 2 were presented using an Amptek XR-100T detector. The algorithms were first coded onto an oscilloscope enabling the code to be emulated prior to implementation on an FPGA. Both the oscilloscope and FPGA versions of the algorithms were shown to be working as expected and exhibited good agreement to the spectrum obtained from a commercially available Canberra Multiport II MCA.

The shaping time was reduced from $100\ ns$ to $50\ ns$ which was shown to lead to a higher throughput of counts for both Algorithms 1 and 2. This however resulted in a degraded spectrum due to ballistic deficit effects arising from the depth of interaction within the detector and was demonstrated by the broadening of the $122.1\ keV$ peak from a ^{57}Co source.

The spectral distortion as a function of count rate was demonstrated using x-rays generated from a tungsten x-ray tube operating at various beam currents. Good agreement was found to the model in Chapter 3 with low energy events piled up and incorrectly assigned to higher energies, resulting in the rotation of the spectrum about bin 19. Algorithm 2 showed a slight reduction in this effect but pile up was shown to still be present.

The pile up in individual I and I_0 spectra was shown to lead to a rollover in the transmission curves produced by both algorithms. This was contrary to the initial understanding, which assumed that the transmission spectrum was a function of the test object only, with all detector and measurement related artefacts normalised out by the transmission measurement. In reality the transmission spectrum acquired on a Bottle Scanner is a convolution of both sample specific information and detector system artefacts.

As pile up is not normalised out by the I/I_0 ratio this makes the system susceptible to rate dependent changes such as detector alignment and beam current instability. This effect was demonstrated to be reduced by changing to an I/I_c measurement where the sample measurement was normalised against a material which more closely matched the transmission of the test object.

The improvement can be seen by a reduction in rollover at high energies and a lower variability in transmission spectra as a function of beam current. The understanding of the effects of pulse pile up on the Bottle Scanner has lead to many changes in data collection and analysis methods, and has resulted in significant improvements to the performance of the system.

Chapter 6   Simulation of Transmission Spectra

6.1   Introduction

As seen in the previous chapter the transmission spectra produced by either I/I_0 or I/I_c show a rollover at high energies. This behaviour is observed using both Algorithms 1 and 2 and has been shown to be due to pulse pile up effects which are not normalised out by the calculation of transmission spectra. In addition to this, measurements using a ^{57}Co source show a significant amount of hole tailing when the selection of a $50\,ns$ shaping time is made. This depth of interaction effect arises from x-rays interacting deep inside the CdTe.

This is compounded by beam hardening which results in a higher average energy in the I spectrum compared to that of the I_0 spectrum due to absorption of low energy x-rays by the intervening bottle. This leads to a greater average depth of interaction in the I measurement making it more susceptible to depth of interaction effects than the I_0 measurement.

135

In this chapter further developments to the modelling work presented in Chapter 4 are discussed. This work has been carried out using the Geant4 software package and allows the interaction of x-rays within the Bottle Scanner to be simulated allowing transmission spectra from bottles to be produced. Also discussed is the addition of more accurate preamplifier and shaping amplifier simulations through knowledge of the depth of interaction of photons within the detector given by Geant4. This has led to validation of the experimental work discussed in the previous chapter and confirms the theory that the rollover effect observed in transmission is driven by pulse pile up.

The work presented in this chapter also allows more sophisticated algorithm development which is discussed in Chapter 7.

6.2   Geant4 Model of the Bottle Scanner System

In this section the details of a Geant4 model of the Bottle Scanner are discussed. The motivation for the development of this modelling environment over that discussed in Chapter 3 is to simulate the true output of the Bottle Scanner. Whilst the model in Chapter 3 is useful for the purposes of algorithm development, the absence of x-ray interaction effects and detector effects prevents true I and I_0 spectra from being produced.

The Geant4 software was initially developed by collaboration under the leadership of CERN[75] and is used in applications such as particle physics, medical physics, accelerator design and space engineering [76]. The software models the full range of scattering and absorption effects and allows each photon or secondary particle to be traced until it is either absorbed, its energy drops below a threshold value or it escapes the modelled world volume. The two main reference papers for Geant4 are [75] and [77] which give a full background to the software and it's development.

The Geant4 model of the Bottle Scanner system was developed collaboratively with M. Taylor and J. Allison[78]. The model includes interaction effects with the bottle under test, the CdTe detector, and the Bottle Scanner chamber. This allows the transmission spectra from various liquids to be simulated. This increased level of realism allows a range of effects to be explored such as the effect of collimator geometries, chemical composition of liquids and container types etc.

137

For the purposes of this work the output of most interest is the energy and depth of interaction of x-rays within the detector.

6.2.1 The Geant4 Model

The modelled world volume in Geant4 is the Bottle Scanner chamber which consists of an exit collimator, bottle carriage, bottle and detector. Fig 6-1 shows a graphical illustration of the model, where the green lines represent the simulated trajectories of x-rays. The geometrical volumes used to create this model are composed of a range of simple 3D shapes and the elemental composition of each component is defined in a materials database. The software then calculates the properties that are necessary to describe the interaction of particles within each volume of material.
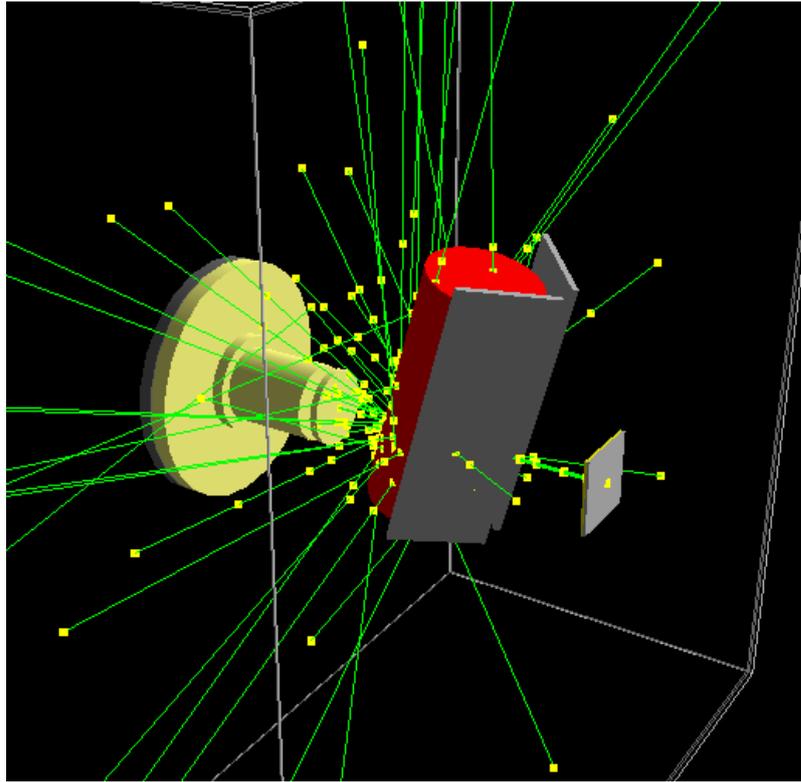
Fig 6-1 Diagram of the geometry modelled in Geant4 showing the x-ray source collimator, bottle presentation in the beam path and the detector. The green lines trace the trajectories of transmitted and scattered x-rays.

Each event in the Geant4 model starts with a single x-ray fired from the source towards the detectors in a narrow pencil beam. The x-ray is tracked through the volumes which it encounters using random numbers in order to determine whether it interacts and if so by which type of interaction. Only the statistically significant interactions in the 0 to 160 keV energy range are considered. These are: Compton scattering and photoelectric absorption [18]. At the point of x-ray interaction the x-ray disappears and is replaced by the interaction products with their energy and direction drawn randomly from the appropriate distributions. The new particles are then traced through volumes in the same way.

Since the system works at low energy the only particles that can be produced are more photons or electrons [79]. Electrons interact quasi-continuously with the intervening material, depositing energy and continually changing direction due to multiple Coulomb scattering. As such, electrons are tracked in much smaller steps than photons. The particle tracking continues until all particle energies have fallen below threshold or they have escaped the world volume.

The energy deposited in the CdTe detector is the event output of most interest for this work. Also recorded for each event is the position and type of the x-ray interaction. Very large numbers of events are simulated to build up a detailed high precision picture of the response of the Bottle Scanner. The results shown in the following sections were run on a farm of 14 computers. As the x-ray emission process is entirely random this allows simulations to be processed in parallel on multiple computers thereby reducing CPU time.

6.3   Modelling of the Detector Response

Whilst the Geant4 simulation allows the energy and position of the interaction of x-rays with the detector to be simulated it does not allow simulation of the signals produced by the detector, preamplifier or shaping amplifier. In addition to this the Geant4 model does not simulate the time of arrival of x-rays at the detector therefore pulse pile up effects cannot be explored directly.

The time of arrival was simulated by use of the model discussed in Chapter 4. This is done by taking the output file from Geant4 which is comprised of energy and location information for each x-ray event and applying the simulation of the random time of arrival of each x-ray. In addition to this the detector response was simulated through knowledge of the depth of interaction of the incident x-ray beam. This is done by simulation of the charge transients using Equation 2-14.

In order to improve the efficiency of the model a simplification was made to the calculation of charge transients. Instead of calculating a unique transient for every interacting photon, the detector volume was split into 20 artificial slices each relating to a $50 \, \mu m$ cross section of the detector. The charge transients were then calculated for each of the 20 segments with $1 \, ns$ resolution and stored in a lookup table. A uniform electric field was assumed and the field was set to $1000 \, V cm^{-1}$ in order to maintain approximate agreement to the rise times measured from the XR-100T detector. The charge transients for a selection of interaction depths are shown in Fig 6-2.
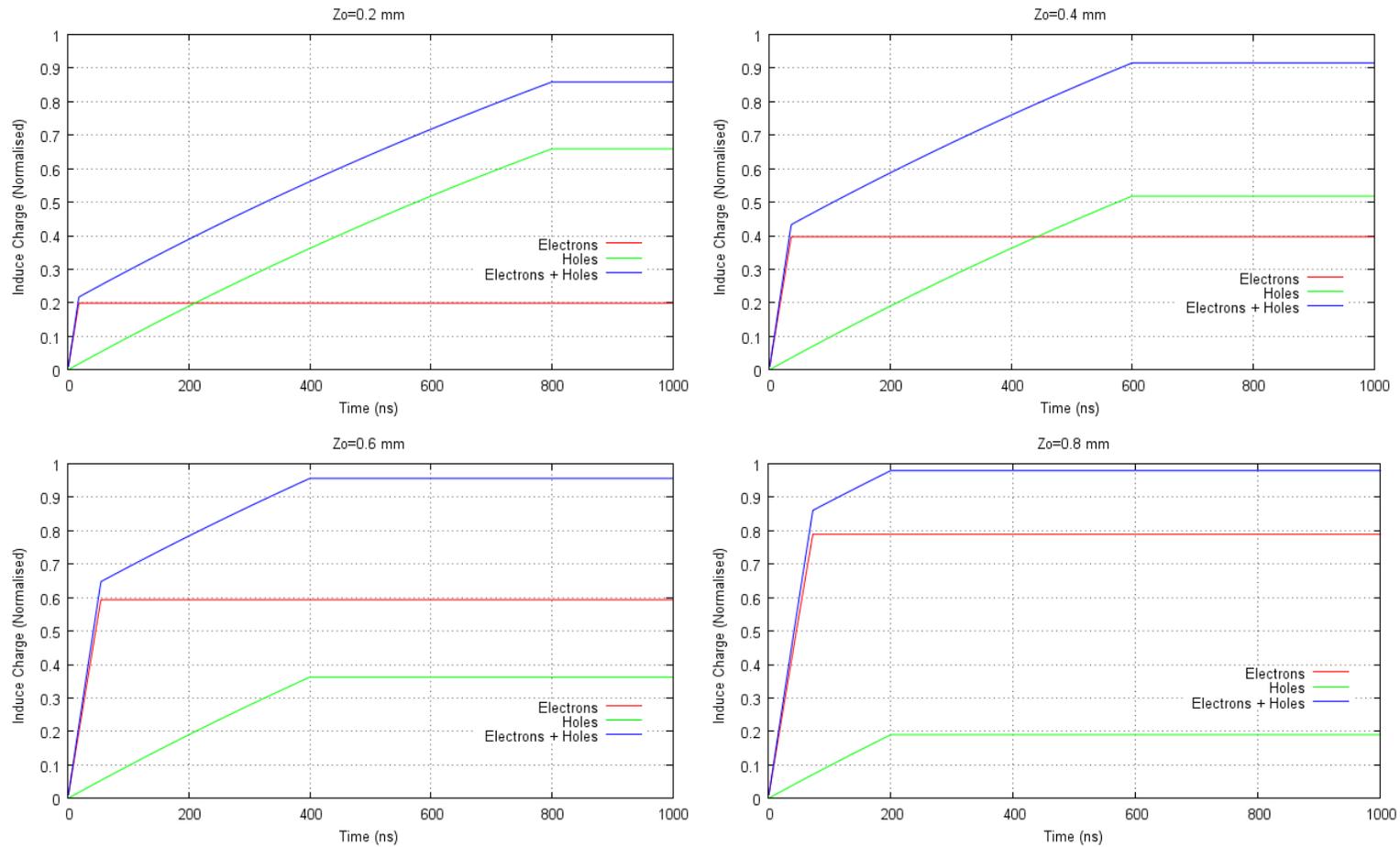
Fig 6-2 Simulation of charge transients for various depths of interaction within a $1\ mm$ thick CdTe detector. Here a uniform electric field of 1000 Vcm^{-1} assumed and a mobility lifetime product for electrons and holes of 3×10^{-3} and $2\times10^{-4}\ cm^2V^{-1}$ respectively. Here Z_0 refers to the depth of x-ray interaction measured with respect to the cathode.

142

The amplitude of each charge transient is calculated from the number of electron hole pairs ionised in the interaction. This is given by Equation 2-3 with the addition of a random fluctuation to account for the Fano factor. Fluctuations due toelectronic noise are not currently included in the model. The charge transients shown in Fig 6-2 are then scaled by the preamplifier gain.

Fig 6-3 shows the shaping amplifier output for the fast and slow preamplifier pulses from the XR-100T detector and a CR-200-50ns shaper. These pulses are due to emissions from a ^{57}Co source and therefore the energies of the incident gamma rays in the left and right of the figure are not necessarily equal. The pulse on the right of the figure has a wider base width which is due to the slow rise time of the preamplifier signal. This is likely to be due to an interaction far from the cathode resulting in a signal predominantly induced by the drift of the holes towards the cathode.
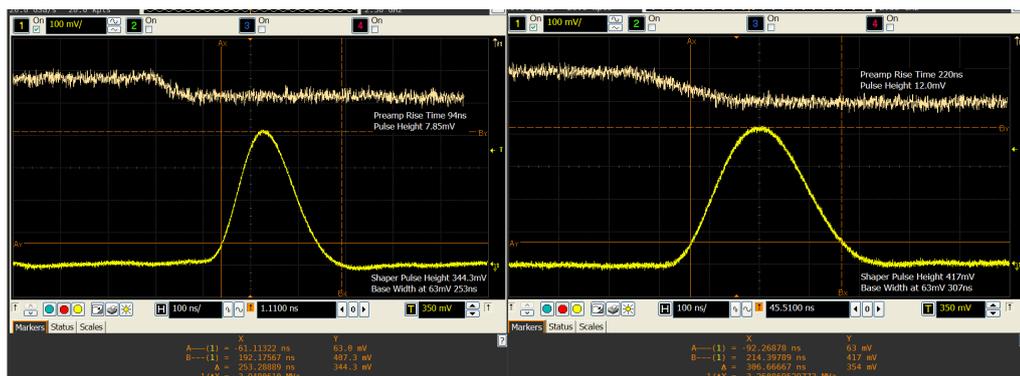

Fig 6-3 Oscilloscope traces from fast (left) and slow (right) preamplifier signals from an XR-100T detector. The corresponding shaping amplifier signals show varying widths due to the difference in rise time between the two preamplifier signals.

Equation 2-14 is not directly applicable to the calculation of the shaping amplifier output as the preamplifier signals do not have instantaneous rise times. Instead it is assumed that the preamplifier signals are composed of a series of 1 *ns* steps. The shaping amplifier signal is then calculated by repeatedly applying Equation 2-14 to every 1 *ns* rise of the preamplifier signal and summing each of the signals together. This method was applied to the preamplifier signals from Fig 6-3 and a comparison between the experimental and simulated shaped outputs is shown in Fig 6-4.
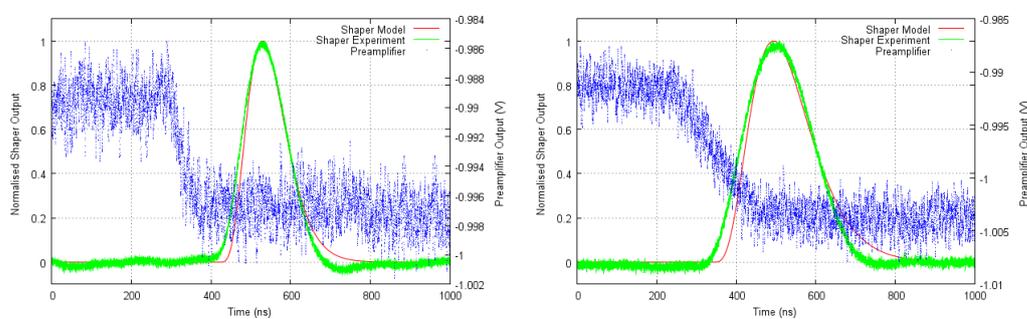

Fig 6-4 Experimental and modelled shaping amplifier output from fast (left) and slow (right) preamplifier signals.

This treatment is important as the width of the shaped pulse is proportional to the rise time of the preamplifier signal and therefore results in pulses with variable probabilities of pile up depending upon the depth of x-ray interaction within the detector. This leads to some interesting effects which are discussed in Chapter 7.

6.4   Simulations of Transmission Spectra

The I and I_0 spectra were simulated for a $1000\,ml$ polyethylene terephthalate (PET) bottle of water using Geant4. Each event was then tagged with a random time of arrival at the detector and the corresponding shaping amplifier signals were calculated as described above using the depth of interaction information given by the Geant4 simulation.

The simulated transmission spectrum is shown in Fig 6-5 (top) with a count rate incident on the detector of 1 count per second i.e. no pile up is present. Fig 6-5 (bottom) shows the same simulation at a detected count rate of $500\,kcps$. At low count rates the transmission curve shows an increase as a function of energy. At high count rates the transmission curve shows a rollover due to pulse pile up as observed experimentally in Chapter 5.
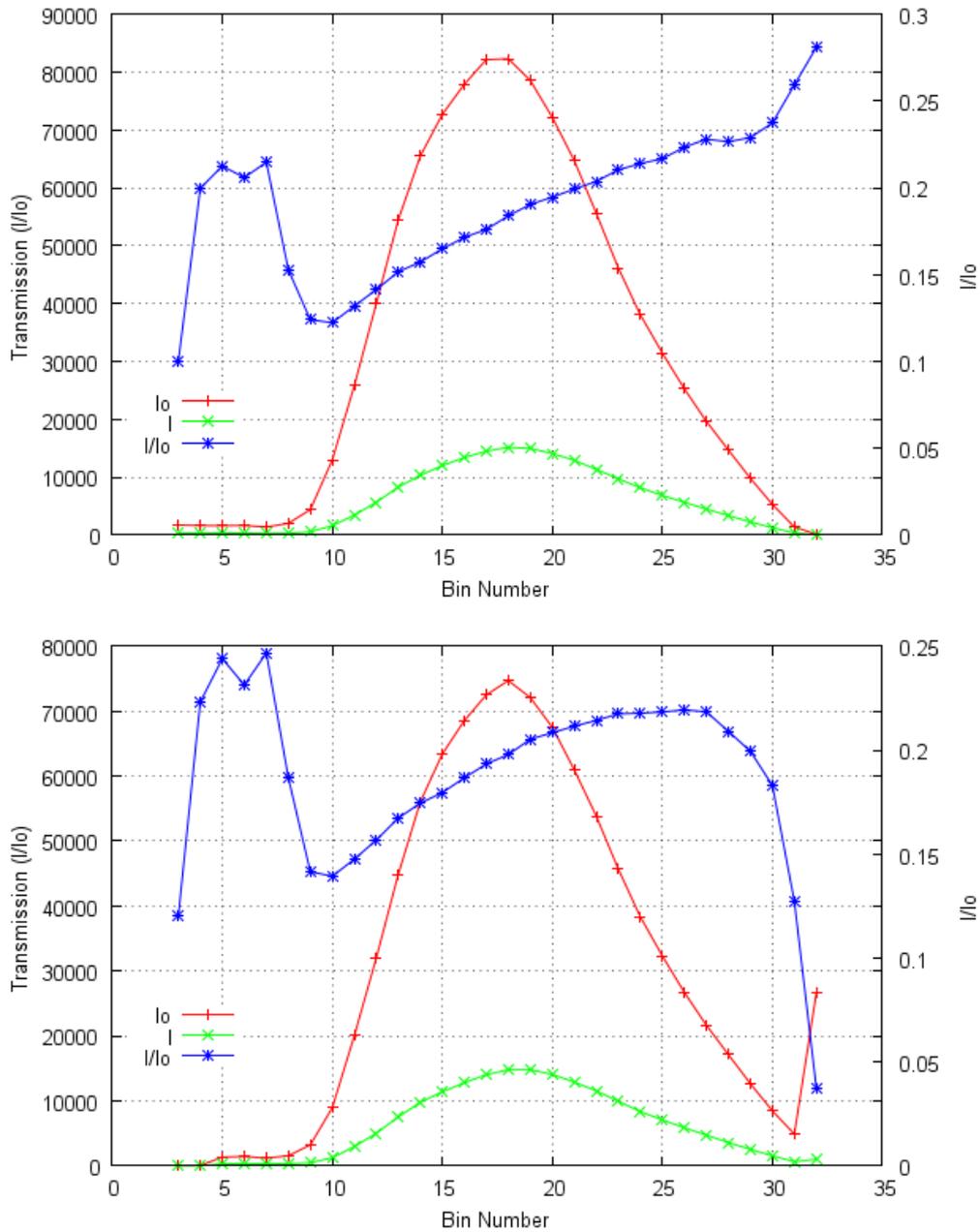
Fig 6-5 Simulated *I*, *I$_0$* and *I/I$_0$* spectra for a 1000 *ml* bottle of water. The graph at the top of the figure shows a low count rate simulation at 1 *cps* and the graph at the bottom of the figure shows a simulation at 500 *kcps*.

Fig 6-6 shows the same modelled transmission spectrum from Fig 6-5 at a count rate of 500 *kcps* along with a spectrum acquired from a Bottle Scanner under the same conditions.
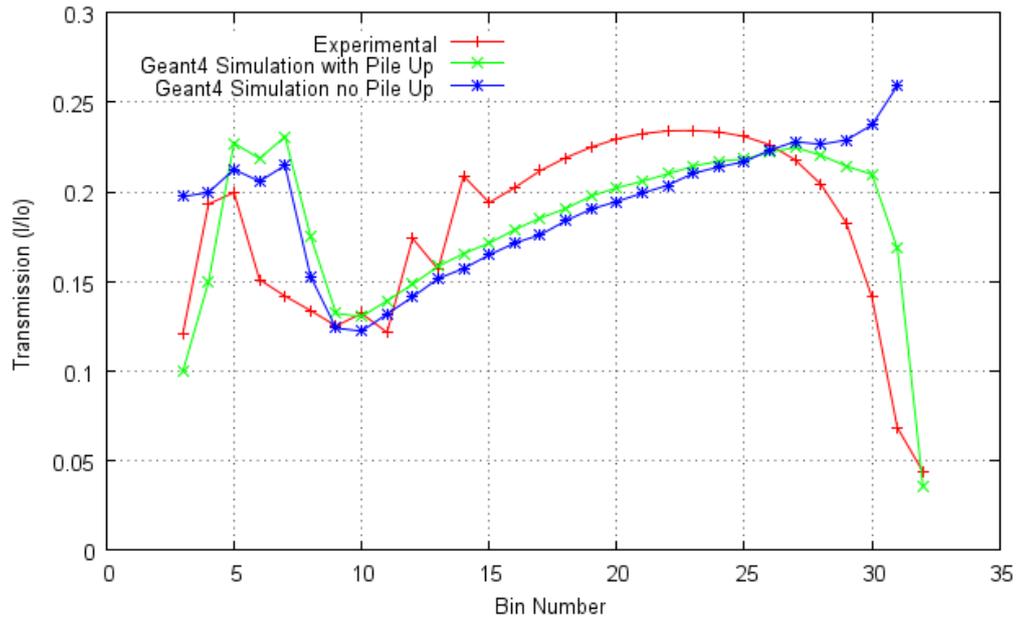
Fig 6-6 Graph showing the transmission spectra from an *I/I₀* measurement of a $1000\,ml$ PET bottle of water. The experimental data was collected by use of the FPGA implementation of Algorithm 2. The modelled transmissions are from a simulation with and without pulse pile up consideration.

As can be seen the model shows an overall agreement to the measured spectrum when pulse pile up is added. The variation between the experimental and modelled spectra is thought to be due to an incomplete description of the detector response. Aside from these discrepancies the overall behaviour of the experimental system and model are in agreement.

6.5   Conclusion

In this chapter the further development to the model discussed in Chapter 3 has been presented. The addition of a Geant4 model has allowed information relating to the x-ray interactions with materials in the beam path (such as bottles) to be simulated. Also the energy and depth of interaction of each x-ray within the detector is returned allowing an improved simulation of the output of the detector and electronics.

The preamplifier signal has been calculated by splitting the detector in to $50\ \mu m$ segments and calculating the charge transient for x-rays depositing energy in each of these regions. This has then allowed the shaping amplifier signal to be modified in order to account for the finite rise time of the preamplifier signal.

The transmission spectrum was then calculated using a $1000\ ml$ PET bottle of water. This was compared to the transmission spectrum from a Bottle Scanner. The general shapes of both the modelled and real transmission spectra show agreement, with the characteristic rollover at high energy. Simulation at a low count rate has proven this rollover to be a count rate driven effect, as previously suggested in Chapter 5.

Whilst there is not complete agreement between the real and simulated transmission, the use of this modelling has allowed the pile up effect to be

explored in a way which is not possible using the current Bottle Scanner system due to the beam current limitations imposed by the x-ray generator.

Further work in the form of improvements to this model is planned in order to more accurately simulate the preamplifier and shaping amplifier response to better match the simulated and real transmission spectra.

Chapter 7   Height-Width Filtering

In this chapter a height-width (HW) filtering method is discussed which was developed in order to correct the depth of interaction effects observed at short shaping times, and to remove piled up pulses from the pulse height spectrum. This work was carried out using a combination of experimental measurements taken using a Bottle Scanner and simulations using the models discussed in Chapters 4 and 6.

The experimental measurements were taken using an oscilloscope with the addition of data acquisition and control software written in Matlab for this application. The data from this software along with simulation data has enabled the development of a new algorithm which is shown to deal with the problem of ballistic deficit produced by short shaping time selection, allowing the detector resolution to be regained whilst maintaining the high count rate/low pile up advantages of a short shaping time. The method proposed here also offers a way of removing a larger fraction of piled up pulses and, as will be shown, leads to a transmission spectrum which more closely matches the underlying physics.

151

The algorithm has been developed with the limitations of the target FPGA in mind and results are shown for the initial implementation of the algorithm on a Cyclone II FPGA.

Also shown are the results of simulations for transmission spectra calculated at various input count rates with varying degrees of pulse pile up treatment, including complete removal of pulse pile up via knowledge of the Monte Carlo truth, removal via the HW filtering method and no pile up removal. This provides a relative measure of the stability of the transmission spectra for a variable input count rate and informs the direction of further algorithm development.

7.1 Identifying Partially Collected Events

As previously shown in Fig 6-3 the shaping amplifier output for the slow preamplifier pulses exhibits a wider base width. Ballistic deficit can occur for such pulses where the preamplifier pulse has not reached its maximum value within the peaking time of the shaping amplifier. In these cases the proportionality between pulse height and energy is not maintained, which potentially results in the incorrect bin assignment of the event. As incorrect assignment is always to a lower bin this leads to the familiar hole tailing effect observed in Fig 5-5.

The base width, W of such a pulse above a given threshold can be defined as:

$$W = t_2 - t_1 \qquad \text{7-1}$$

where t_1 and t_2 are the times of intersection of the pulse with the threshold, defined here as $63\ mV$.

This parameter can then be used to define whether height/energy proportionality is maintained. A filter can be applied such that pulses where W is greater than a predefined value are either discarded or corrected.

As W is a function of the height of the pulse the discard criteria must be set in order to take this into account. An illustration of this is shown in Fig 7-1 where

the shaping time is $50\ ns$. A lookup table of pulse width as a function of pulse height can then be generated either by empirical inspection of pulses on an oscilloscope or by a functional relationship based on the response of the CR-RC network to a step function.
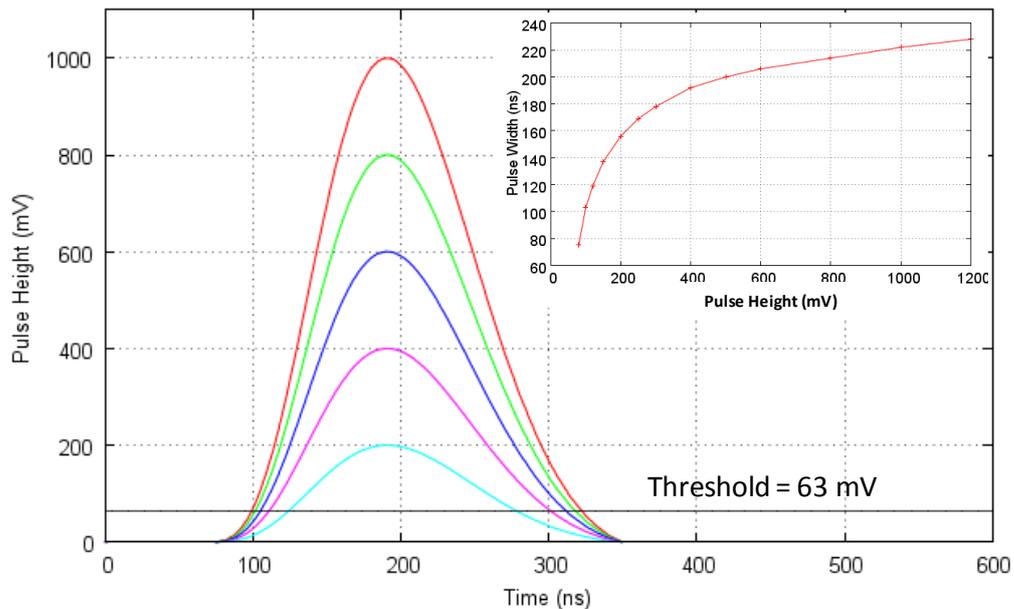

Fig 7-1 Simulation of the CR-RC network of the CR-200-50ns shaping amplifier at different amplitudes between 0 and $1\ V$. As can be seen the base width at the $63\ mV$ threshold increases with pulse height. The relationship between pulse width and pulse height is shown in the inlayed figure.

The inlay in Fig 7-1 shows a plot of W as a function of pulse height, H from data captured on an oscilloscope using a Keithley 3390 pulse generator with a rise time of $10\ ns$. Here it can be seen that larger pulses have wider base widths at the $63\ mV$ threshold, meaning that any filter must include a variable acceptance criteria in order to accommodate the full range of pulses i.e. any width based filtering must also take into consideration the pulse height prior to making a decision whether to delete or correct a pulse. This is referred to as the minimum HW curve.

154

Assuming the performance of the detector is limited only by the sweep-out time of the charges and not by charge collection efficiency, the occurrence of a ballistic deficit affected event implies that the photon interaction position, z, from the cathode is greater than the distance which can be traversed by the holes during the peaking time of the shaping amplifier.

This leads to a maximum interaction depth, z^* measured from the cathode contact on the detector. Interactions between $z = 0$ and $z = z^*$ will result in collection of the entire electron and hole signal within t_p. Interactions between $z = z^*$ and $z = d$ will result in some loss in hole signal. This is illustrated in Fig 7-2.
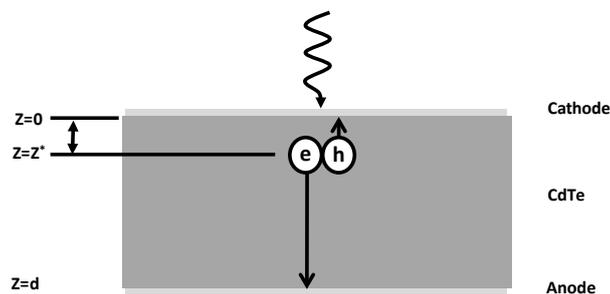

Fig 7-2 Diagram showing the creation of an electron-hole pair at a distance z^* from the cathode. Interactions at $z > z^*$ suffer ballistic deficit effects due to the longer collection time of the hole signal.

The maximum depth of interaction, z^* with respect to the cathode can be written in terms of the hole velocity and the peaking time of the shaping amplifier:

$$z^* = v_h t_p \tag{7-2}$$

Expression 7-2 therefore states that any interaction at a depth of greater than z^* will not be fully collected in time t_p. Rewriting Equation 7-2 in terms of hole mobility shows the bias dependence of the maximum interaction position.

$$z^* = \frac{\mu_h V}{d} t_p \qquad\qquad 7\text{-}3$$

Higher bias voltages result in a larger value of z^* due to the greater hole velocity, however bias voltage is limited by leakage current and break down of the Schottky diode in the case of the XR-100T detector.

Like ballistic deficit, charge trapping also results in loss of pulse height/energy proportionality as the probability of charge trapping increases with the drift length of the hole signal to the cathode. For this reason distortion of the shaping amplifier pulse height due to ballistic deficit and charge trapping effects are convoluted, and collectively contribute to form the continuum of pulse height distortion which leads to hole tailing. As such these are collectively referred to here as depth of interaction effects. The measurement of parameters H and W allow such events to be identified and as will be seen they can be corrected via a depth of interaction correction or removed from the spectrum all together.

7.1.1   Correction of Depth of Interaction and Pulse Pile up Effects

Simple removal of incompletely collected events would not only be disadvantageous due to the reduction in the throughput of counts, but would also result in a filter which does not apply uniformly to the entire spectrum. The mean

interaction distance from the cathode is dependent on the photon energy and this correction would therefore result in preferential suppression of high energy events. In addition to this both I and I_0 spectra would be affected in different ways due to the variation in beam hardening. This situation is analogous to that of a thin detector with low detection efficiency at high photon energies. It is for this reason that an energy correction method rather than a simple filtering method represents the most desirable solution.

In order to reassign those pulses which are affected by depth of interaction effects they must first be distinguished from those which have larger than expected base widths due to pulse pile up. It would not be beneficial to reassign a piled up pulse back into the spectrum as clearly both the energy and number of such pulses cannot be accurately determined. It will be shown in Section 7.3 that reassignment of certain piled up events is unavoidable, however this should be minimised where possible.

The treatment of each class of distorted pulses separately ensures that where distinguishable, piled up pulses are not added back into the spectrum. This method will be introduced by use of HW scatter plots of shaping amplifier pulses under various conditions.

HW acquisition software was written in Matlab in order to produce the HW plots shown in this section. The events are captured as in Chapter 5 by using a

DSO90254A oscilloscope set to a sampling frequency of $200\ MHz$ with a trigger level of $63\ mV$. The software contains the basic pulse height detection common to all algorithms with the addition of some instrument control code and a measurement of the time that the signal remains above the $63\ mV$ threshold. The output from this program is the H (units of volts or bins) and W (units of seconds or samples) parameters for each pulse, which can then be used to form a HW scatter plot. In order to achieve reasonable counting statistics 100,000 events were collected for all experimental data shown here.

Fig 7-3 shows a HW scatter plot from detection of the 0 to $160\ keV$ bremsstrahlung continuum emitted by a tungsten x-ray tube at a detected count rate of $500\ kcps$ in I_c and a beam current of $0.2\ mA$. Here the detector bias was $600\ V$ and the shaping amplifier used was a CR-200-50ns. From Fig 7-3 it can be seen that the lower edge of the plot represents the minimum width for a pulse of a given height and refers to the ideal case from the inlay in Fig 7-1. Pulses lying along this line or very close to it have HW relationships which indicate complete collection of both the electron and hole signal i.e. interactions within a depth of 0 to z^*.
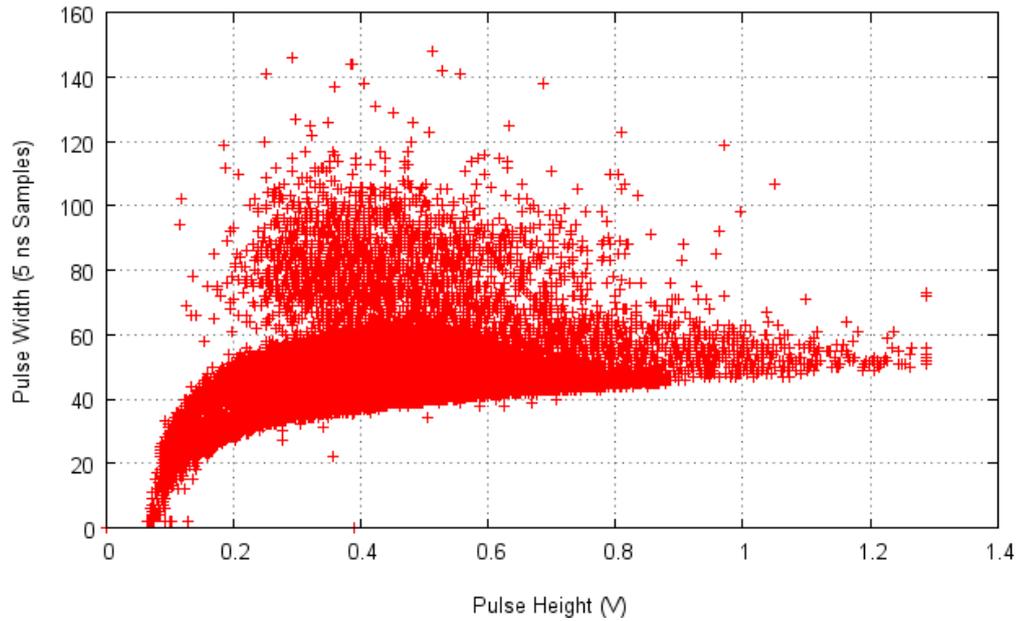
Fig 7-3 HW plot from an XR-100T detector for 100,000 events using the 0 to 160 keV bremsstrahlung continuum from a tungsten x-ray tube. Here the detector bias voltage was 600 V and the shaping time was 50 ns. Data was collected using a DSO90254A oscilloscope with a custom designed Matlab acquisition and control program.

Above this region there are two further types of pulse. The first, lying just above the minimum HW curve, are pulses generated from interactions at positions greater than z^*. The density of this 'lozenge' shaped region arises from the fact that there is a unique relationship between the width and height of such pulses i.e. pulses with greater than minimum widths will have less than minimum heights in a correlated manner.

The region beyond this lozenge shape is less densely populated and arises from pulse pile up. Such piled up pulses have incorrect heights and widths which arise from the interaction of two pulses in a way that is completely random. The height and width of such convoluted pulses are completely uncorrelated and as a

consequence the scatter in this region is random and density fluctuations are expected to obey Poisson statistics.

Proof that the deviations from the minimum HW curve in these two regions are due to differing mechanisms can be seen by repeating the measurement at a lower input count rate. This was done by using a low activity ^{57}Co source with a count rate of around 100 counts per second which results in a largely pile up free measurement regime.
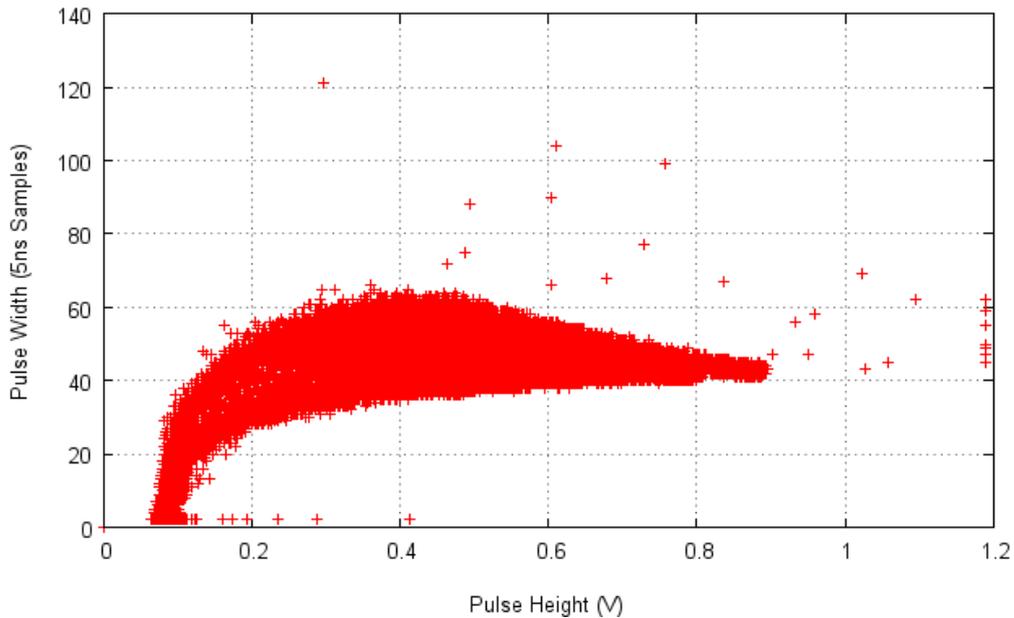

Fig 7-4 HW plot from a XR-100T detector for 100,000 events using a low count rate ^{57}Co source in order to achieve a near pile up free measurement regime. Here the detector bias was $600\ V$ and the shaping time was $50\ ns$.

As can be seen from Fig 7-4 there is a dense lozenge shape which remains despite the lower count rate. The lozenge only extends to $0.85\ V$ due to the lower photon energies emitted by the ^{57}Co source ($136\ keV = 0.85\ V$ since $160\ keV = 1\ V$). As this shape is insensitive to count rate, appearing in both the high count

rate x-ray measurement shown in Fig 7-3 and the low count rate gamma ray measurements in Fig 7-4 this indicates that the lozenge shape is a function of the detector properties and not the input count rate.

The structure of the lozenge is determined by depth of interaction effects, namely ballistic deficit and incomplete charge collection which effect charges generated far from the cathode. The fine structure of the lozenge can be seen more clearly in Fig 7-5 where the HW plots for both ^{57}Co and ^{241}Am are shown as both surface plots and coloured density plots. Here the z axis reflects the number of counts in a given region.

In order to generate such density information it was necessary to bin the HW data, the bin sizes were chosen to reflect the sampling rate and voltage resolution of the FPGA. Pulse heights are therefore represented as bins 1-32 and pulse widths are represented as multiples of 5 ns samples. Greater resolution is easily available via the oscilloscope although this is not currently implementable on the Cyclone II FPGA used in this work.
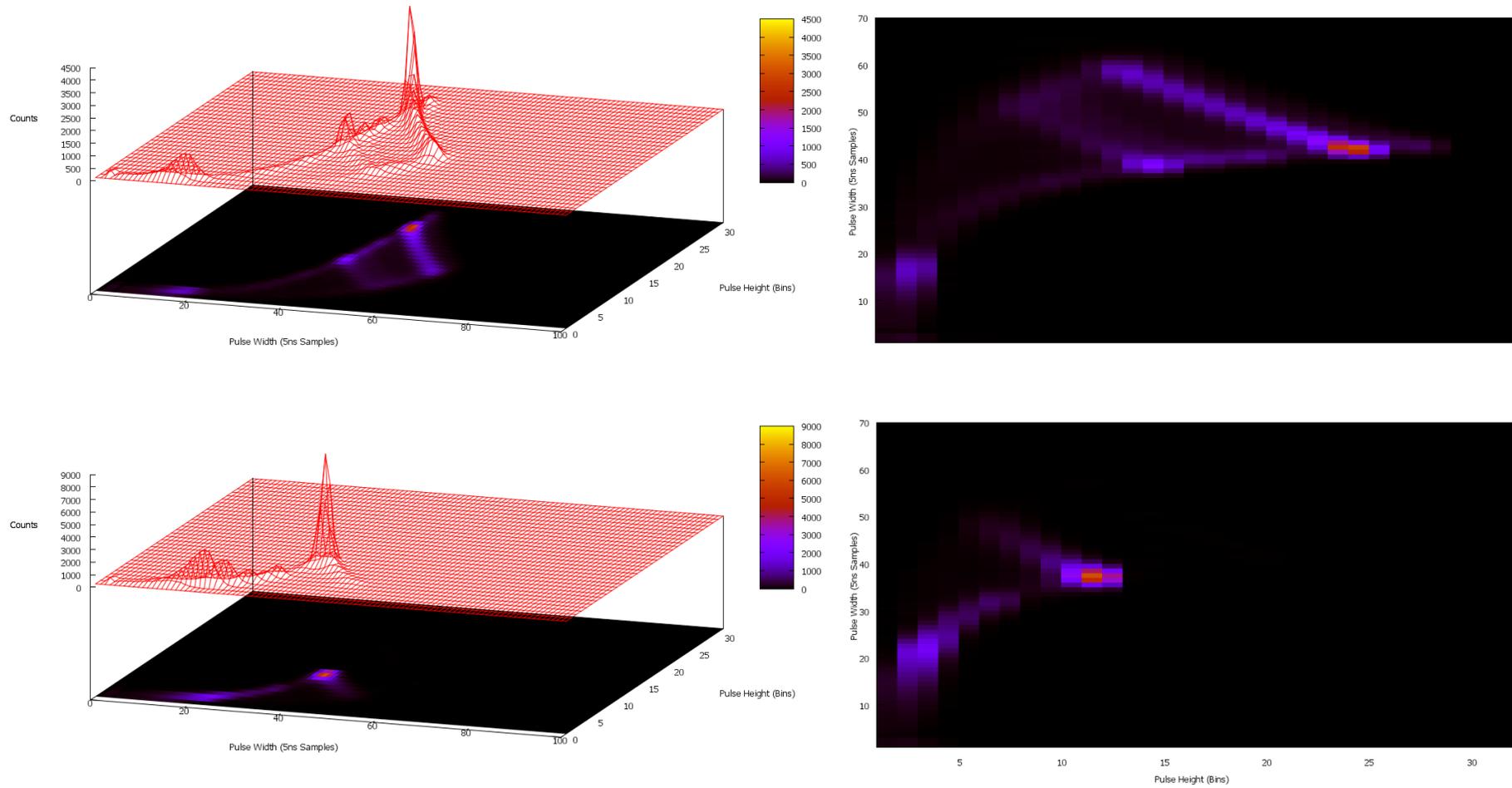
Fig 7-5 Three dimensional HW surface plots for ^{57}Co (top left) and ^{241}Am (bottom left) with corresponding density plots. 100,000 events were collected using a DSO90254A oscilloscope and Matlab analysis software. The main peaks are at 122.1 keV for ^{57}Co and .59.5 keV for ^{241}Am.

162

As can be seen from Fig 7-5 the height width plots for both ^{57}Co and ^{241}Am show clear fine structure. The most noticeable structures are the tails which emanate from the 59.5 keV and 122.1 keV lines. Other tails can be observed in the ^{57}Co plot which emanate from the fluorescence peak of the lead source holder and the cadmium and tellurium escape peaks. Also visible on this figure is the clear lozenge shape which encompasses the entire range of events from those with ideal HW characteristics to those which are highly distorted by depth of interaction effects.

Proof that the origin of the lozenge is due to depth of interaction effects can be seen by varying the shaping time and detector bias. Both larger shaping times and higher bias voltages should result in reduced tailing resulting in a smaller lozenge shape. The outer edge of the lozenge should therefore be expected to collapse down towards the ideal HW curve with increasing shaping time and detector bias.

Fig 7-6 shows the HW plots for shaping times of 50 ns and 100 ns. Results from acquisitions with a ^{241}Am source are shown here as the effect is more clearly observable due to the presence of only a single emission line. As can be seen the 59.5 keV tail is reduced by increasing the shaping time, a result which is expected from a depth of interaction driven effect.
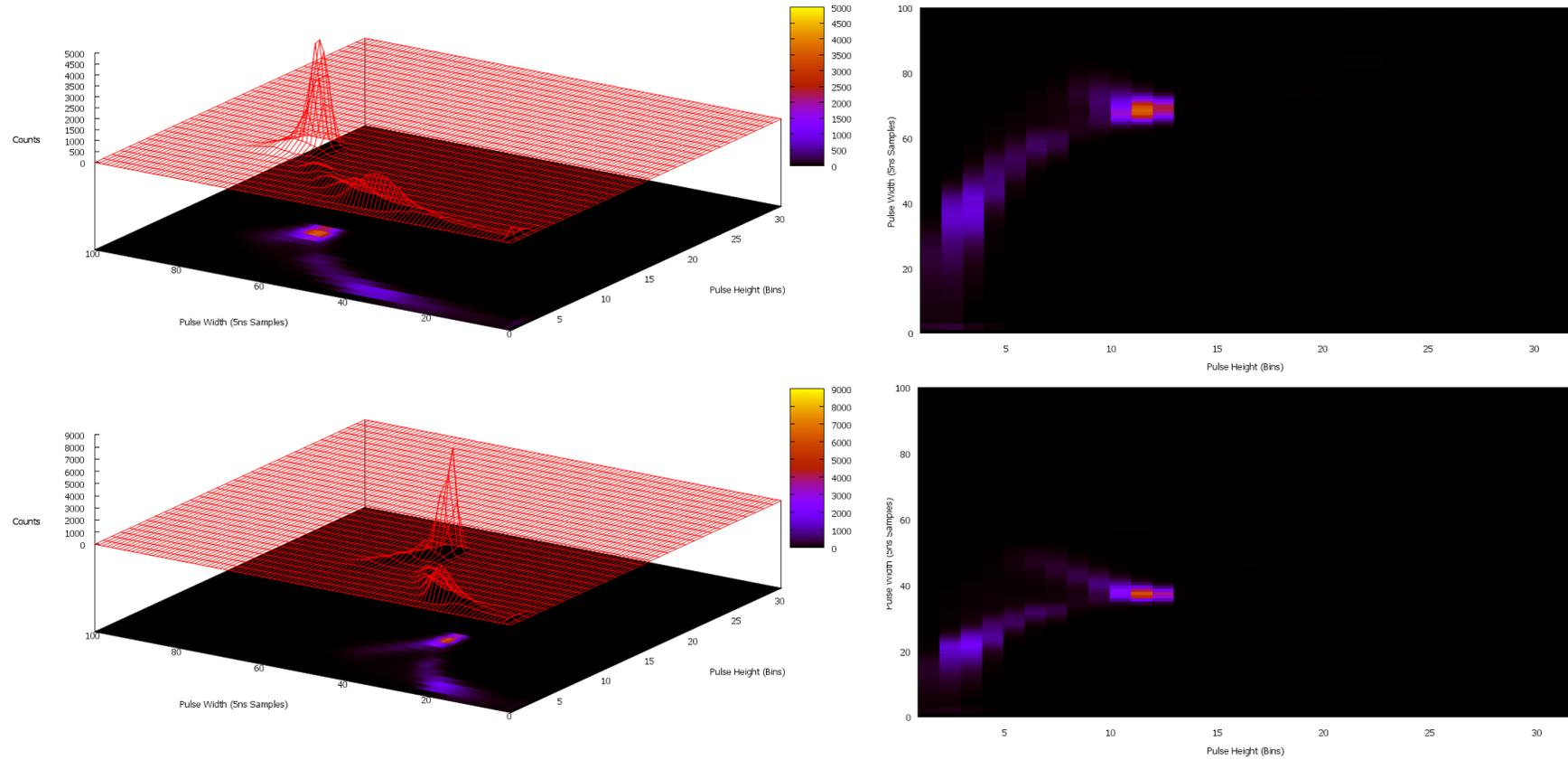
Fig 7-6 HW plots for 100,000 events with shaping times of 100 ns (top) and 50 ns (bottom) for a ^{241}Am source. The main peak is at 59.5 keV.

164

Fig 7-7 shows the effect of bias voltage on the 59.5 keV tail. As can be seen the tail increases as the bias voltage is decreased, which is also consistent with a depth of interaction effect due to ballistic deficit and CCE. The tail is convolved with the 59.5 keV peak and can be seen to disappear into the main peak with increasing bias voltage or shaping time.
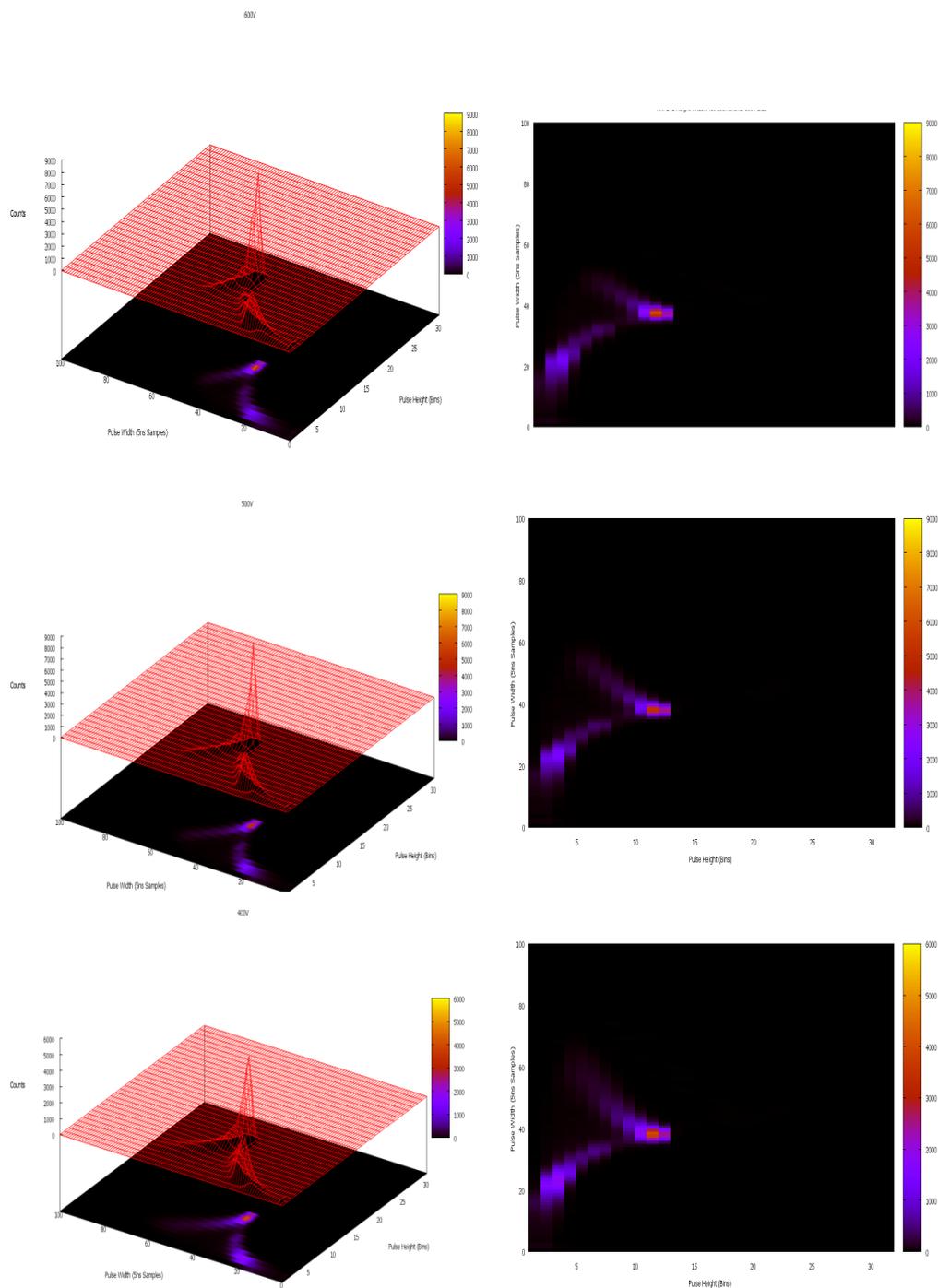
Fig 7-7 Three dimensional HW plots for 100,000 events using an ^{241}Am source with a shaping time of 50 ns. Here the acquisitions were carried out for different detector biases of 600 V (top), 500 V (middle) and 400 V (bottom) to observe the effect on the 59.5 keV tail.

If the high count rate x-ray data in Fig 7-3 is now re plotted using the density plot approach shown above, the lozenge region and pulse pile up region can be clearly distinguished. Fig 7-8 shows the density plot of all data and clearly illustrates the lozenge region similar to that in the previous figures. The pulse pile up is not observable here as the random nature of the pulse pile up results in a low density spread above the lozenge region.
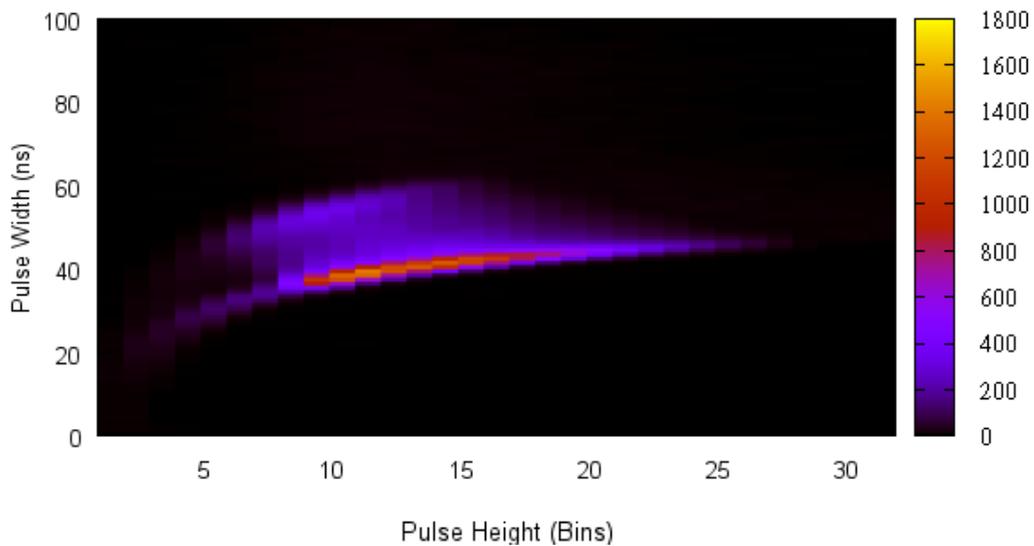

Fig 7-8 HW density plot of 100,000 detected events from the 0 to 160 keV bremsstrahlung continuum from a tungsten x-ray tube as shown in Fig 7-3.

In order to see the pile up outside of the lozenge region Fig 7-9 shows a cross section through Fig 7-8 taken at 20 counts ($z = 20$). This clearly shows the spread of piled up pulses above the lozenge. In addition to this, the shape of the lozenge can still be observed even in the presence of the piled up pulses.
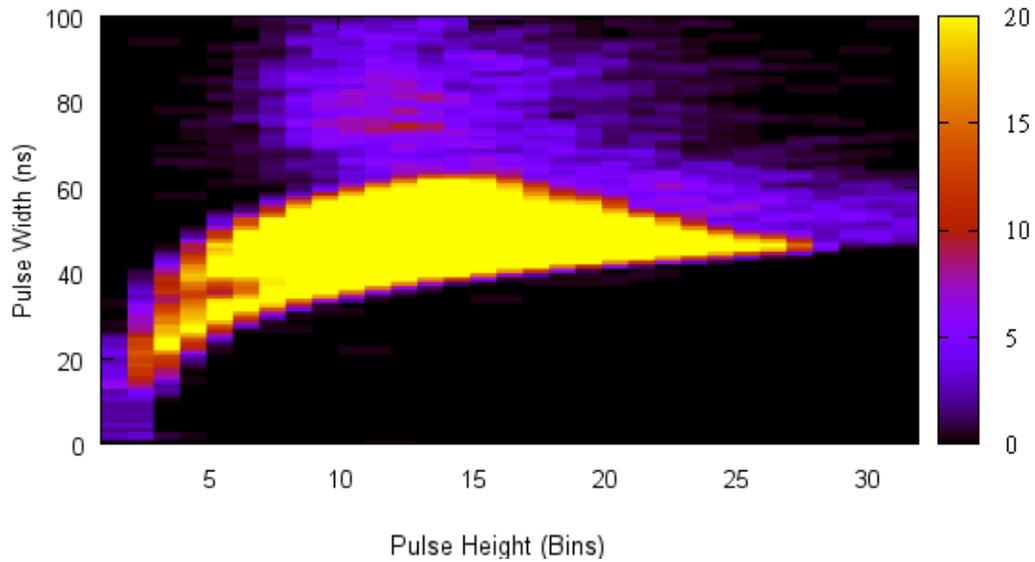
Fig 7-9 A cross section of the HW plot from Fig 7-8 taken at a position of $z = 20$ in order to make visible the pulse pile up outside of the lozenge region.

As illustrated in Fig 7-10, pulses can now be categorised into three types by their location in height-width space.
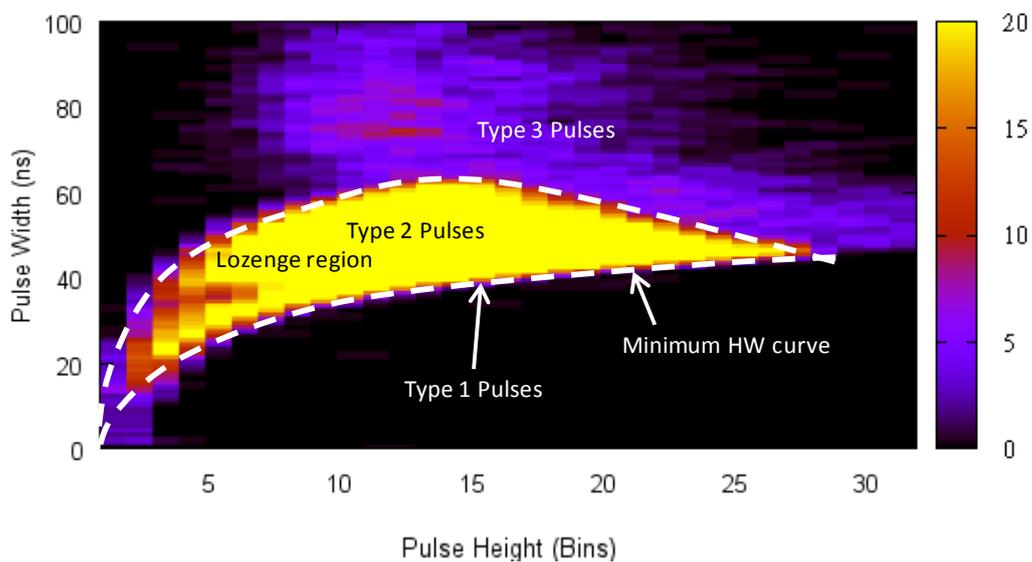

Fig 7-10 HW plot from Fig 7-9 showing the three types of pulses classified based on their positions in height-width space. See text below for definitions of these three types of pulse.

Pulses can be categorised into one of the following types:

- *Type 1* pulses which have both heights and widths which conform to the theoretical minimum for the shaping amplifier in question.

- *Type 2* pulses where the height and width of the pulse is distorted by depth of interaction effects or very closely time spaced pulse pile up.

- *Type 3* pulses where the height and width of the pulse is distorted by pulse pile up effects at greater time separations than in type 2.

The location of pulses in height-width space can now be used to both correct for depth of interaction effects and remove a significant fraction of the pulse pile up. The methodology behind this is discussed in the following section.

7.2   Depth of Interaction Correction

In the previous section it was shown that there are two causes for the incorrect bin assignment of pulses. These are depth of interaction effects (type 2 pulses) and pulse pile up effects (type 2 and 3 pulses). Pile up events with large time separations can be distinguished due to their clear separation from the lozenge region. Pile up events with small time separations are indistinguishable from type 2 pulses, and represent the limitation of the algorithm. The percentage of such pulses is estimated in Section 7.4 via Monte Carlo simulation in Geant4.

The correlation between pulse width and pulse height in the case of type 2 pulses then allows a correction method to be applied in order to 'map' back pulses onto the minimum HW curve. The HW correlation can be seen more clearly by plotting in three dimensions. Fig 7-11 shows a HW plot of 100,000 events from a ^{57}Co source from Fig 7-4.
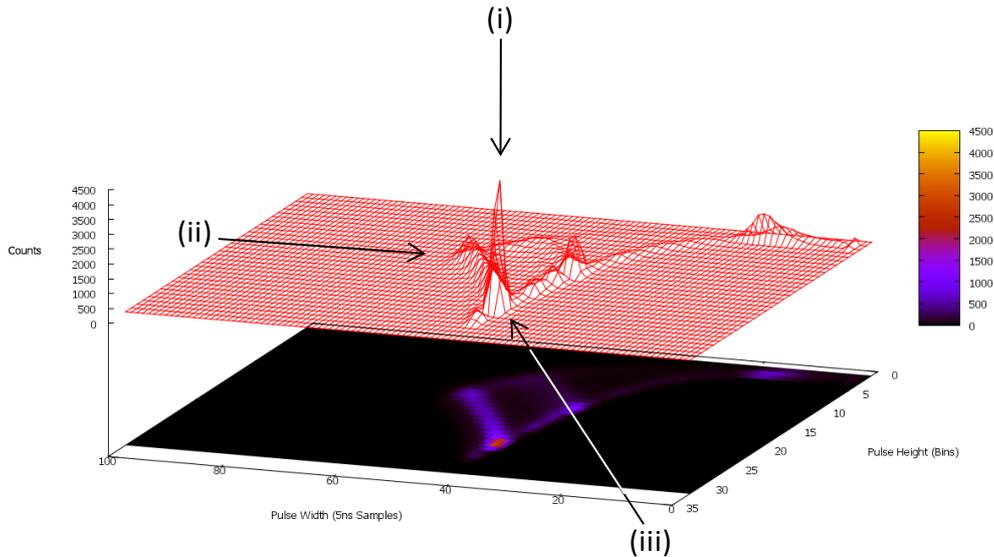

Fig 7-11 HW plot of the spectrum from a ^{57}Co source. This 3D plot is of the same data set as that shown in Fig 7-4 with the third axis indicating the number of counts at a given (H, W) coordinate.

As can be seen from Fig 7-11 the 122.1 keV peak shows a tail which relates to events of greater width and reduced height. As discussed in the previous section these events are clearly from the 122.1 keV peak. Standard pulse height spectroscopy wrongly assigns such events to a lower bin. The effect of this was previously seen in Fig 5-5 and results in a degraded spectrum under these measurement conditions.

The arrows on Fig 7-11 indicate the key view points where (i) is the two dimensional HW plot seen in previous figures, (ii) is analogous to the view point of standard pulse height spectroscopy techniques such as those described in Chapter 4 where the spectrum is degraded by type 2 events, and (iii) is the preferred view point which projects the tailing effects back on to the main peaks as would occur by removal of type 2 pulses. The third view point will be discussed in further detail here.

7.2.1 Depth of Interaction Correction of Pulses

As each point on this lozenge maps back to a unique point on the minimum HW curve this allows a reassignment of pulses based on their unique pulse height to pulse width relationship.

For illustration purposes the effect of viewpoints (ii) and (iii) shown in Fig 7-11 on the shape of the ^{57}Co spectrum is illustrated in Fig 7-12. Fig 7-12 (a) shows the spectrum from viewpoint (ii) which is analogous to a standard pulse height measurement. Fig 7-12 (b) shows a flat projection of Fig 7-11 from viewpoint (iii). This projects the tail from each peak back onto the main peak.

(a)

(b)

Co⁵⁷ 122 KeV
Co⁵⁷ 136 KeV
Te Escape Peak
Cd Escape Peak
Pb Flourescence
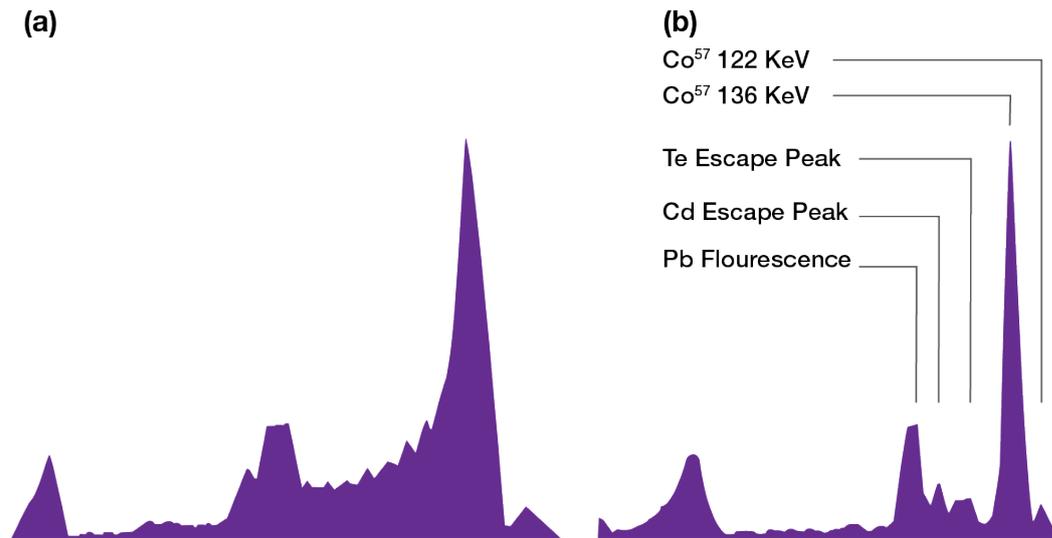
Fig 7-12 Graphs showing the 3D HW plot from Fig 7-11 from the two different viewpoints. See text above for a full explanation of this figure.

Whilst this is merely a visual projection and is in fact analogous to the case of filtering out all type 2 pulses it provides a good illustration of the improvements which can be made to the detector resolution by this technique. This improvement in resolution allows the cadmium and tellurium escape peaks [80] to be seen along with the fluorescence peak from the lead source holder. Such features are ordinarily hidden by the tail of the 122.1 *keV* peak as in Fig 7-12 (a).

7.2.2 The HW Algorithm

A great improvement to the resolution of a ^{57}Co spectrum can be made by a simple visual projection of the tails from each peak back onto the main peak. In this section an algorithmic method of performing true depth of interaction correction to the spectrum will be discussed.

Taking the gradient of the tail of the 122 keV peak ($\Delta W/\Delta H$), the incorrectly assigned pulses can be mapped back onto the minimum HW curve. This is done by calculating the true height, H for a pulse of measured height and width H', W' respectively. The basic pulse detection algorithm remains as described in the flow chart in Fig 4-8 with the addition of a measurement of the base width, W'. This is calculated by measuring the crossing time of the threshold by the pulse as shown in Fig 7-13. Note that here the pulse widths and heights are referred to as H' and W' respectively as this reflects the possibility that the measured heights and widths of any given pulse may differ from the true corrected heights and widths.
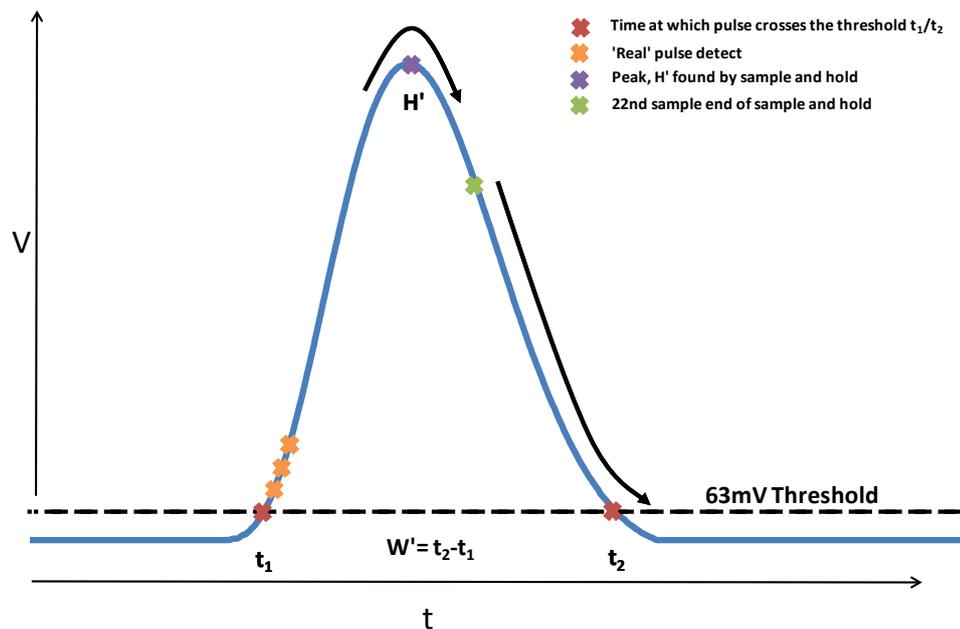
Fig 7-13 Graphical representation of the algorithm used to obtain H' and W' for a given pulse.

As in the case of Algorithm 2, the pulse detect state is not enabled until the pulse has dropped below the threshold level thus preventing the registering of any secondary pulses which are convoluted with the first. The values of H' and W' are then returned by the algorithm and as will be described later are used to index

173

the true height of the pulse from a lookup table. An example of such a lookup table is shown in Fig 7-14.

Fig 7-14 128x32 element lookup table used to correct depth of interaction effects by applying the transformation $(H', W') \rightarrow (H, W)$. Note omitted cells contain zeros and refer to locations where H' and W' are uncorrelated due to pulse pile up.

In the case where $H' = H$, the value in the lookup table at location (H', W') is the same as H'. Where $H' \neq H$, the value in the lookup table is either a corrected height value or alternatively a zero. A zero in the lookup table reflects the fact that H' and W' do not correlate to any H, W coordinates which are deemed to define a real pulse. By this measure such pulses are regarded as piled up and are therefore discarded. It should be noted that if no correction is applied to any H', W' values, the output is then identical to that of Algorithm 2 and any such cases are therefore referred to as such in the preceding pages.

Pulses for which $(H', W') = 0$ are not added to the pulse height spectrum but the value W' for such events is added to a cumulative discard counter. Whilst the number of pulses in a given discard period or indeed the energy of such pulses is

not known this feature provides a useful dead time counter which can be used to assess the percentage of dead time for a given acquisition. As discussed in Chapter 4, further statistical analysis could be carried out in order to correct for such a dead time however this possibility has not yet been explored.

This correction is trivial to carry out on pre acquired data from the oscilloscope using a software package such as Excel. Taking the raw data from Fig 7-11 the pulse height (voltage) data can be binned into a number of H' locations without the bin number restriction present on the FPGA. This data can then be mapped back as described. The result of this is shown in Fig 7-15, where the spectrum has been corrected before being binned into 128 bins.
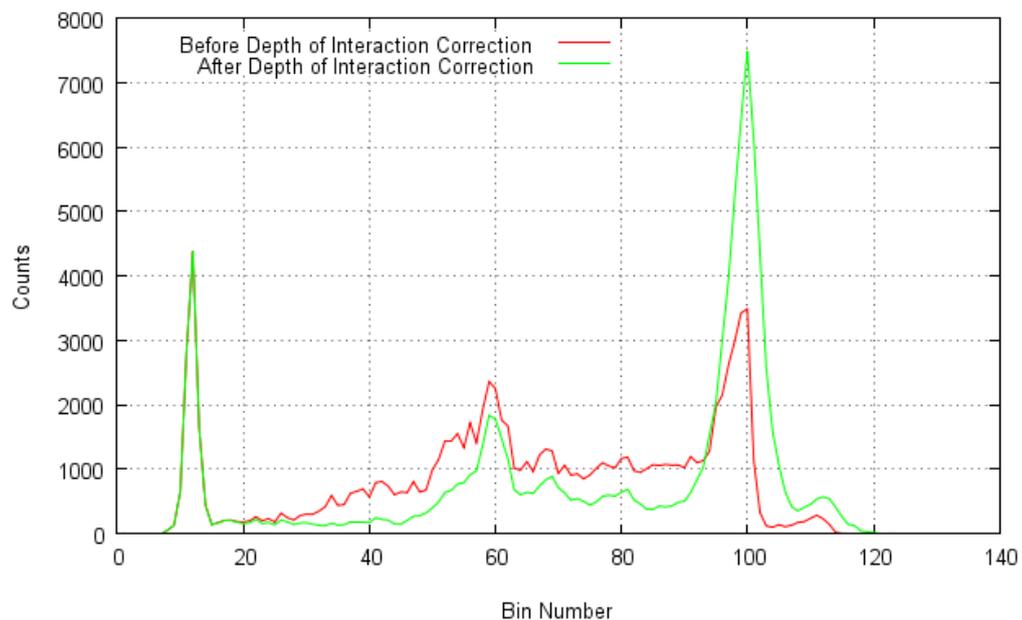
Fig 7-15 128 bin pulse height spectra collected using a DSO90254A oscilloscope and processed using a Matlab pulse height detection algorithm. The spectrum in red shows a standard acquisition using an emulation of Algorithm 2 similar to that shown in Fig 5-2 and the green spectra shows the HW depth of interaction correction.

The computation of H for a given H', W' is too complex to be carried out in real time on an FPGA so instead must be carried out offline. A 128×32 value lookup table is generated containing the reassigned bin value for a given H' and W'. This takes the form shown in Fig 7-14. The resolution of the height field is equal to 1 bin and the resolution of the width field is from 1 to 128 samples with a sampling period of 5 ns per sample.

As can be seen in Fig 7-14 many of the cells contain a zero and represent a location for which there is no $(H', W') \rightarrow (H, W)$ correlation. Any pulse which looks up such a location is returned as a zero meaning that it is discarded.

The 128×32 value lookup table was produced by geometric calculations using a low count rate ^{57}Co HW plot as shown in Fig 7-11. Here it is assumed that there is no pulse pile up present and can therefore be used to define the lozenge. This lookup table along with the modification to the pulse detection algorithm was then programmed [66] onto an FPGA and tested using a ^{57}Co source. An acquisition using Algorithm 2 was also carried out and is shown alongside the corrected spectrum in Fig 7-16 for comparison. A measurement time of 80 seconds (5000 frames of $16\,ms$) was selected in order to achieve a total of approximately 100,000 counts in each spectrum. The actual counts within each spectrum for both acquisitions are in agreement to within the Poisson error.
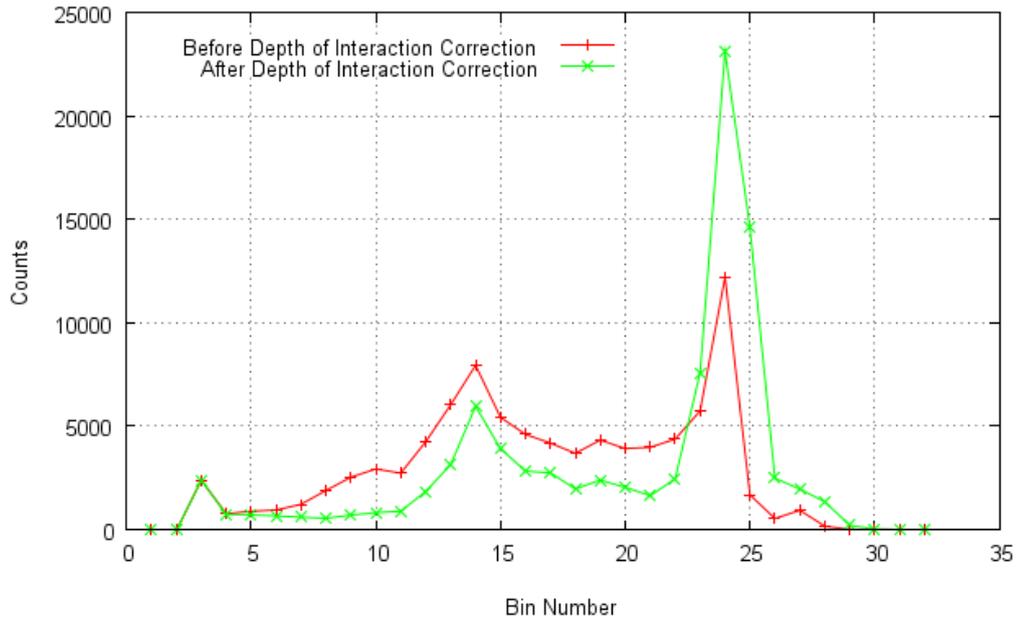
Fig 7-16 Graph showing the ^{57}Co spectrum before and after depth of interaction correction. The data here was taken using an FPGA with a 128×32 value lookup table which was used to reassign pulses to the correct bin.

The corrected spectrum in Fig 7-16 shows a marked improvement in the resolution compared to that of Algorithm 2. The improvement is limited by the accuracy to which H' and W' are known. Further improvements may be made by increasing the sampling frequency of the A to D to better define W' and increasing the number of bins used in the FPGA algorithm to increase the resolution of H'. This would allow for finer mapping back of pulses.

7.3   Geant4 Simulations of HW Plots

It has been clearly shown that the pulses outside the lozenge region of the HW plot are due to pulse pile up. In low count rate measurements with ^{57}Co and ^{241}Am sources it was shown that the lozenge region and tails emanating from the various spectral peaks are due to depth of interaction effects.

This makes pile up removal from outside of the lozenge region trivial. Any piled up pulses inside the lozenge by definition cannot be distinguished using this algorithm and it is therefore not possible to experimentally verify the proportion of such pulses. These are due to very closely spaced events such that the width and height of the convoluted pulses does not exceed the boundary conditions set by the lozenge. In order to assess the usefulness of this method it is important to quantify the proportion of such pulses.

The simulation [78] discussed in Chapter 6 can be used to model the effect of pulse pile up on the HW plot. The signal is constructed using the depth of interaction information from the Geant4 model and the shaping amplifier signal is calculated. As in Chapter 4 the events are randomly generated using a Monte Carlo approach meaning that pulse pile up is observable at higher rates. HW values are then returned in a binned 128×32 array in the same way as the FPGA algorithm illustrated in Fig 7-13. One million detected events are simulated for each count rate. Whilst one million are detected, the number of simulated photons emitted from the x-ray tube is many orders of magnitude

178

higher as events are lost due to the small solid angle of the detector, scatter of photons within the intervening medium and incomplete absorption by the detector.

As the events are generated within the model itself it is possible to know the number of pulses contributing to any single HW value. This represents the Monte Carlo truth and is not obtainable by experiment. Using this information the relative proportion of pulse pile up inside and outside the lozenge can be quantified.

The lozenge shape is defined within the model by a low count rate simulation at 1 cps as shown in Fig 7-17 and it is assumed that no pulse pile up is present and therefore the lozenge shape is entirely due to depth of interaction effects. The simulation was carried out using a pulse shaping time of $50\ ns$. As can be seen Fig 7-17 shows reasonable agreement to the experimental data in Fig 7-8.
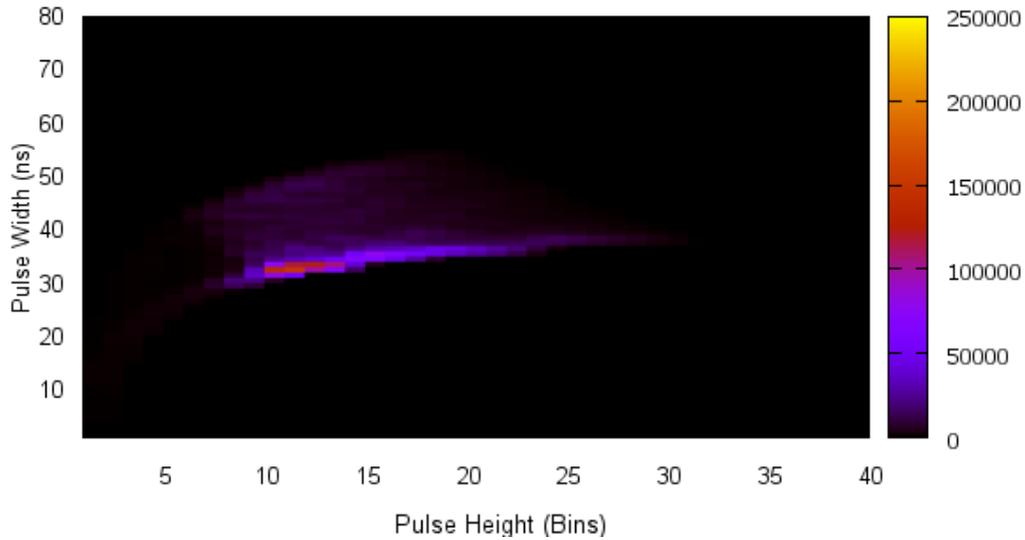
Fig 7-17 HW plot from a low count rate Geant4 simulation of the 0 to 160 *keV* x-ray spectrum from *I_c*. The simulation includes depth of interaction effects due to ballistic deficit and charge trapping which give rise to the characteristic shape of the plot.

The HW plots in Fig 7-18 show the effect of a detected count rate of 500 *kcps*. Fig 7-18 (a) shows a HW plot of all three pulse types, Fig 7-18 (b) shows only pulses containing one event (non piled up events only) and Fig 7-18 (c) shows pulses containing multiple events only (piled up events). The x-axis has been extended to 64 bins in order to accommodate all piled up events and the z-axis has been restricted to 40 counts in order to allow the piled up pulses to be clearly visible against the main lozenge. Pulses with magnitudes greater than the bin equivalent of 32 are outside the range of the FPGA. As these pulses can only originate from pulse pile up they are discarded by the algorithm.
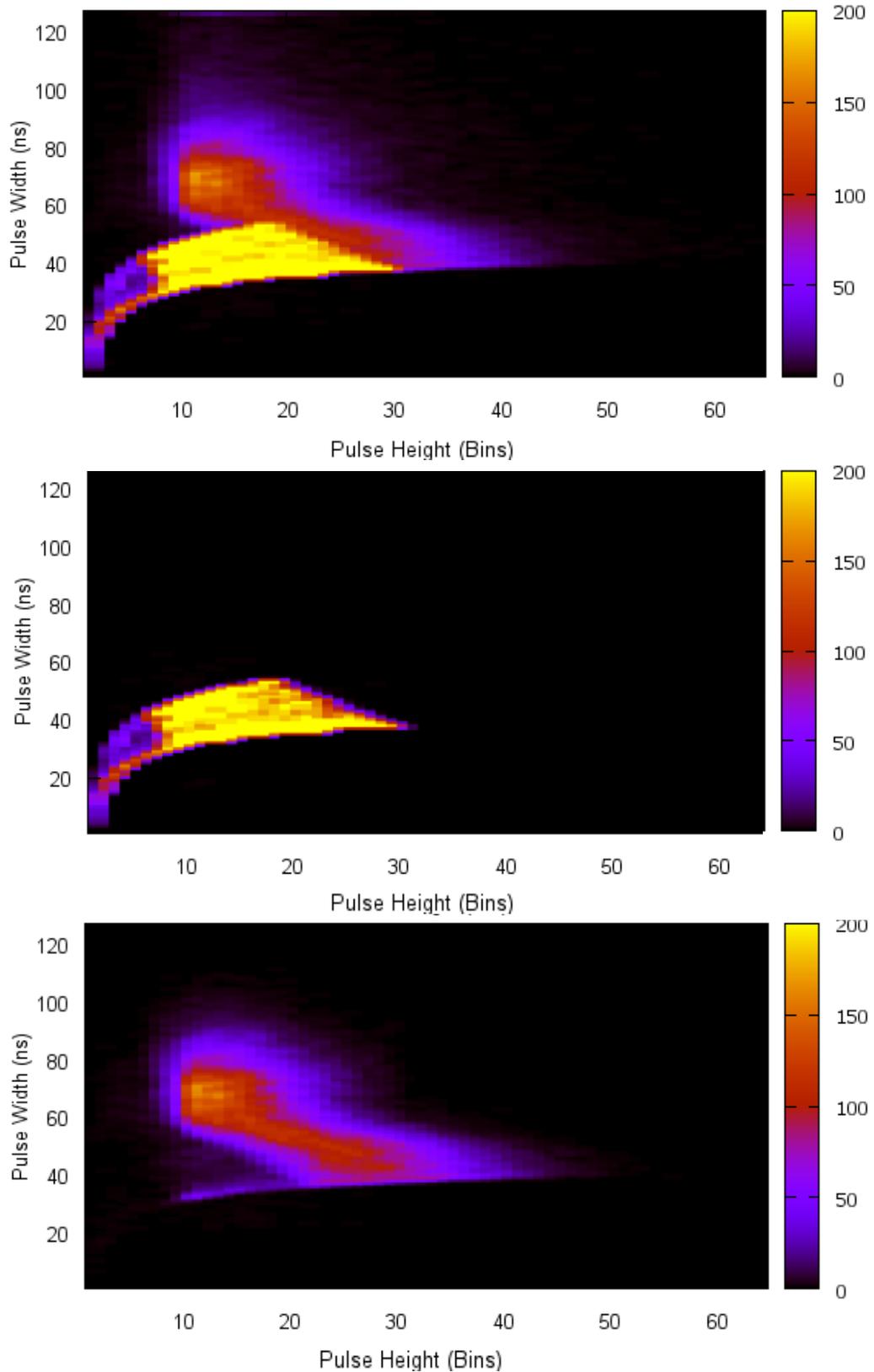
Fig 7-18 Simulation of x-rays incident on a detector from a tungsten tube. The spectra shown here are at a detected count rate of 500 *kcps* in I_c. From the top to the bottom of the figure: (a) HW density plot showing the locations of all piled up and non piled up events (top), (b) all non piled up events (middle), (c) piled up events only (bottom).

As can be seen from Fig 7-18 (c) a significant number of piled up pulses exist inside the lozenge region. This is expected from the modelling carried out in Chapter 4. Here the probability of pulses having a time of greater than $n\delta t$ between them was given by Equation 4-6 and shown to have an exponential form. The width component in a HW plot can be regarded as being analogous to this where the distribution of pulses along the width axis due to pulse pile up is defined by the same probability distribution. The difference in width distribution on a HW plot from the pure RTSE type distribution is due to the addition of depth of interaction effects and the concept of a minimum pulse width defined by the minimum HW curve. Such a minimum clearly does not exist for point processes and is only observed here due to the point spread functions of the preamplifier and shaping amplifier.

Also observable is the clear similarity of the lozenge outline in Fig 7-18 (b) to the low count rate simulation in Fig 7-17. The lozenge shape is completely blurred out in Fig 7-18 (c) due to the random interaction of piled up pulses. Using this type of analysis for different count rates, the percentage of piled up pulses inside and outside of the lozenge and therefore the pile up rejection efficiency of the algorithm can be determined.

Fig 7-19 shows the percentage of the total counts piled up inside the lozenge at count rates of $200\ kcps$ to $600\ kcps$. Here the low count rate (1 cps) simulation was used in order to define the lozenge region. It was then calculated that $20.3\% \pm 0.2\%$ of piled up pulses occur within the lozenge region and $79.7\% \pm$

0.2% occur outside of the lozenge region. Whilst the number of piled up events relative to the starting number of events increases with count rate, the proportions inside and outside the lozenge remain constant within the errors stated as intuitively expected.
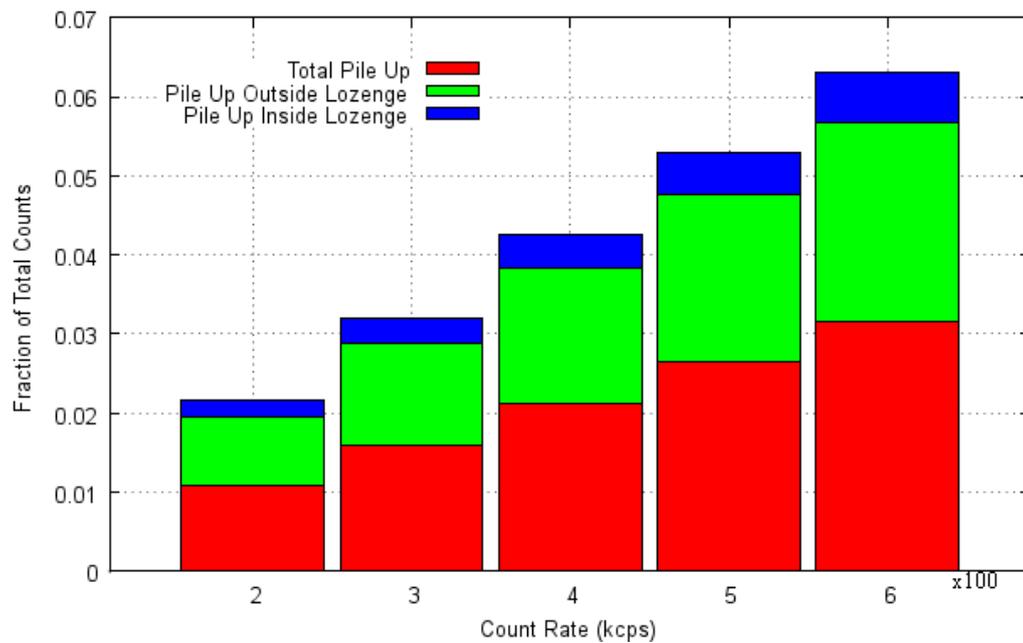
Fig 7-19 Pile up percentage for count rates of 200 *kcps* to 600 *kcps* in I_c.

Clearly a further level of sophistication is required in order to remove pulses from within the lozenge region however the approach outlined here is straightforward enough to be implemented on an FPGA in real time and has an efficiency of around 80% for pile up removal from the modelled system. The algorithm efficiency is highly dependent on the size of the lozenge which is in turn dependant on the material properties. Therefore, as with other applications, high electron and hole mobility lifetime product, high electric field and minimal device thickness are desirable features for achieving good high count rate operation.

Fig 7-20 shows a deviations plot of the I_c spectrum for various count rates and shows the familiar behaviour discussed in Chapter 4, with counting deficit in the low bins and excess in the high bins due to incorrect bin assignment of piled up pulses. This plot considers all pulse widths with no filtering applied and shows that the model is behaving as expected.
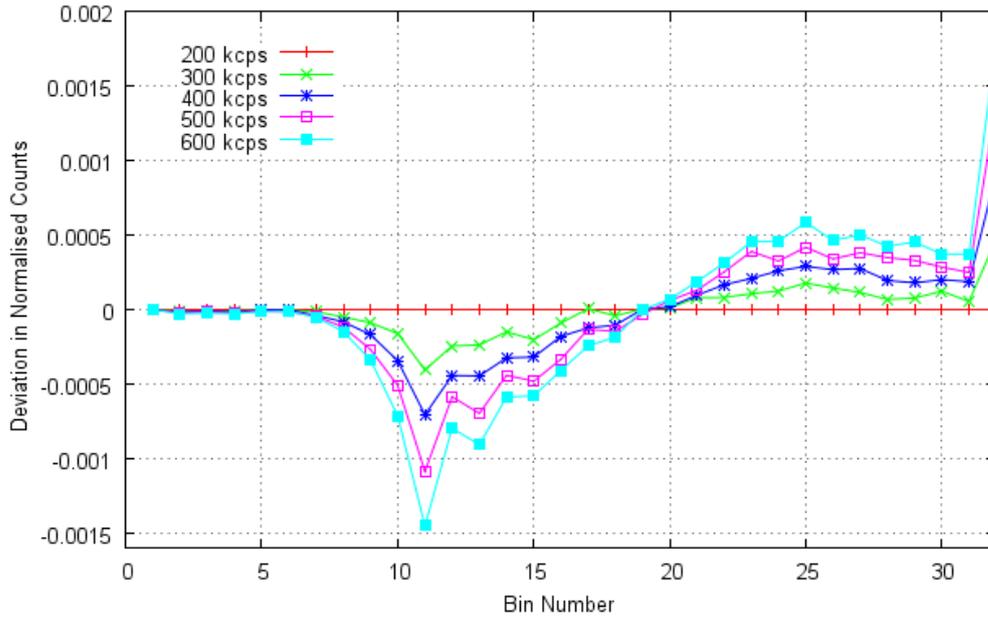
Fig 7-20 Deviations plot of normalised I_c counts as a function of bin number for various count rates. Here the deviation is with respect to a rate of 200 *kcps* measured in I_c and the counts are taken from all locations within the HW plot. The rate dependant deviation in counts is as discussed in Chapter 4 and due to pulse pile up.

Again using the data from the low count rate simulation in Fig 7-17 to define the pile up free lozenge region, the same analysis can be repeated but this time taking only the lozenge region into account, this is shown in Fig 7-21.
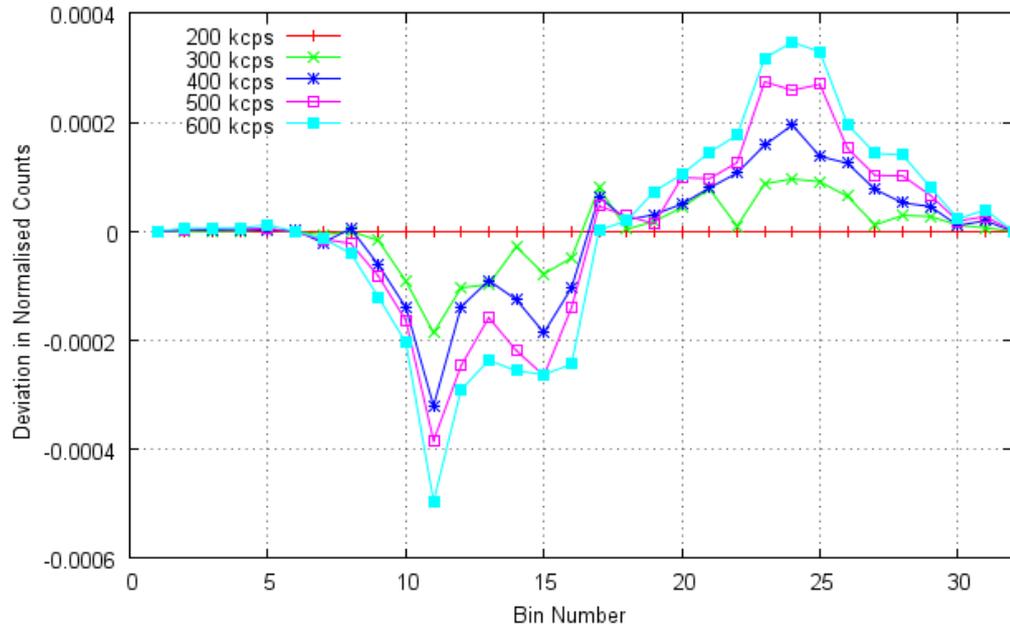
Fig 7-21 Deviations plot of normalised counts as a function of bin number for various count rates. Here the deviation is with respect to a rate of 200 $kcps$ in I_c and the counts are taken only from those occupying the lozenge region of the HW plot.

Comparing the results from Fig 7-20 and Fig 7-21 it is clear that the magnitude of the deviation is reduced by removal of counts which appear outside the lozenge region, making the I_c measurement less sensitive to variations in count rate. Also the pile up in bin 32 with pulses of greater than 1 V is removed as such counts do not form part of the lozenge. This can be seen more clearly by taking the total absolute deviation for each count rate from Fig 7-20 and Fig 7-21. The total absolute deviation is plotted as a function of count rate in Fig 7-22.
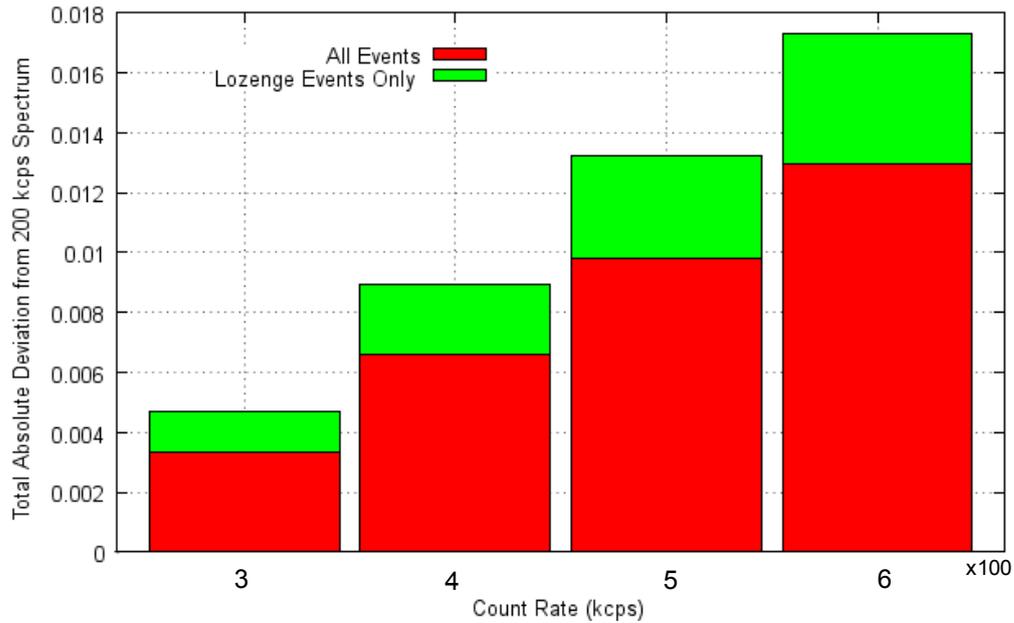
Fig 7-22 Total absolute deviation as a function of count rate where all events are included in the spectrum and where lozenge only events are included. Here the deviation is measured with respect to the 200 $kcps$ I_c measurement as in Fig 7-20 and Fig 7-21.

From Fig 7-22 it can be seen that removal of type 3 pulses reduces the total deviation across the spectrum by over two thirds when compared to Algorithm 2. The following sections will look at the effect on transmission by repeating this analysis on the I spectrum, then taking the ratio I/I_c.

7.4 The Effect of HW Filtering on Transmission Spectra

As seen in Chapter 5, both Algorithms 1 and 2 showed artefacts due to pulse pile up and were shown to be unstable with varying input count rates. Whilst the HW filtering approach is useful in the future design of detectors for spectroscopy applications, any features which appear detrimental to such systems are not necessarily a concern for this application.

The reason for this is that by taking an I/I_0 or I/I_c measurement, any features of the spectrum which are common to both spectra will be normalised out of the measurement. Equally any features which are not normalised out of the spectrum but can be shown to be invariant from run to run and preferably machine to machine are not necessarily detrimental to the ability to identify liquids. This section therefore looks at the self consistency of modelled transmission spectra at varying input count rates in order to assess the stability of the transmission spectra with and without removal of type 3 pulses. This was done using a simulated I and I_c spectra, where the I simulation was carried out for a pyrex cuvette with a path length of $100\ mm$.

The raw transmission spectra are shown in Fig 7-23 for count rates of 450, 500 and 550 $kcps$ as measured in I_c with various levels of pile up treatment applied to the HW plot. Firstly the pulse pile up is removed completely by reference to the photon time of arrival information from the simulation. Whilst this is not possible in a real system it represents the ideal case in terms of pile up removal so is useful as a baseline from which to measure relative performance. The second set of spectra includes all events in the HW plot with no pile up removal applied, and the final set of spectra is with type 3 events removed.

The total simulated events are approximately 10 million in I_c and around 2.8 million in I. Also shown is the low count rate simulation at 1 count per second which has the expected increase towards high energies.
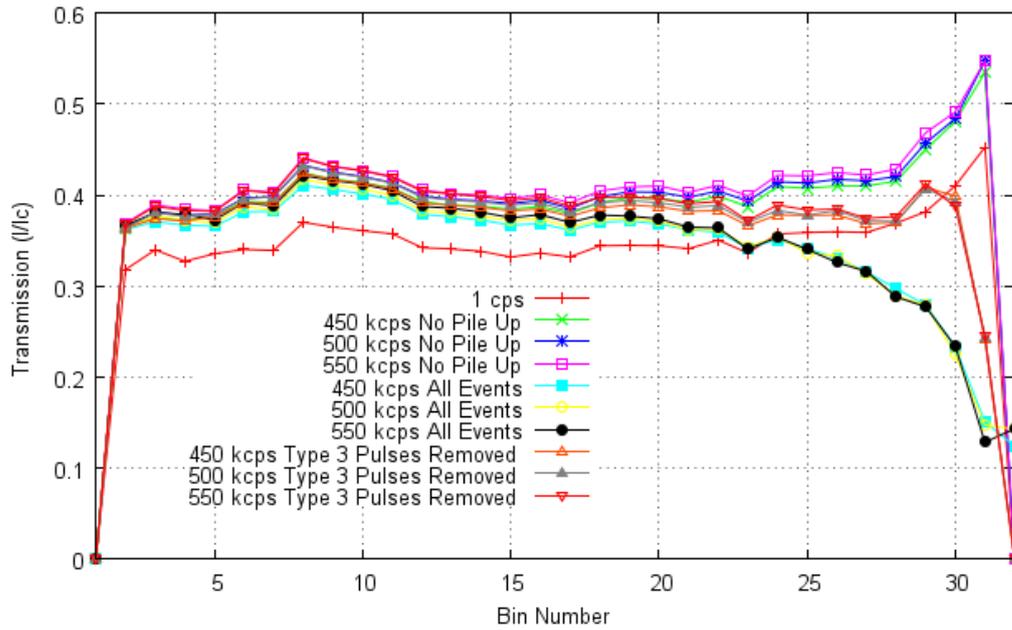
Fig 7-23 Modelled transmission spectra from a Geant4 simulation. Here the transmission is calculated from I/I_c where I_c is derived from a calibration block made from PEEK. The transmission data shown is with pile up removed, all events with no pile up removal and with type 3 events removed. Each simulation was carried out at rates of 450, 500 and 550 *kcps* as measured in I_c..

The type 3 pulse removal was carried out by using the low count rate HW simulation in order to define the lozenge region. As such pulses are not subject to pulse pile up, any deviation from the minimum HW curve is due to depth of interaction effects only. Each family of curves is normalised and replotted in Fig 7-24 with error bars given by the propagated Poisson errors in I and I_c.
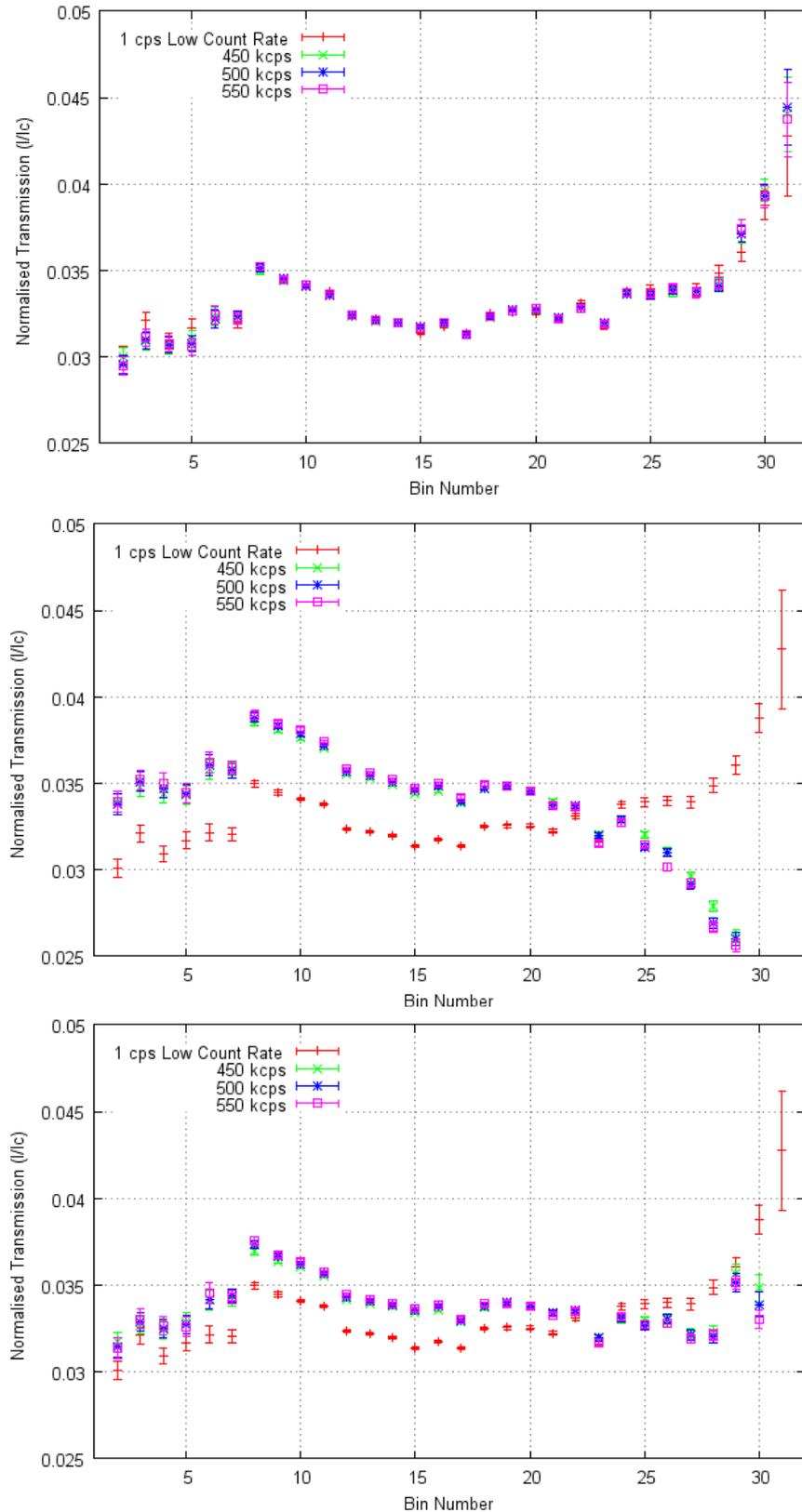
Fig 7-24 Normalised transmission spectra from a simulation with various degrees of pile up treatment: All pile up removed from I and I_c (top), no pile up removed (middle), and pile up removed from inside lozenge only (bottom). Each plot shows three spectra with a count rate of 450 $kcps$, 500 $kcps$ and 550 $kcps$ to illustrate the transmission stability at varying count rates. A low count rate simulation at 1 cps is also shown in each graph for comparison.

As discussed in Chapter 4 the probability of pulse pile up is not uniform across the spectrum due to the larger base widths of high energy pulses which make them more likely to pile up. Removal of all piled up pulses if it were possible would have the effect of removing perturbations due to pulse pile up which would in turn be replaced by perturbations due to pile up removal. Without the aid of simulation it is not clear that this would lead to an improvement in the stability of the transmission curves and therefore whether this is a meaningful mode of operation to strive for.

Fig 7-24 (middle) shows the transmission spectra with no pile up removal from I and I_c. As can be seen the curves exhibit a rollover at high energies due to pulse pile up effects. Rollover is significantly reduced by pile up removal from outside the lozenge (bottom) and almost ideal transmission is regained by complete pile up removal (top). This illustrates that for this scenario the removal of piled up pulses is advantageous even if the pulses cannot be added back into the spectrum and implies that the perturbations in transmission caused by pulse pile up are greater than those caused by pile up removal. The transmission spectra can also be seen to be much less sensitive to changes in count rate with complete pile up removal.

The more realisable solution is to remove the type 3 pulses from outside of the lozenge region. Fig 7-24 (bottom) shows the transmission with type 3 pulses removed. The filtering of these pulses results in transmission curves which show a much improved agreement to the low count rate simulation when compared to

190

the case in Fig 7-24 (middle) where no pile up removal is carried out. The rollover at high energies is still observable but to a much lesser extent, and in addition to this the transmission curves show less sensitivity to variations in count rate.

Whilst the modelled transmission spectra show a significantly better agreement to low count rate transmission with removal of type 3 pulses, the key interest is the stability of the transmission shape with varying count rate. The variability can be quantified by a Z-test. Taking the $500\ kcps$ transmission curve as the centre value in each case, the Z_0 can be calculated for each of the three sets of curves shown in Fig 7-24 using Equation 3-3. This is calculated here for the normalised transmission and is therefore only sensitive to changes in the shape of the transmission curve rather the absolute value. Fig 7-25 shows the sum of Z_0 across all bins for count rate perturbations from 500 to $450\ kcps$ and from 500 to $550\ kcps$ for each type of pile up treatment.
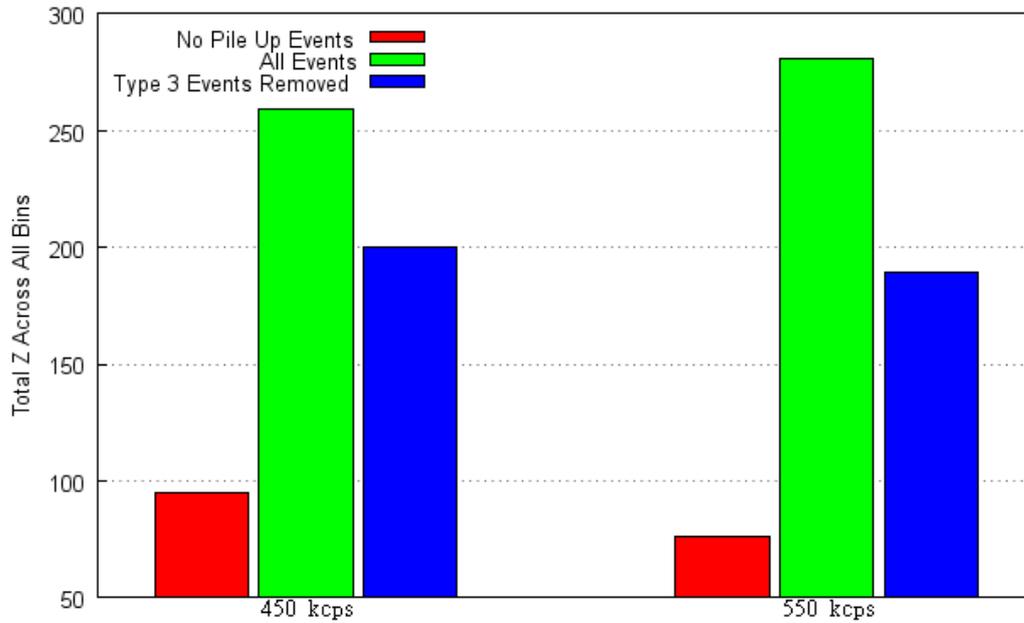
Fig 7-25 Graph showing the total z across all bins for a Z-test of the I/I_c spectra in Fig 7-24.

As can be seen from Fig 7-25 the lowest variability is observed with complete pile up removal however a notable improvement can be seen by removal of type 3 pulses from the I and I_c spectra. The improvement is around a 32% reduction in Z_0 where the counts are perturbed from 500 $kcps$ to 550 $kcps$.

7.5   Conclusion

In this chapter an algorithm has been discussed which both removes piled up pulses and corrects those where depth of interaction effects have degraded the pulse height. This is done by use of a HW filter which has been implemented on an FPGA to allow real time acquisition/correction to be carried out.

The filter is successful in both removing the majority of pulse pile up and correcting for depth of interaction effects and does so without any loss to the throughput rate of counts. This work has given a better understanding of the factors affecting the transmission spectrum and has enabled these to be included into the ongoing Geant4 modelling program.

Experiments using an oscilloscope implementation of the correction algorithm have shown significant improvements in the pulse height spectrum for a ^{57}Co spectrum at low count rate. The algorithm was then implemented on an FPGA and showed a similar level of improvement. Whilst the improvement in resolution is clear, the effect of filtering on pulse pile up and the final transmission spectra is more difficult to quantify. In particular the effectiveness of the algorithm in dealing with pulse pile up cannot be measured via experiment due to an inability to distinguish between real events and incorrectly binned piled up events.

For this reason a Geant4 model was used in order to simulate the transmission spectra with detector related effects such as carrier mobility and lifetime, pulse pile up and ballistic deficit. Using this model it was then possible to quantify the proportion of piled up events which would be incorrectly binned by the HW algorithm. It was found that pulse pile up events exist inside the lozenge region. They represent approximately 20% of the pile up total and are indistinguishable from events which are perturbed by depth of interaction effects.

The effect of pile up and pile up removal on the end transmission spectra was then explored using a reference transmission from a low count rate simulation. It was found that the closest match to a low count rate transmission was achieved by complete removal of piled up pulses. This shows that the perturbations introduced by pile up removal are less than those due to the inclusion of pile up in the I and I_c spectra. Whilst complete pile up removal is not possible in a real system, such a simulation provides useful direction for future treatments.

The removal of the majority of events via HW filtering was shown to be advantageous when compared to the more simple paralyzable Algorithm 2 outlined in Chapter 4. The stability of each transmission curve was tested by varying the count rate by $\pm 10\%$ from the operating point of $500\ kcps$ in I_c. Using a Z-test it was shown that the HW filtering algorithm leads to a reduction of around 32% in the value of Z_0 summed across all bins when compared to Algorithm 2.

HW filtering approach has also been shown to give a large improvement to the resolution of the detector. This improvement is exaggerated due to the effects of the very short shaping time used in this application however this could also be used in longer shaping time systems.

This approach is likely to give improvements to detector resolution where charge collection efficiency is a problem, for example in very thick high energy detectors. Here the pulse height dispersion due to depth of interaction effects is increased. Additionally this may also allow material currently not deemed to be suitable for use in spectroscopy applications to be used, such as material with low mobility-lifetime products.

Chapter 8   Conclusions and Further Work

8.1   Conclusion

The aim of this work was to design a detector system capable of detecting high count rate and high energy x-rays for the production of a Bottle Scanner system with the capability of identifying liquids inside sealed bottles in order to address the aviation security market requirement.

As discussed, the major difficulty with high count rate detection comes from pulse pile up which distorts the energy spectrum and degrades detector resolution. Methods of dealing with this including the design of paralyzable and non paralyzable FPGA algorithms were discussed. Three such algorithms were devised and modelled using Monte Carlo simulations of the random arrival rate of photons at the detector and it was found that a paralyzable algorithm was the most favourable in terms of minimising spectral distortion. This however comes at the cost of count rate and a solution was proposed using Algorithm 3 whereby pulses could be added back into the spectrum by reference to the non piled up spectrum.

197

This was shown to be an ineffective method of correcting the spectrum due to the non random nature of the pulse pile up. In order to regain true Poisson type variance in the spectrum a more sophisticated method of pile up inspection is required, for example where piled up pulses are deconvolved. Such a highly computationally intensive approach was not practical using the current Cyclone II FPGA due to the limited number of switching operations which can be performed.

Testing of FPGA Algorithms 1 and 2 on a Bottle Scanner system showed very similar spectral distortion characteristics to those predicted by the Monte Carlo simulations, namely that pulses piling up would result in a loss of counts at lower energy and an increase in counts at higher energies. This resulted in a rotational effect on the Algorithm 1 spectrum. Algorithm 2 on the other hand showed a loss in counts at lower energies due to the pile up effect but was less susceptible to increases in counts at higher energies due to its paralyzable nature.

Calculation of the transmission spectrum for a given material showed a rollover towards the high energy region of the spectrum which was verified by the use of a Geant4 model. This was shown to be due to variations in pulse pile up between the I_0 measurement and the lower count rate I measurement. This therefore showed that the calculation of transmission was not entirely successful in removing non materials related artefacts from the beam and a method of improving this by normalising against a calibration material, I_c was discussed.

The reduction in shaping time was shown to improve the maximum count rate of the detector system however as previously mentioned this resulted in a significant degradation of the spectrum. Results were presented using a ^{57}Co source in order to allow the resolution to be measured. As discussed, this application is somewhat unique in that it is the transmission spectrum which is the measurement of concern and not the individual I and I_0 (or I_c) measurements, therefore degradation in the resolution of individual spectra does not automatically infer a loss in material identification capability due to the normalising effect of the transmission measurement.

The degradation due to shaping time was shown to be due to a depth of interaction effect. By referring to the Beer-Lambert law it can be seen that the average depth of interaction in I is greater than that in I_0 due to the beam hardening from the presence of a bottle in the beam path during the I measurement. This prevents the depth of interaction effect from being normalised out of the transmission spectrum.

A new approach to this problem was discussed in Chapter 7 where a modification to Algorithm 2 was developed in order to carry out a real time depth of interaction correction on incompletely collected pulses. This was done using a biparametric style approach to analyse the shaping amplifier signal directly. Measurement of the height and width of a pulse above a $63\ mV$ threshold allows pulses to be plotted in a three dimensional height-width space. By analysis of the tailing effects from ^{57}Co and ^{241}Am sources a geometrical correction of pulses

could then be applied in order to map back pulses from the tail region of each pulse.

By employing this technique the resolution of the detector was significantly improved in an emulated 128 bin version of the algorithm using a DSO9054A oscilloscope. A 32×128 element lookup table was then generated in order to carry out the correction in real time using an FPGA. As this procedure is insensitive to the origin of the pulse degradation, pulses degraded by both ballistic deficit and charge trapping are both corrected by this technique.

From low count rate gamma measurements, all pulses affected by depth of interaction effects were found to exist inside a well defined lozenge region where the degraded pulse correlates uniquely back to a correct location in height width space, $H', W' \rightarrow H, W$. As piled up pulses can interact at any time separation this leads to convoluted pulses with widely varying widths and heights, these cannot be correlated back to a true location in height width space. Consequently a significant fraction of these pulses exist far outside the lozenge region due to their significantly larger widths and/or heights. It is therefore possible to set a boundary condition excluding such pulses from the output spectrum.

It was found by simulation in Geant4 that around 80% of piled up pulses exist outside of the lozenge region leaving 20% inside the lozenge region at a count

rate of 500 *kcps*. This represents the limitation of this algorithm and piled up pulses inside the lozenge region cannot currently be identified.

As previously discussed pulse pile up does not have a flat probability distribution and perturbs the spectrum in a way that cannot be normalised out of a transmission measurement. Therefore any removal of piled up pulses is also not equally probable at all energies meaning that it is not intuitively clear whether pile up removal produces a benefit to the stability and integrity of a transmission measurement. This was tested with the aid of a Geant4 model by measuring the self consistency of transmission spectra at various count rates with and without pile up removed.

It was found that the removal of pulse pile up was indeed beneficial and moreover gives a transmission spectrum which more closely matches that of a low count rate, pile up free simulation. In addition to this, removal of all piled up events from inside and outside of the lozenge was shown to give excellent agreement with the low count rate measurement and resulted in reduced sensitivity to variations in count rate. Clearly this is not possible in the real world but suggests that the idea of pulse pile up removal is beneficial at a count rate of around 500 *kcps* and the requirement to add pulses back into the spectrum is not as important as may first be envisaged.

The ability to simultaneously perform both pile up rejection and depth of interaction correction of pulses offers an excellent advantage over other reported systems. The high count rate capability is also orders of magnitudes greater than other correction techniques and offers a solution which does not require complex electronics or custom ASICs. From a wider context the HW approach also has uses in high energy, low count rate applications where large volume, thick detectors (tens of millimetres) detectors are required. Whilst ballistic deficit is not a concern in these low count rate applications, such detectors suffer from a higher degree of spectral degradation due to charge trapping.

The Bottle Scanner system is currently using Algorithm 1 and whilst this was shown to be the poorest performing of all algorithms this was favoured for version 1 of the Bottle Scanner due to its relative simplicity. The work carried out here has provided the basis for the production of the detection part of the Bottle Scanner system. Appreciation of the effects of pulse pile up and depth of interaction effects have enabled the design and operation of the system to be carried out in a way that is sympathetic to these effects. Examples of this include the use of an I_c measurement rather than an I_0 measurement which allows a greater normalisation of such effects, the count rate is also restricted to an upper limit of 500 $kcps$ as the gain in reduced Poisson errors at higher count rates is negated by the loss in spectral shape due to pile up.

With new legislation in place from the end of April 2011 stating that all airports must have a liquid threat screening facility Kromek is well placed in the market

202

to deliver this and is to date one of only two companies to have demonstrated such a capability. The current system is capable of meeting the throughput requirement of 1 bottle every 20 seconds and has a false alarm rate which is well within the customer requirements. The Bottle Scanner has passed the ECAC European safety trials and is now in airports across Europe. The system will also soon be going into U.S. trials with the Transport Security Authority (TSA).

8.2   Further Work

Further work is required to study the effect of the HW filtering approach to the identification of liquid threats. All indications show that this will lead to improved stability and resolution as a result of removing pulse pile up and correcting for depth of interaction effects. It has become clear from this work that reproducibility in a single system is highly count rate dependant and improvements in the treatment of pulse pile up are advantageous. This may lead to reduced system to system variability, opening up the possibility of transferring material databases between machines which is not currently possible.

Improvements in the area of liquid phase growth are resulting in larger area and increased thickness detector grade material. Thicknesses of up to 15 mm are now being grown and have applications in high energy gamma ray detection. Whilst pulse pile up is not a concern in such applications, the increased thickness is expected to lead to significant charge trapping. Work is planned to investigate

the effectiveness of HW correction of such signals in order to reinstate the energy resolution to that expected from much thinner devices.

Recent advances in FPGA and A to D technology open up the possibility of performing more complex deconvolution processes on the piled up shaping amplifier signal, or alternatively allowing pulse height analysis to be carried out directly on the preamplifier signal. As the preamplifier signal is narrower in the time domain this opens up the possibility of further reducing pile up effects.

The Bottle Scanner is defined as a Type B product as it is capable of scanning a single bottle without the need to open the bottle lid. Development of the next generation Type C system has begun which is capable of simultaneously screening multiple containers. This technology requires the development of large linear arrays of detectors and read out electronics and is presenting a range of new challenges and possibilities.

The requirement of high count rate operation is even more important to the type C product with an expected requirement of one million counts per second per pixel. This has lead to the design of a novel detector geometry which deals with the slow hole transit times by confinement of charge generation near to the cathode region of the detector and a patent application for this is underway.

8.3   Other Work

This thesis was produced during an industrially based CASE studentship with Kromek and has consequently given me the opportunity to get involved in a wide range of projects. A wide range of other work has been carried out which does not appear in this thesis. Some examples of this additional work are given in this section.

This thesis is based on a commercially available detector however during this work a small pixel detector was developed for this application and now appears in Kromek's Verifier Scanners. A poster [81] was presented at the Nuclear Science Symposium in Orlando describing some of the features of this detector. Pixellated detectors with 36×36 elements have also been produced for Siemens with $180 \ \mu m$ pixel size. Siemens are currently investigating these for use in CT imaging applications. A 20 million counts per second detector was also supplied to the European Space Agency (ESA) for testing at CERN. This was a $10 \times 10 \times 2$ mm multi pixel detector with full electronic read out into a Nova Xena II ASIC.

A large amount of materials characterisation work has also been carried out on Kromek's MTPVT grown material. The results of electrical characterisation of CdMnTe was presented in a poster at the Nuclear Science Symposium in Dresden [82] as part of an ESA funded project.

8.4   Patents

The following patents have been filed relating to this work:

HW Add Back Algorithm: Application Number PCT/GB2010/050806
                                        Published as: WO2010/133871

A method and apparatus for correction of detected radiation data from a semiconductor device are described. The method comprising the steps of measuring a pulse energy reading from radiation incident at the semiconductor device; filtering the signal and determining the time that the filtered signal exceeds a predetermined threshold energy; if the determined time is within predetermined parameter(s) comprising at least a predetermined maximum, storing the pulse energy reading in a first, pulse energy data register; if the determined time is above a predetermined maximum, discarding the pulse energy reading and incrementing a count in a second, discard data register; repeating the above steps to acquire a dataset of pulse energy readings of a desired size in the first data register; and on completion of such acquisition; using the discard data register to supplement the dataset of pulse energy readings by numerically correcting discarded counts and adding back into the dataset of pulse energy readings.

HW Filtering Algorithm: Application Number GB1019521.2

A method of and device for processing a radiation pulse based on detecting a pulse at a detector; measuring the energy of the pulse and determining a pulse width and a pulse height; assigning the pulse to one of two or three classes based on the determined pulse width/ pulse height as follows:

> (i) a first class if the pulse width/ pulse height is within a threshold range of a first bounding curve on a notional pulse width/ pulse height plot;

(ii) subject to (iii) below, a second class if the a pulse width/ pulse height is outside the threshold range on a notional pulse width/pulse height plot;

(iii) optionally, a third class if a pulse width/ pulse height otherwise in compliance with (ii) above fails to meet an acceptance criterion; and consequently:

A) If the event is assigned to the first class, using the pulse width and/or height without further correction for further processing;

B) If the event is assigned to the second class, applying a correction to modify the pulse width/ pulse height profile of the pulse and using the pulse width and/ or height so modified for further processing;

C) If the event is assigned to the third class, discarding the pulse.

Fabrication of Semiconductor Material: Application Number GB1105673.6

A method of fabrication of semiconductor material comprising the steps of:

- Providing a wafer of semiconductor material having a first major surface and a second major surface;
- applying to the said first major surface a layer of secondary material in such manner as to cause the layer of secondary material to adhere to the wafer via an adhesive bond at their adjacent surfaces;
- cutting through the secondary material/ wafer assembly in a plurality of linear cutting directions to produce a plurality of semiconductor elements of polygonal cross section from the layer of secondary material/ wafer/adhesive layer;
- removing the secondary material from each such semiconductor element.

References

1   D. Casciani, (BBC News, 2009), Vol. 2011.

2   N. Day, 2009.

3   D. Derbyshire, in *Daily Mail* (Daily Mail, 2010).

4   Nuchtech, (2011), Vol. 2011.

5   CEIA, (2011).

6   H. K. Sanghera et al, Journal of Crystal Growth **237-239** (Part 3), 1711 (2002).

7   B. J. Cantwell et al, Journal of Crystal Growth **275** (1-2), 543 (2005).

8   J. T. Mullins et al, Journal of Crystal Growth **310** (7-9), 2058 (2008).

9   E. Diéguez, in *Comprehensive Semiconductor Science and Technology*, edited by Bhattacharya Pallab, Fornari Roberto, and Kamimura Hiroshi (Elsevier, Amsterdam, 2011), pp. 170.

10   D. Newhouse, (Trend 2009), Vol. 2011.

11   S. Singh et al, Signal Processing **83** (1), 31 (2003).

12   R. F. Eilbert, in *Aspects of Explosives Detection*, edited by Marshall Maurice and C. Oxley Jimmie (Elsevier, Amsterdam, 2009), pp. 89.

13   D. Newhouse, (Trend, 2009), Vol. 2011.

14   A.V. Kuznetsov et al, in *Detection of liquid explosives and flammable agents in connection with terrorism*, edited by A. Kuznetsov H. Schubert (Springer science, St. Petersburg, 2008), p. 233.

15   P. Mostak, in *Detection of liquid explosives and flammable agents in connection with terrorism*, edited by A. Kuznetsov H. Schubert (Springer science, St. Petersburg, 2008), p. 233.

16   V. McMahon, (2011), Vol. 2011.

17   N. Day, 2008.

18   C. Leroy et al, *Principles of Radiation Interaction in Matter and Detection*. (World Scientific Publishing Co., 2004).

19   A. Owens et al, Nuclear Instruments and Methods in Physics Research Section A: Accelerators, Spectrometers, Detectors and Associated Equipment Proceedings of the 5th International Workshop on Radiation Imaging Detectors **531** (1-2), 18 (2004).

20   K. Zanio, *Semiconductors and Semimetals*. (Academic Press, 1978), p.235.

21   G.F. Knoll, *Radiation Detection Measurement*, 3 ed. (John Wiley & Sons, 1999), p.802.

22   H. Spieler, *Semiconductor Detector Systems*. (Oxford University Press, Berkeley, 2005).

23   R. C. Alig et al, Physical Review Letters **35** (22), 1522 (1975).

24   H. K. Sanghera et al, Journal of Crystal Growth **237-239** (Part 3), 1741 (2002).

25   P. Fougeres, et al, Nuclear Instruments and Methods in Physics Research Section A: Accelerators, Spectrometers, Detectors and Associated Equipment **428** (1), 38 (1999).

26   A. Groza et al, Physica Status Solidi C Conferences **2** (5), 1586 (2005).

References

27   J. Franc et al, Nuclear Instruments and Methods in Physics Research Section A: Accelerators, Spectrometers, Detectors and Associated Equipment **434** (1), 146 (1999).

28   Z. Alkan et al, *Landolt-Bornstein-Numerical Data and Functional Relationships in Science and Technology*. (Springer-Verlag, Berlin, 1999).

29   D.J. Olego et al, Applied Physics Letters **47**, 3 (1985).

30   C. Szeles, Materials Research Society Symposium Proceedings **484**, 309 (1998).

31   S. Ramo, Proceedings of the IRE **27** (9), 2 (1939).

32   W. Shockley, Journal of Applied Physics **9** (10), 2 (1938).

33   Z. He, Nuclear Instruments and Methods in Physics Research Section A: Accelerators,Spectrometers,Detectors and Associated Equipment **463** (1-2), 250 (2001).

34   C.K. Jen, Proceedings of the IRE (1941).

35   L. Hamel, Nuclear Instruments and Methods in Physics Research Section A: Accelerators, Spectrometers, Detectors and Associated Equipment **597** (2-3), 207 (2008).

36   K. Hecht, Zeitschrift Fur Physik a Hadrons and Nuclei **77** (3-4), 10 (1932).

37   V.M. Gerrish, *Semiconductors for Room Temperature Nuclear Detector Applications*. (Academic Press, San Diego, 1995).

38   Cremat Inc, (2006).

39   A. Doehring et al, Nuclear Instruments and Methods **59** (1), 40 (1968).

40   V. Radeka, Nuclear Instruments and Methods **99** (3), 525 (1972).

41   P.N. Luke, Applied Physics Letters **65** (22), 2884 (1994).

42   M. Amman et al, SPIE **3115** (1997),

43   A. Kargar et al, Nuclear Science, IEEE Transactions on **56** (3), 824 (2009);

44   A. Zumbiehl et al, Nuclear Instruments and Methods in Physics Research Section A: Accelerators, Spectrometers, Detectors and Associated Equipment **469** (2), 227 (2001).

45   L. Verger et al, Journal of Electronic Materials **26** (6), 738 (1997).

46   R. Redus et al, Nuclear Instruments and Methods in Physics Research Section A: Accelerators, Spectrometers, Detectors and Associated Equipment **380** (1-2), 312 (1996).

47   C. Mestais et al, Nuclear Instruments and Methods in Physics Research Section A: Accelerators, Spectrometers, Detectors and Associated Equipment **458** (1-2), 62 (2001).

48   A. P. Foglio et al, Nuclear Instruments and Methods **70** (1), 52 (1969).

49   Gilmore G, *Practical Gamma-ray Spectrometry*. (John Wiley & Sons, Ltd, 2008).

50   Upp D. L. et al, Journal of Radioanalytical and Nuclear Chemistry, 377 (2004).

51   M. Makarewicz et al, Journal of Radioanalytical and Nuclear Chemistry **244** (3), 649 (2000).

52   J.T. Valentin, Nuclear Instruments and Methods, 592 (1994).

53   S. Gadomski et al, Nuclear Instruments and Methods, 217 (1992).

54   S. Gowda, Pramana **63** (3), 529 (2004).

55   G. J. Hine, Physics Review **85**, 725 (1952).

56   W. Hines et al, *Probability and Statistics in Engineering*, Fourth Edition ed. (John Wiley & Sons, 2003).

57   M. Senior, in *Solid Works* (2010).

58   R. Redus, *XR-100T-CdTe X-ray & Gamma Ray Detector* (2010).

59   A. Sonzogni, in *National Nuclear Data Centre* (Brookhaven National Laboratory, 2011).

60   S. Pomme, Nuclear Instruments and Methods, 338 (1999).

61   J.W. Muller, Nuclear Instruments and Methods, 47 (1973).

62   J.W. Muller, Nuclear Instrument and Methods, 401 (1974).

63   R Bytheway et al, X-ray Tube Simulator (2008).

64   P. Lynn, *The Analysis and Processing of Signals*. (Macmillan Education Ltd, 1982).

65   R. Bytheway et al, X-ray Tube Simulator (2008).

66   D. Bell, FPGA Source Code (2010).

67   D Burgess et al, Nuclear Instruments and Methods in Physics Research Section A: Accelerators, Spectrometers, Detectors and Associated Equipment **236** (2), 368 (1985).

68   L.Wielopolski et al, Nuclear Instruments and Methods **140** (2), 297 (1977).

69   L. Wielopolski et al, Nuclear Instruments and Methods **133** (2), 303 (1976).

70   E.G. Kessler Jr. et al R.D. Deslattes, in *National Institute of Standards and Technology* (2011).

71   A. Cola et al, Nuclear Instruments and Methods in Physics Research Section A: Accelerators, Spectrometers, Detectors and Associated Equipment **568** (1), 406 (2006).

72   G. Prekas et al, Journal of Physics D: Applied Physics **43** (8), 085102 (2010).

73   U. Bonse, *Characterization of crystal growth defects by X-ray methods : proceedings of the NATO Advanced Study Institute on Characterization of Crystal Growth Defects by X-ray* (Plenum Press New York, 1979).

74   S. Cockerton et al, Nuclear Instruments and Methods in Physics Research Section B: Beam Interactions with Materials and Atoms **97** (1-4), 561 (1995).

75   S. Agostinelli et al, Nuclear Instruments and Methods in Physics Research Section A: Accelerators, Spectrometers, Detectors and Associated Equipment **506** (3), 250 (2003).

76   E. J. Buis et al, Nuclear Instruments and Methods in Physics Research Section A: Accelerators, Spectrometers, Detectors and Associated Equipment **599** (2-3), 260 (2009).

77   J. Allison et al, Nuclear Science, IEEE Transactions on **53** (1), 270 (2006).

78   J. Allison et al, Geant4 Simulation of the Bottle Scanner (2010).

79   O. Kadri, Nuclear Instruments and Methods in Physics Research Section B: Beam Interactions with Materials and Atoms **258** (2), 381 (2007).

80   S. Watanabe, Nuclear Instruments and Methods in Physics Research Section A: Accelerators, Spectrometers, Detectors and Associated Equipment **567** (1), 150 (2006).

81   P.D. Scott et al, in *Nuclear Science Symposium* (Orlando, 2009).

82   P.D. Scott et al, in *Nuclear Science Syposium* (Dresden, 2008).